NAZARBAYEV UNIVERSITY

FABRICATION OF 2D AND 3D CONDUCTING POLYMERS AND THEIR NANOCOMPOSITES

by
Guldana Zhigerbayeva

Submitted in partial fulfillment of the
requirement of Nazarbayev University
for the degree of
Doctor of Philosophy in Chemical Engineering

July 2024

FABRICATION OF 2D AND 3D CONDUCTING POLYMERS AND THEIR NANOCOMPOSITES

by
Guldana Zhigerbayeva

Submitted in partial fulfillment of the requirement of Nazarbayev University
for the degree of
Doctor of Philosophy in Chemical Engineering

School of Engineering and Digital Sciences
Nazarbayev University

Supervised by
Dr. Nurxat Nuraje
Dr. Salimgerey Adilov
Dr. John Zhanhu Guo

July 2024

Declaration

I declare that the research contained in this thesis, unless otherwise formally indicated within the text, is the original work of the author's original work. The thesis has not been previously submitted to this or any other university for a degree and does not incorporate any material already submitted for a degree.

_____

Guldana Zhigerbayeva

Date: 2nd July, 2024

Abstract

The Industrial Revolution and the rapid development of advanced materials manufacturing plastic and polymers made the materials of the 21st century. Modern research societies are interested in natural and synthetic polymers due to their adaptability to our daily needs, chemical, mechanical, and optical properties, good processability, and relatively economically efficient production.

The main advantage of polymers over metals and ceramics is their unique and flexible composition, which can be shaped into advanced and more complicated structures. Other advantages include the weight difference, less energy consumption during processing, corrosion resistance, the ability to blend with other polymers easily, and most importantly, the possibility of application in smart materials by constantly replacing the metals with conductive polymers. Before the discovery of conductive polymers, the previous conventional application of polymers was mainly non-electronic due to their inherent insulating properties and mechanical stiffness. Conducting polymers (CPs) attracts researchers due to their ability to combine the electrical properties of metals with the original mechanical and physicochemical properties of traditional polymers.

The applicability of conducting polymers is influenced by their processing characteristics, doping level, redox properties, polymer structure, and whether charge transport is purely electronic or mixed ionic and electronic.

The size and structure of the conducting polymers (CPs) can vary from atomic configuration to microarchitecture. Nanomaterials can be made up of single atoms, atomic clusters, nanowires, atomically thin layers, hierarchical designs, and two-dimensional (2D) or three-dimensional (3D) macrostructures. These diverse forms are crucial for structural design in all aspects. New techniques were created to make 2D and 3D intrinsic structures of different nanomaterials that can be changed to fit different designs through self-assembly or heterostructure synthesis. Depending on the desired application, these techniques can adjust 2D or 3D nanomaterials for better device performance. Phase control, defect formation, doping, and innovative concepts based on the unique structural properties of 2D, and 3D nanomaterials hold significant potential but remain largely unexplored. Conventional methods for fabricating two-dimensional and three-dimensional conducting polymers require many additional endeavors, such as combining several techniques, selecting specific templates, and using highly costly equipment. In this thesis, we introduced a universal strategic synthetic approach that can easily fabricate various morphological structures of

conducting polymers in a one-step step, including nanopowders, nanorods, 2D nanosheets, and 3D bulk materials. Moreover, bicontinuous microemulsion (BME) is a unique interlayered platform that fabricates a continuously porous conducting polymer network. The synthesized materials exhibit an essential increase in performance over traditional template-assisted polymers due to open-cell porosity, which allows better charge transport and adsorption-desorption through the polymer matrix. During this study, four different composite materials were synthesized with polypyrrole using BME and explored their potential applications, such as sensors for heavy metal ions detection, antibacterial coating and working electrode for BES, flexible micro-supercapacitor, flexible ultra-sensitive hydrogen gas sensors working at room temperature.

The great performance demonstrated by fabricated devices proved that the developed platform can be used to synthesize unique multifunctional materials with tailoring properties.

Acknowledgments

Completing a PhD in four years was a significant goal for me, and I was determined to achieve this degree within that timeframe, no matter the challenges. It was a long, tough, and mainly very stressful journey, as balancing several roles of a PhD student, wife, and mother to a newborn was extremely difficult. I am grateful to have reached this milestone and achieved my goal.

First and foremost, I am deeply grateful to my supervisor, Dr. Nurxat Nuraje, for his unwavering support, guidance, and encouragement throughout the entire PhD period. His research ambitions inspired me to work with greater dedication and set high professional goals. I am equally thankful to my co-supervisor, Dr. Adilov Salimgerey, for his support and guidance.

I want to express my gratitude to my colleagues and RE Lab members, especially Dr. Munziya Abutalip, Dr. Vladislav Kudryashov, and Asset Aliyev, for their help, support, and assistance.

I am indebted to my family for their patience, love, support, and understanding. To my parents Dr. Kazhgaliyev Nurlybay and Dr. Kazhgaliyeva Azhar, who were my role models and main support team. To my partner, Dr. Magazov Yerbolat, whose constant support, patience, and love gave me the strength to complete my studies. Most importantly, I would like to thank my baby son, Yerkhan, for being such a wonderful child and allowing me to finish everything on time.

Additionally, I would like to acknowledge the financial support provided by the Faculty Development Competitive Research Grant of Nazarbayev University (no. 021220FD4551) "Crosslinked 3D Nanoporous Conducting Polymer Materials via Bicontinuous Microemulsion-based Approach" and the Targeted Program of MHES of the Republic of Kazakhstan (no. BR21882185), which made this research possible.

Finally, I extend my deepest gratitude to all those who have supported me, directly or indirectly, throughout this journey. Your contributions, no matter how small, have been invaluable.

Thank you all.

Table of contents

List of tables

List of Figures

List of abbreviations

$FeCl_3$	anhydrous iron (III) chloride
p-TSA	p-toluenesulfonic acid
PPy	polypyrrole
MWCNT	multi-walled carbon nanotubes
0D	zero-dimensional
1D	one-dimensional
2D	two-dimensional
3D	three-dimensional
HCl	hydrochloric acid
CPs	conducting polymers
NPs	nanoparticles
HCPs	hybrid conducting polymers
AFM	Atomic force microscope
BET	Brunauer–Emmett–Teller
CTAB	Cetyltrimethylammonium bromide
FTIR	Fourier-transform infrared
GR	Graphene
PANI	Polyaniline
PEDOT	Poly(3,4-ethylenedioxythiophene)
PEDOT:PSS	Poly(3,4-ethylenedioxythiophene)–polystyrene sulfonic acid
PTh	Polythiophene
SEM	Scanning electron microscopy
TEM	Transmission electron microscopy
TGA	Thermal gravimetric analysis
Co_3O_4	Cobalt (iii) oxide
Ag	silver
N-CDOT	Nitrogen doped carbon dots
CoO	Cobalt (ii) oxide

IPNs	interpenetrating polymer networks
LED	light-emitting diodes
Au	gold
Pt	platinum
CNT	carbon nanotubes
TiO_2	titanium dioxide
ZnO	zinc oxide
MnO_2	manganese dioxide
P3HT	poly (3-hexylthiophene)
UV	Ultra-violet
BME	bicontinuous microemulsion
Py	pyrrole
VPP	vapor-phase polymerization
ME	microemulsion
HLB	hydrophilic-lipophilic balance
O/W	oil-in-water
W/O	water-in-oil
SDBA	sodium dodecylbenzene sulfonic acid
APS	ammonium persulfate
FIP	freezing interfacial polymerization
MF	melamine foam
XRD	X-ray diffraction
EDX	energy-dispersive X-ray spectroscopy
BET	Brunauer–Emmett–Teller
BJH	Barrett-Joyner-Halenda
PL	photoluminescence spectroscopy
SDS	sodium dodecyl sulfate
DCM	dichloromethane
FTIR	Fourier transform infrared spectrometer
BC	bicontinuous
DI	deionized water
SD	standard deviation
BES	bioelectrochemical system
EET	extracellular electron transfer
PBC	pure bicontinuous system
NBC	nonionic bicontinuous system
BEC	bioelectrochemical cell
CA	chronoamperometry
WE	working electrode
CV	cyclic voltammetry
DPV	differential pulse voltammetry
EC	electrochemical
ATP	adenosine triphosphate
ROS	reactive oxygen species
KOH	potassium hydroxide
THF	tetrahydrofuran

NaCl	sodium chloride
MgSO4	magnesium sulfate
NMR	Nuclear Magnetic Resonance
CH_2Cl_2	dichloromethane
$AlCl_3$	aluminum chloride
DMSO	dimethyl sulfoxide
NaOH	sodium hydroxide
MSC	micro-supercapacitor
EDLC	electrochemical double-layer capacitance
PVDF	poly(vinylidene difluoride
PVA	poly(vinyl alcohol)
NMP	n-Methyl-2-pyrrolidone
H_2SO_4	sulfuric acid
PET	polyethylene terephthalate
Cr	chromium
EIS	impedance spectroscopy
GCD	galvanostatic charge/discharge
H_2	hydrogen gas
CO_2	carbon dioxide
NO_2	nitrogen dioxide

List of symbols

Symbol Description

σ	conductivity
T	temperature
π	value of Pi
T_g	glass transition temperature
µm	micro-meter
ms	mass of swollen gel
md	mass of dry gel
l	length
R	resistance
A	cross-sectional area
ρ	bulk resistivity
W	width
H	height
$\sigma\sigma$	relative uncertainty in conductivity
σ_R	standard deviation of resistance
Ω	Ohm
Å	Angstrom
C	capacitance
ϑ	scan rate
ΔV	the voltage window
I	current
E	energy density
P	Power density
$\int i\, dV$	the area of the CV curve
Δt	discharge time

CHAPTER 1. INTRODUCTION

1.1 Intent of this Thesis

The modern research community's huge interest is directed to natural or synthetic polymers due to their adaptability to our daily life needs and, more importantly, their desirable chemical, mechanical, and optical properties, good processability, and relatively economically efficient production. The main advantage of polymers over metals and ceramics is their unique and flexible composition, which can be shaped into advanced and more complicated structures. Besides the weight difference, there is less energy consumption during processing, corrosion resistance, the ability to blend with other polymers easily, and, most importantly, the possibility of application in smart materials that constantly replace metals with conductive polymers.

Conducting polymers has received significant attention in recent decades due to their wide range of applications. Numerous synthetic procedures have been established to create diverse nanostructures of conducting polymers, each with exciting features. Nevertheless, the methods for producing two-dimensional (2D) nanosheets are either intricate or costly. There is currently no established methodology for the synthesis of both 2D and 3D materials or their composites. As a result, developing new structural engineering approaches and understanding how they govern the characteristics of 2D and 3D nanomaterials is vital.

This study demonstrates a simple and scalable approach for fabricating conducting polymer nanocomposites in two-dimensional, three-dimensional, and other complex shapes by modifying the interface within a bicontinuous microemulsion system. The bicontinuous microemulsion polymerization method serves as a soft template, enabling the production of polymeric materials with a unique, continuously porous morphology. The uniqueness of this synthesis method lies in its ability to create materials with different dimensional structures (0D, 2D, and 3D) by adding cross-linkers into the polymer matrix or increasing the concentration of the oxidant and dopant. This structural versatility, from nanoscale thin films to macroscale porous gels, allows for the fabrication of materials with tailored properties to suit specific application needs. Through this research, we developed a novel technique that allows us to synthesize various free-standing structures of conducting polymers with different morphologies and tailored multifunctional properties.

1.2 Hypotheses

After a literature review of the existing polymerization techniques for 2D and 3D conducting polymers, these hypotheses were defined:

1. The unique oil-water layered nature of the BME polymerization method allows the fabrication of free-standing 2D and 3D conducting polymers and their composites with better structure-property characteristics, which will expand the application of the materials.

2. Adding a cross-linker to the polymer matrix will improve the layered structure of BME, resulting in the synthesis of many-layered 2D films that allow the fabrication of hybrid conducting polymer films with tailored properties.

3. The unique continuous structure of bicontinuous microemulsion allows template-free fabrication of 3D continuously porous hybrid conducting polymer soft gels by simply increasing the oxidant concentration.

4. Incorporating cobalt oxide into polypyrrole (PPy) soft gels will enhance their capacitance, thereby improving their suitability as electrode materials for flexible micro-supercapacitors.

5. The introduction of graphene nanoflakes into the continuously porous PPy matrix will enhance the electrical conductivity and increase the material's surface area, thereby improving its sensitivity and overall performance as a hydrogen gas sensor.

1.3 Objectives of the Study

1. The thesis's primary goal is to develop a new, one-step bicontinuous microemulsion-based method for the synthesis of continuously porous 2D and 3D hybrid conducting polymers and their nanocomposites.
2. The secondary objective is to study the morphology-property relationship of these materials comprehensively.
3. The final objective is to explore potential applications of the developed conducting polymer materials.

1.4 Aims of the Study

The developed objectives of the study formulate research aims:

1. Design a universal synthesis approach that will allow the development of hybrid conducting composite materials with tunable multifunctional properties for desired applications.
2. Investigate the factors affecting the fabrication of 2D and 3D conducting polymer morphologies.
3. Investigate the gas sensitivity of the 3D polypyrrole-graphene composite material.
4. Design planar micro-supercapacitors based on 3D PPy-CoO soft gels and quantify their capacitance.

1.5 Scientific Significance and Novelty of Study

The originality of this thesis lies in the development of a one-step, scalable, tunable synthesis method for creating free-standing 2D and 3D conducting polymers and nanocomposites with tailored structure-property relationships and a broad range of potential applications. The developed polypyrrole composites address the key challenges in hydrogen gas sensing and micro-supercapacitors, contributing to the advancement of sensor and micro-supercapacitor technologies.

1.6 Research Outputs

Publications

Abutalip, M., Zhigerbayeva, G., Kanzhigitova, D., Askar, P., Yeszhan, Y., Pham, T. T., Adilov, S., Luque, R., & Nuraje, N. (2022). Strategic synthesis of 2D and 3D conducting polymers and derived nanocomposites. *Advanced Materials*, *35*(5).https://doi.org/10.1002/adma.202208864

Conferences

Zhigerbayeva, G., Nuraje, N., Turlybekuly, A., & Adilov, S. (2024, May). Pure 3D Conducting Polymer Network for an Ultra-Sensitive and Flexible Hydrogen Gas Sensor at Room Temperature. In *245th ECS Meeting (May 26-30, 2024)*. ECS.

1.7 Thesis Overview

The focus of this thesis is the fabrication of conducting polymers and their hybrid composites, especially polypyrrole (PPy) and combining them with other materials to make them work better in different technological settings. The work is divided into several chapters, each addressing

different aspects of the research, from foundational literature to innovative synthesis methods and practical applications.

Chapter 2 discusses the fundamental principles governing conductivity, the synthesis methods used to create hybrid conducting polymers, and the properties of conducting polymers. It also delves into the specific conduction mechanisms of polypyrrole, one of the most widely studied conducting polymers.

Chapter 3 reviews the synthesis methods for polypyrrole, detailing techniques such as microemulsion polymerization, interfacial interactions during microemulsion polymerization, bicontinuous microemulsion polymerization, and various characterization techniques.

Chapter 4 explores the development of a synthetic strategy for fabricating two-dimensional (2D) and three-dimensional (3D) conducting polymers and their nanocomposites. This chapter thoroughly examines how conducting polymers polymerize using four different bicontinuous microemulsion interfaces.

Chapter 5 demonstrates the successful synthesis of 3D continuously porous polypyrrole gels with moderate porosity and high pore volume, highlighting their high electrical conductivity. This chapter provides a detailed study of the property-morphology relationships, laying a foundation for further investigation into their applications and potential modifications.

Chapter 6 covers the synthesis of various conducting polymer composite materials and their applications, synthesized by the bicontinuous microemulsion polymerization technique. It includes 2D PPy@Ag/Co_3O_4 composite films for antibacterial behavior analysis and 3D PPy-Seb. Linker-N-CDots for heavy metal detection, 3D PPy-CoO for flexible micro-supercapacitors for energy storage applications, and 3D PPy-graphene for flexible, ultra-sensitive hydrogen gas sensors at room temperature.

Chapter 7 outlines potential future research directions and summarizes the essential findings and contributions of the thesis.

CHAPTER 2. LITERATURE REVIEW

2.1 Conducting polymers (CPs).

Polymers are macromolecules composed of smaller monomers that can be interconnected differently, leading to diverse microstructures. The notion that plastics could be electrically conductive was impossible until roughly four decades ago. Nevertheless, in 1977, Hideki Shirakawa, Alan Macdiarmid, and Allan Heeger made the groundbreaking discovery that polyacetylene can conduct electricity.[9] This vital discovery led to a new field of study at the intersection of chemistry and condensed matter physics. The new class of materials made it possible to create modern energy storage systems, organic photovoltaic cells, electronic devices, etc. In later research, Heeger and Macdiarmid [10] discovered that oxidative doping could make the polymer twelve times more conductive than pristine polyacetylene. This invention spread quickly through the polymer and electrochemistry communities, ultimately leading to an intensive investigation of alternative conducting polymers, and was rewarded with the Nobel Prize in 2000. The mechanical and electrical properties of conducting polymers result from alternating single and double bonds, as shown in Figure 2.1. Their electrical and optical properties, solubility, and processability depend on the attached dopant ions and composite side chains obtained by additional fillers into the polymer matrix.[11] The delocalized state of π bonds influences the crystallinity and amorphous nature of CPs and is also crucial in generating charge carriers, such as polarons, bipolarons, and solitons.[12,13] When CPs are doped or excited with light, the π bond starts self-localization and changes the polymer from a nonlinear insulating state to a metallic state with higher conductivity and a moderate bandgap. [11,14,15]

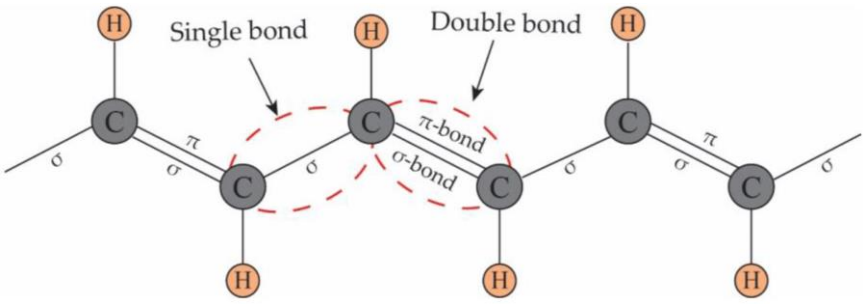

Figure 2.1. Illustration of the conjugated single and double bonds of polyacetylene. [16]

The term "conducting polymer" covers two distinct definitions: the first refers to polymers loaded with conductive fillers such as carbon black, metal flakes, or fibers. [17,18] These polymers are

recognized for their affordable price, lightweight nature, strong mechanical properties, and ease of processing. The primary practical role of the polymer matrix is to act as an adhesive binder of the conductive components together into an integrated solid structure. The low cost, lightweight, mechanical durability, and simplicity of processability of the polymer component, in conjunction with the relatively bulky solid conductivity, are the factors that have contributed to the interest in such materials. The second, in contrast, refers to polymers that produce and transmit charge carriers throughout the polymeric chain. Compared to the first category, these polymers have advantages such as managing electrical conductivity by regulating oxidation or reduction reactions, identifying the type of charge carriers, and easing the transition between conductive and insulating states. However, they need more processability, mechanical properties, and environmental instability. Various structural modifications are being developed, including interpenetrating polymer networks (IPNs), co-polymers, and hybrid conducting polymers (HCPs).[16,19]

The conducting polymers that have been studied and used the most extensively are polyacetylene (PA)[19], polyaniline (PANI)[20], polypyrrole (PPy)[21], polythiophene (PTH)[22], poly(3,4-ethylenedioxythiophene) (PEDOT)[23] and their derivatives. The chemical structures of these conducting polymers are depicted in Figure 2.2. Among them, polypyrrole is widely recognized and extensively researched, with various morphologies such as nanoparticles[24], nanotubes[25], nanofibers[26], thin films[4], thick films[27], and sponge-like[28] structures. The unique properties of conducting polymers make them attractive for a wide range of applications, such as electrochemical energy storage devices[29], sensors[30], light-emitting diodes (LED)[13], bioengineering devices[31], organic solar cells[32], electromagnetic shielding[33], and others.

Figure 2.3 demonstrates the number of publications dedicated to polypyrrole and polypyrrole films in the last decade. However, to the best of our knowledge, no comprehensive synthetic approaches allow for the easy fabrication of perfect two-dimensional and three-dimensional conducting polymer hybrid composite materials.

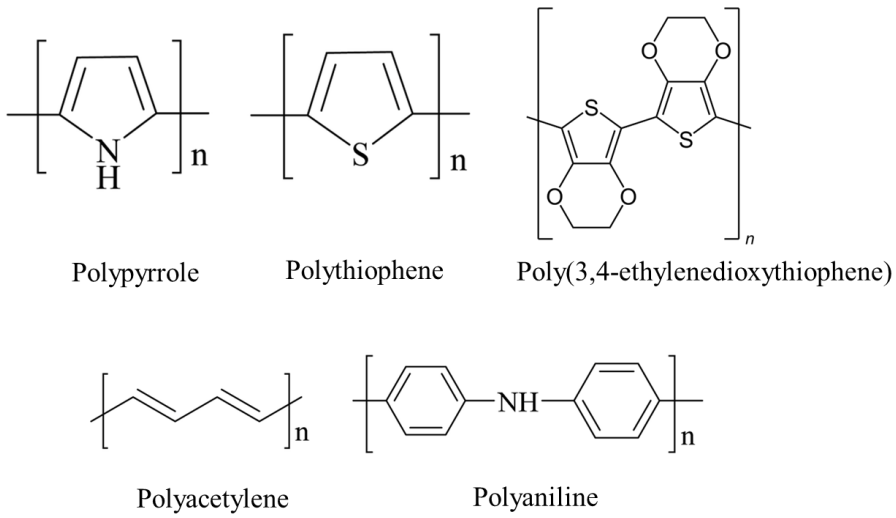

Figure 2.2. Schematic illustration of some conducting polymers.

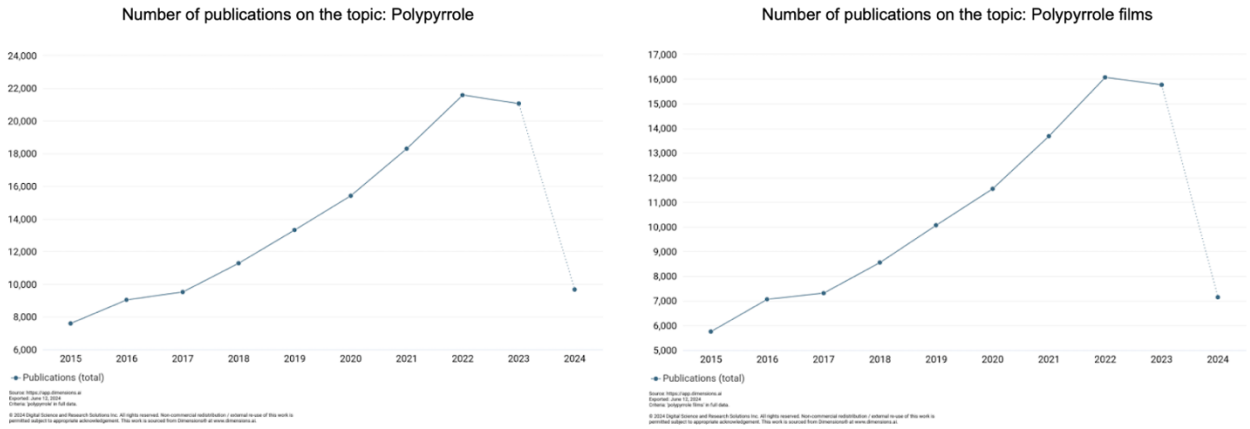

Figure 2.3. The number of publications in the last decade dedicated to polypyrrole and polypyrrole films.

2.1.1 The Hybrid conducting polymers (HCPs).

Hybrid conducting polymer composites (HCPs) represent a versatile class of organic compounds that are achieved by incorporating organic or inorganic constituents into the conducting polymer matrix. The successful fabrication of conducting polymer composite material enhances the intrinsic properties of the pure conducting polymer while introducing additional functionalities dictated by the nature of nanoparticles introduced to the polymer system and the synthesis method employed. The distinctive structure of the CPs enables the creation of diverse composite materials

that make them attractive candidates for multifunctional systems.[34] Modified conducting polymers as multifunctional materials open new opportunities for developing novel smart materials with advanced electrical, optical, and mechanical properties.[35] They have applications in different types of sensors[36–38], catalysis[39], LED[40], medical diagnosis[41], photovoltaic devices[32], supercapacitors[42] and so on.

The research community's primary interest is conducting polymer composites based on metal/carbon nanoparticles. Metals like gold (Au), silver (Ag), or platinum (Pt) are often paired with conducting polymers to introduce specific properties such as enhanced conductivity, stability, antibacterial properties, and catalytic activity. Carbon-based materials such as carbon nanotubes (CNT), graphene, and carbon black are another widely utilized category of nanoparticles. These composites augment the electrical conductivity, mechanical properties, surface area of polymers, and thermal stability. Additionally, inorganic nanoparticles, including metal oxides such as titanium dioxide (TiO_2), zinc oxide (ZnO), manganese oxide (MnO_2), and cobalt oxides (Co_xO_y), are frequently integrated into hybrid conducting polymers. Metal oxides within the polymer matrix provide specific functionalities such as photocatalytic activity, sensing capabilities, improved charge transfer, and storage ability.[34]

The addition of dopant molecules or conducting salts can induce structural rearrangements within the conducting polymer matrix, altering the materials' electrical properties and charge transport characteristics and thereby enhancing performance in different application areas.

The synthesis of these composite polymer materials typically involves three primary methods: dispersing metal nanoparticles into a polymer matrix, generating nanoparticles in situ during polymerization, or polymerizing the matrix around a metal nanocore using chemically compatible ligands or polymeric structures. Each method presents its own set of limitations. For example, the dispersion of metal particles within a polymer matrix often results in an uneven distribution of particles and subsequent particle agglomeration.[43] The second approach offers a means to avoid agglomeration, but controlling the quantity of NPs formed is challenging.[44] The third method, utilizing a metal core as a template for polymer growth, is also constrained, as it is contingent upon the application and the characteristics of the metal employed, which may be prone to corrosion or rigidity issues.[45]

2.2 Conduction Mechanism of Conducting Polymers (CPs).

The primary factor influencing the electrical conductivity of a polymer is its electronic configuration. Developing intrinsic conductivity in polymers requires a conjugated structure consisting of conjugated segments or conjugated structures with alternating single and double bonds or atoms providing p-orbitals for a continuous orbital overlap (e.g., N, S). As a result of the free movement of electrons throughout their structure, metals have high conductivity.

To facilitate the movement of delocalized π-electrons along the polymer chain, conducting polymers comprise a series of sp^2-hybridized carbon atoms in their backbone. These π-bonds significantly influence the inherent electrical characteristics of the material, as they facilitate electron mobility, a fundamental requirement for electrical conduction.[46] In the undoped or neutral state of a conducting polymer, the π-electron system is similar to that of a semiconductor, consisting of an energy gap separating the empty conduction band from the full valence band. The energy band theory visualizes the distinctions between conductors, insulators, and semiconductors, as shown in Figure 2.4. However, it does not fully explain why organic materials like polymers conduct electricity.

The band gap is a crucial concept in band theory, representing the energy difference between the valence band's topmost occupied level and the conduction band's lowest unoccupied level. In insulators, a wide band gap prevents electrons from quickly crossing. At the same time, semiconductors have a smaller gap, enabling electron excitation by thermal energy or photon absorption, making conductivity possible under certain conditions. The conductivity of such materials can be significantly improved by doping, which can be either oxidative (p-type doping) or reductive (n-type doping). Oxidative doping depletes electrons from the π-system, introducing positively charged carriers, known as 'holes,' into the polymer chain. The movement of these holes along the polymer's backbone leads to hole conduction. In contrast, reductive doping introduces additional electrons into the π-system, resulting in the formation of negatively charged carriers that enhance conductivity by electron transport.[9,16,47]

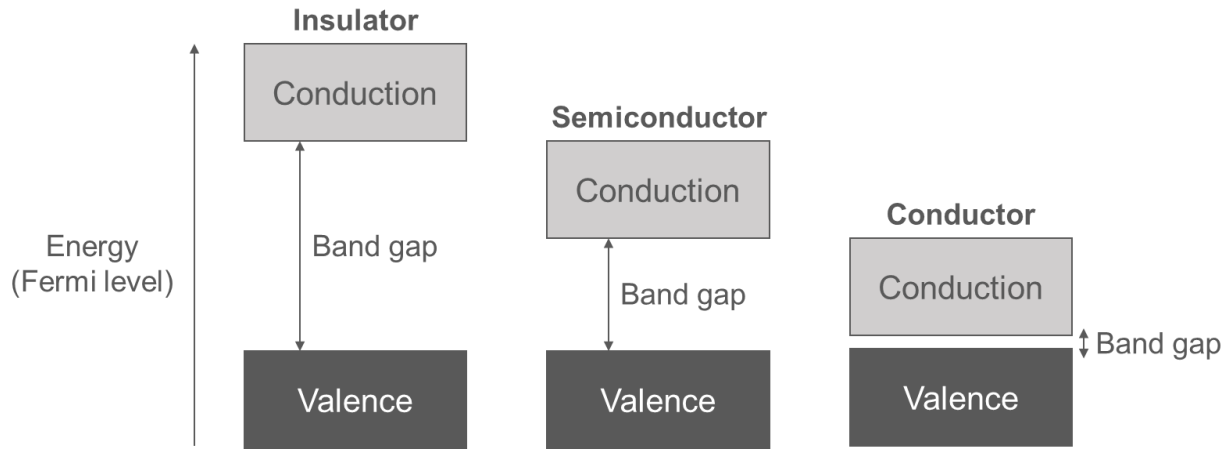

Figure 2.4. Band structure of solids: insulators (the large E_{gap} between the valence and conduction bands in insulators means that at room temperature, electrons cannot reach the conduction band), semiconductors (the moderate E_{gap} allows the valence band to overlap the conduction band by thermal energy), and conductors (overlap of the valence band and the conduction band and the valence electrons can move through the material).

Conducting polymers exhibit a complex charge transport mechanism involving the transport of charge carriers and the rearrangement of the molecular structure of polymer in response to doping.[9] Polarons are the primary charge carriers in many doped conducting polymers, carrying charge and spin due to the removal or addition of an electron from the π-system.[48] They can migrate along the polymer chain, contributing to electrical conductivity. Bipolarons are formed when two polarons merge, resulting in the loss or gain of two electrons, creating a doubly charged carrier, which reduces the band gap and enhances the polymer's electrical conductivity.[49] Solitons, unique to certain types of conducting polymers, are topological excitations that create a domain wall between different electronic states of the polymer.[50] These charges can move freely along the polymer chain without energy loss, contributing to charge transport. This understanding has opened opportunities for developing various applications, including flexible electronics and energy storage systems. Figure 2.5 gives a comparative overview of the electrical conduction range possibilities of the conducting polymers with other materials in doped and undoped cases. Additionally, Table 2.1 represents the quantitative conductivity, energy band gaps, and doping types for the most studied conducting polymers.

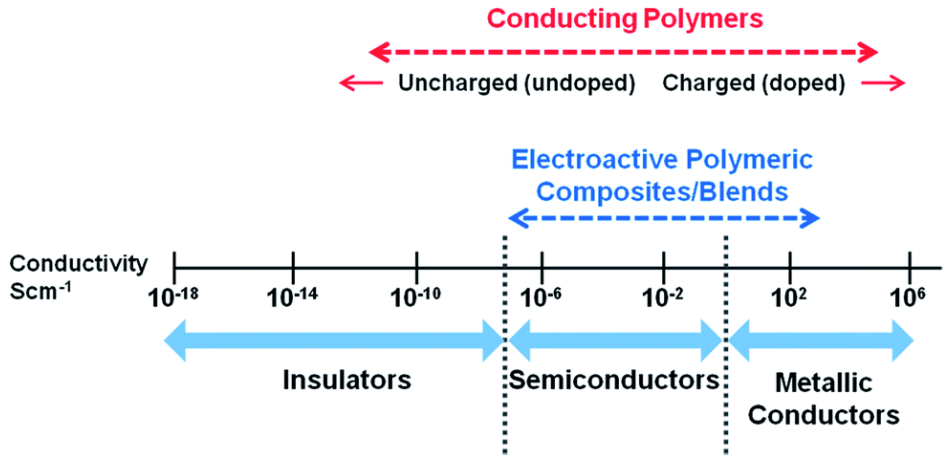

Figure 2.5. The comparative illustration of the electrical conductivity range of CPs with other types of conducting materials.[1]

Table 2.1. Electrical conductivity and energy band gap of some conducting polymers.

Conducting polymer	**Band gap (eV)**	**Conductivity (S cm^{-1})**	**Types of doping**	**References**
Polyacetylene	1.5	10 -10^3	p	[51]
Polypyrrole	3.1	10^2 - 7.5×10^3	p	[52]
Polyaniline	3.2	30 - 200	n,p	[51]
Polythiophene	2.1	10 - 10^3	p	[22]
Poly(3,4-ethylene dioxythiophene)	1.1	0.4 - 400	n,p	[22,51,53]

2.2.1 Conduction mechanism of Hybrid Conducting Polymers (HCPs).

The conduction mechanism observed in hybrid conducting polymers is similar to that of pristine conducting polymers, with electrical conductivity increasing through processes like charge transfer or electron delocalization. Elevated dopant concentrations typically correspond to increased electrons, thus influencing the superior electrical performance of conducting polymer composites. Molecular rearrangements accompany the synthesis of HCPs due to different manipulations. The conduction mechanism in HCPs arising from various interactions within the polymer matrix during synthesis with nanoparticles may occur, such as Van der Waals's, hydrogen

bonding, and electrostatic interactions, based on the type of components. In most cases, the conduction mechanism of HPCs predominantly involves charge-hopping, which involves the movement of charge carriers such as electrons and holes between localized states within the polymer matrix and nanoparticles. The presence of nanoparticles in the polymer structure provides additional sites for charge carriers to hop between, thereby improving conduction in regions where the polymer alone may exhibit insulating behavior. Furthermore, introducing NPs into the polymer matrix can induce modifications in the material's band structure. For instance, metal nanoparticles introduce additional energy states within the band gap of the polymer and narrow the band gap, allowing the easier and faster movement of the carriers through the material. For example, the PANi-TiO_2 composite demonstrated interfacial interaction, which improved the material's electrochemical stability and oxidation potential.[54] Similarly, polymer/metal interaction is performed by the poly (3-hexylthiophene) P3HT/Au hybrid. The electrical conductivity of the composite was increased by the electron hopping effect and homogeneously distributed gold nanoparticles in the P3HT matrix.[55] Carbon-based composites, such as graphene sheets or multi-walled carbon nanotubes (MWCNT), increase the porosity of the polymer materials and promote coupling between the polymer chains, thereby preventing the agglomeration of nanoparticles and improving charge carrier transfer and conductivity, respectively.[56,57] This improvement can be attributed to the strong p-p interactions between polypyrrole and graphene nanosheets, forming a continuous conducting pathway.

2.2.2 Conduction mechanism of Polypyrrole (PPy).

Polypyrrole (PPy) exhibits conductivity due to alternating single and double bonds within its molecular structure, resulting in a delocalization of electron density throughout the polymer. In its undoped state, polypyrrole acts as an insulator with a large band gap of 3.16 eV.[58] During oxidation, the neutral PPy chain loses a π-electron and undergoes local deformation from a benzenoid structure to a quinoid one, producing a polaron. This results in the formation of two localized electronic states within the energy gap, with the unpaired electron occupying the bonding state (Figure 2.6). Through further oxidation, a second electron is extracted from the PPy chain, creating a doubly charged bipolaron. The degree of benzenoid-to-quinoid distortion appears stronger in bipolaron than in the polaron. As the polymer undergoes additional oxidation, bipolarons merge, creating two distinct, narrow bipolaronic bands. This process also causes a reduction in the energy gap to 1.4 eV. [59]

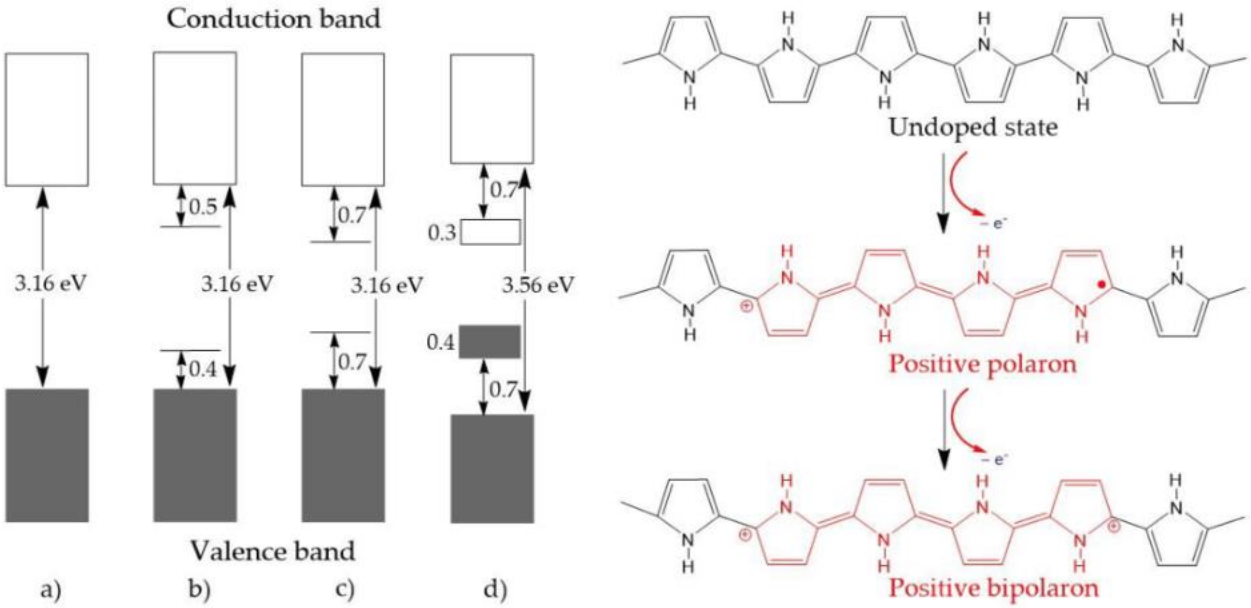

Figure 2.6. The electronic conduction band movement mechanism of polypyrrole in various states: a) undoped, (b) polaron, (c) bipolaron, and (d) doped.[60]

2.3 Synthesis of Hybrid Conducting Polymers (HCPs).

Conducting polymers are a class of organic polymers with intrinsic conducting properties. The synthetic approach used for their fabrication can elevate their unique mechanical, optical, and electrical properties. Many approaches have been developed for the synthesis of conducting polymers and their nanocomposites, including chemical oxidation polymerization, electrochemical polymerization, vapor phase, hydrothermal, solvothermal, microemulsion, photochemical, template-assisted, and solid-state methods. Table 2.2 summarizes the advantages and disadvantages of different polymerization techniques utilized for the synthesis of HCPs.

Table 2.2. Summary of standard polymerization techniques for conducting polymers, with their advantages and disadvantages.

Polymerization approach	Advantages	Disadvantages	Applications	Ref.
Chemical polymerization	-High yield, suitable for industrial application	-Limited control over polymer structure and	Energy storage, bulk synthesis,	61–63

	-Control over molecular weight of polymer -Cost-effective -Bulk production -Universal for different CPs	morphology -Cannot produce freestanding CP films -Environmental concern (use of potentially toxic solvents, catalysts) -Possible impurities -Post-processing requirements	coatings, industrial production, anticorrosion, LED, battery electrodes	
Electrochemical polymerization	-High purity and conductivity of CPs -Can control thickness and morphology -No need for oxidants -Form uniform films on a substrate -Room temperature operation -Allows in-situ doping	-Reduced yield and scalability -Requires conductive substrate -Depends on the electrolyte properties -Thickness limitations;	Solar cells, biosensors, delivery systems, supercapacitors	64–67
Photochemical polymerization	-Initiate polymerization without thermal energy -Morphology can be controlled under light -Ambient conditions -High precision in patterning -Fast reaction rate -Versatile	-Limited to photosensitive monomers -Requires special, complex equipment -Potential degradation of material under light -Limited depth of light penetration -Limited scalability	Organic photovoltaics, Microelectronics photolithography, LED, photoresponsive materials	68–71
Plasma polymerization	-Thin film production -No need for solvents - Suitable for a wide range of monomers -Functionalization Surface modification -Ambient conditions -Higher adhesion of obtained films	-Complex and expensive equipment -Limited control over polymer structure -Require vacuum conditions -High energy consumption -Difficult control of deposition rate	Biomedical applications, surface coatings, electronics, gas sensors, corrosion-resistant coatings	72–75
Interfacial polymerization	-High molecular weight polymers -Can create thin films and bulk materials Simple and efficient	-Limited control over reaction kinetics -Possible interfacial instability -Monomer solubility issues	Filtration membranes, gas sensors, supercapacitors, biomedical	76–78

	-Fast reaction rate -Control over the thickness of polymers - Scalable -Versatile	-Post-processing requirements	implants	
Template-assisted	-Precise control over polymer morphology -Versatile for different templates -Can create nanostructured polymers -Controlled pore size and pore size of polymers	-Template removal is challenging -Limited properties due to the type of template -Cost of templates -Template contamination	Sensors, capacitors, and scaffolds, bioelectrochemical application	[79–81]
Hydrothermal polymerization	-Precise control over reaction conditions, leading to consistent and reproducible polymer structure -Crystalline polymer structure for better mechanical properties of polymers -Versatile polymer morphologies -High-purity polymers -Green synthesis technique	-Special equipment is required - High energy consumption (also temperature, pressure) - Slow reaction time - Low scalability - Limited suitable monomer range	Battery electrodes, supercapacitors	[82–85]
Emulsion polymerization	-High molecular weight -Control over particle size -High reaction rate -Environmentally friendly Stable dispersion of monomer	-Surfactant residues in the final product -Complex purification required -Limited monomer solubility -More mechanically stable polymers -Lower electrical conductivity	antistatic coatings, sensors, electromagnetic shielding, organic photovoltaics, OLEDs, energy storage systems	[86–88]

Polypyrrole exhibits unique electrical conductivity, distinctive redox activity, and stability at room temperature, and it can be simply prepared in solution.[3,58,59]

Chemical and electrochemical polymerization are the two most frequently employed synthesis techniques for synthesizing polypyrrole[61,62,64,66,78,81,89].

Initiation of the oxidation reaction requires an oxidant solution such as iron (III) chloride ($FeCl_3$), ammonium persulfate (APS), or other oxidizing and doping agents.[60] Other synthesis methods for PPy include microemulsion polymerization, vapor-phase polymerization (VPP), temperature-assisted polymerization, interfacial polymerization, photopolymerization, and template-assisted polymerization.

Our research specifically concentrated on the microemulsion polymerization of polypyrrole, among which bicontinuous or middle-phase polymerization was chosen. This approach was selected for its ability to create homogenous and well-defined polymer structures. To get a comprehensive understanding of the benefits and complexities of this method, we will provide an in-depth explanation of the microemulsion polymerization process.

2.3.1 Microemulsion polymerization of polypyrrole.

Microemulsions have garnered significant attention in polymer synthesis due to their unique ability to provide a stable, homogeneous, well-dispersed medium for polymerizing various monomers.[90–92] One of such monomers extensively studied in the context of microemulsion polymerization is pyrrole. [4,5,78,93]

A microemulsion (ME) is a thermodynamically stable, isotropic mixture of two immiscible liquids, such as oil and water, stabilized by surfactant and co-surfactant molecules.[94] It is widely used in industrial fields like pharmaceuticals, cosmetics, paints, and the food industry. The theories and characteristics of microemulsions are the fundamentals of colloidal chemistry. Microemulsion polymerization employs surfactant micelles as flexible templates to produce polymeric particles, and the operational conditions and surfactant type influence the morphology of the micelles. [95] Surfactants with longer carbon chains reportedly facilitate the production of larger nanoparticles, as they offer a more significant amount of internal space to facilitate the necessary polymerization.[94]

Microemulsions undergo structural changes based on their composition and formation conditions, influenced by the surfactant concentration, hydrophilic-lipophilic balance (HLB), and the water-to-oil ratio, as shown in Figure 2.7.

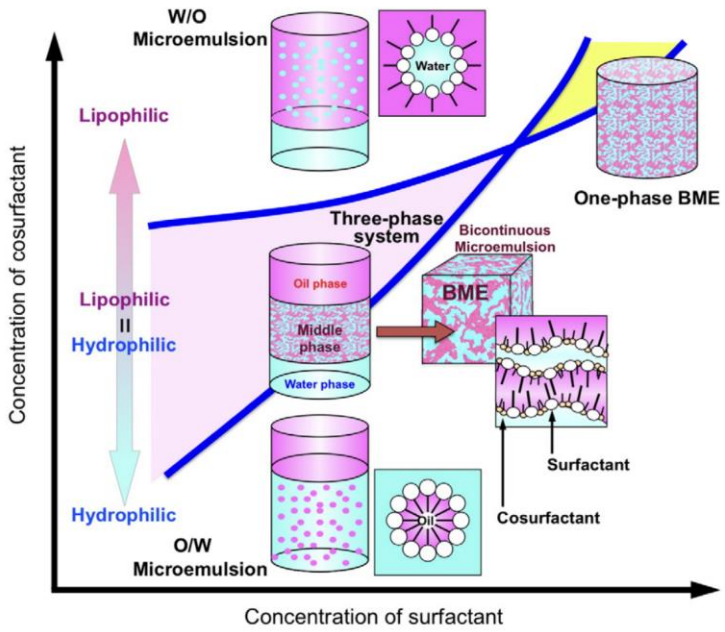

Figure 2.7. The diagram illustrates the different phase configurations of microemulsions (MEs) that are determined by the hydrophilic-lipophilic balance (HLB). [2]

A microemulsion system phase diagram is a graphical representation that illustrates the different phases formed by varying the proportions of water, oil, and surfactant (Figure 2.8). Typically presented as a ternary phase diagram, it uses an equilateral triangle to display the compositions of the three components.

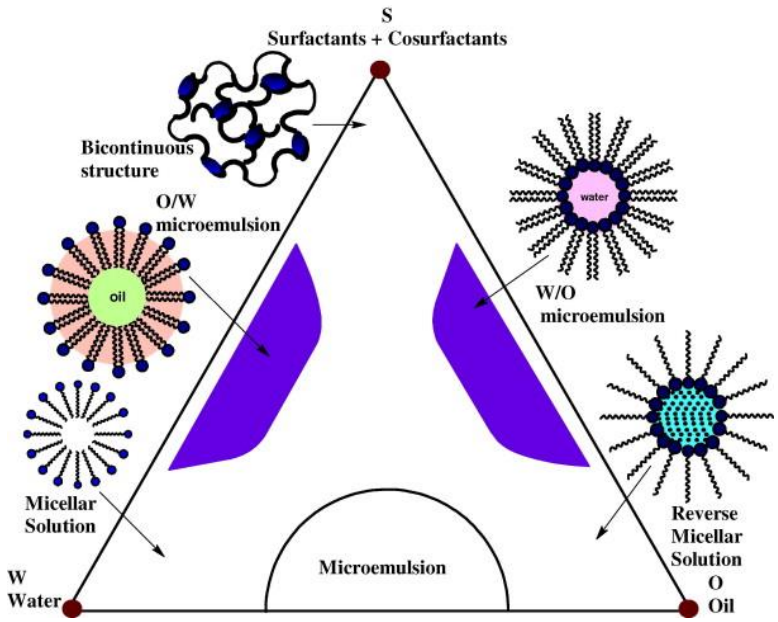

Figure 2.8 Ternary phase diagram of oil, water, and surfactant microemulsion solution. [91]

Within this diagram, distinct regions indicate the presence of single-phase microemulsions (such as oil-in-water or water-in-oil microemulsions) and multiphase equilibria (such as two-phase and three-phase systems). Phase boundaries within the diagram separate these regions, helping to predict and understand the stability and behavior of the microemulsion under different compositional conditions. Winsor's observation classifies microemulsions into four distinct types based on their phase behavior and composition: Winsor I, Winsor II, Winsor III, and Winsor IV.[96] There are four main phases:

- *Windsor I - Oil-in-water (O/W)* - Microemulsions are composed of tiny oil droplets evenly distributed throughout a continuous water phase. The stability of this structure is enhanced by surfactants with high hydrophilic-lipophilic balance (HLB) values, which facilitate the dissolution of oil in water. O/W microemulsions are well-suited for polymerizations that include water-soluble monomers. They provide an environment inside the scattered oil droplets where polymer formation may occur.
- *Windsor II—Water-in-oil (W/O)* microemulsions are water droplets that diffuse inside a continuous oil phase. The structure is defined by small, spherical water droplets stabilized by a surfactant layer. This particular microemulsion is often created when the surfactant has a low HLB value, promoting water dissolution in oil. These structures are beneficial for polymerizations in which the monomer is soluble in oil, enabling controlled polymer growth within the dispersed aqueous phase.
- *Windsor III—Bicontinuous (middle phase)* microemulsions are characterized by an intricate arrangement in which both water and oil phases create continuous, interconnected networks. This particular microemulsion arises when surfactant concentrations and HLB values are in between, resulting in neither phase being dominant. The bicontinuous structure is advantageous for polymerizations that need hydrophilic and hydrophobic environments. It allows for consistent polymerization and promotes the creation of hybrid materials with distinctive features.
- *Windsor IV- single-phase microemulsions* - stable, isotropic solutions formed by a homogeneous mixture in which the oil, water, and surfactant are completely miscible. Winsor IV microemulsions are optimal for applications that require consistent performance and a long storage life due to their thermodynamic stability, which prevents them from separating over time. Their high solubilization capacity enables them to transport both

hydrophilic and lipophilic substances, which is particularly advantageous in pharmaceuticals for improving drug bioavailability and in cosmetics for effectively conveying active ingredients. Furthermore, Winsor IV microemulsions are employed in the food industry for enhanced oil recovery, as they ensure additives' uniform distribution and stability. The formulation of these systems necessitates the meticulous selection and optimization of the components to preserve the delicate equilibrium required for their distinctive characteristics.

2.3.2 Interfacial interactions during microemulsion polymerization.

Microemulsion polymerization involves dispersing monomers in either the aqueous or oil phases, and several key factors—such as monomer solubility, concentration, reactivity, and structure—play a critical role in influencing the polymerization process. Additional parameters like temperature, solvent concentrations, and the presence of doping agents also have a significant impact on the final thickness and morphology of the produced polymers. In this process, polymerization occurs at the interface between immiscible solutions, where chemical kinetics govern the reaction. The interface acts as a boundary between the two phases, facilitating direct contact between monomers, leading to rapid polymerization and the formation of thin polymer films due to the low solubility of monomers.

Film thickness and structural properties can be fine-tuned by adjusting the concentration of monomers and oxidants. In the oxidative interfacial polymerization of conducting polymers, monomers polymerize through oxidative coupling. Traditional chemical oxidative polymerization tends to induce nucleation and secondary growth, which can lead to membrane development through this secondary growth if the polymer remains at the interface. However, when polymers disperse into the water layer, secondary growth is prevented, restricting polymerization to the interface alone. [3,58,93,97]

Numerous studies have demonstrated the application of microemulsion polymerization to produce polypyrrole (PPy). Microemulsion polymerization has been discovered to increase the yield of PPy nanoparticles, enhancing the degree of conjugation along the polymer backbone and the orderly organization of macromolecular chains. Feng et al. conducted a comparative analysis of PPy powders synthesized via solution, emulsion, and microemulsion polymerization using iron chloride ($FeCl_3$) as an oxidizing agent and sodium dodecylbenzene sulfonic acid (SDBA) and butanol as surfactant and co-surfactant, respectively.[98] Their experimental results concluded that

the microemulsion system is notably stable without any evident precipitation compared to the other two systems. Moreover, the yield of PPy powder was higher in the microemulsion polymerization system, along with enhanced conductivity and higher thermal stability. Qinghao Yang et al. synthesized freestanding self-assembled polypyrrole films using oil/water interfacial polymerization.[3] For the synthesis, they employed $FeCl_3$ and ammonium persulfate (APS) as oxidants, p-TSA as a dopant, Tween80 and Span80 as surfactants, and chloroform as the oil phase. The obtained films had a porous nature, and the researchers investigated the effect of temperature and surfactant on the morphology of the films. They concluded that the Tween80 surfactant, along with higher temperatures, facilitates the formation of pores and increases their size. Additionally, polymerization time was found to affect the morphology, with longer polymerization times resulting in thicker films. Films synthesized with Tween80 also exhibited better capacitance, cycling stability, and electrical conductivity, as shown in Figure 2.9.

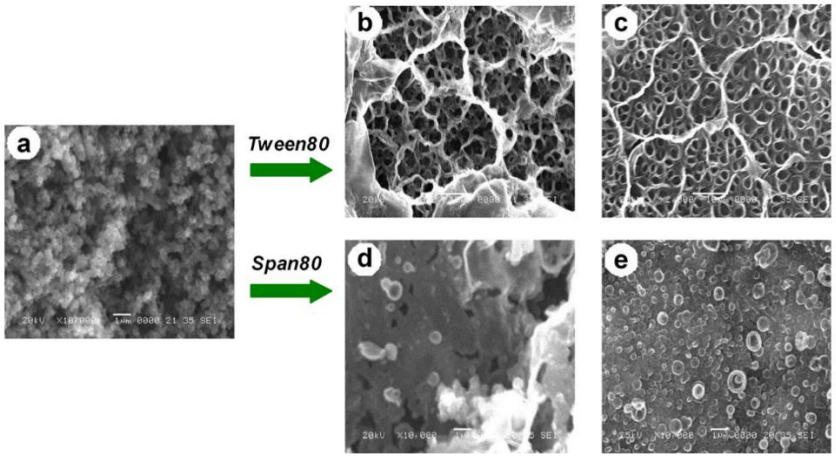

Figure 2.9. SEM images of PPy films synthesized without any surfactants and with Tween80, and Span80 as a surfactant at 25 °C and 0 °C.[3]

Guijin Qi and co-workers synthesized highly conductive and freestanding PPy films using the freezing interfacial polymerization (FIP) technique illustrated in Figure 2.10.[4]. For the synthesis, they used cyclohexane as the oil phase and iron chloride solution with p-TSA as an oxidant and doping agent. This technique achieved high conductivity, such as 2010 S/cm, and suggested that the films might possess longer conjugation lengths and more ordered structures. Lower temperatures resulted in a more ordered structure of the synthesized polymers, avoiding

unfavorable cross-linking, or branching. However, the obtained films were still mechanically unstable.

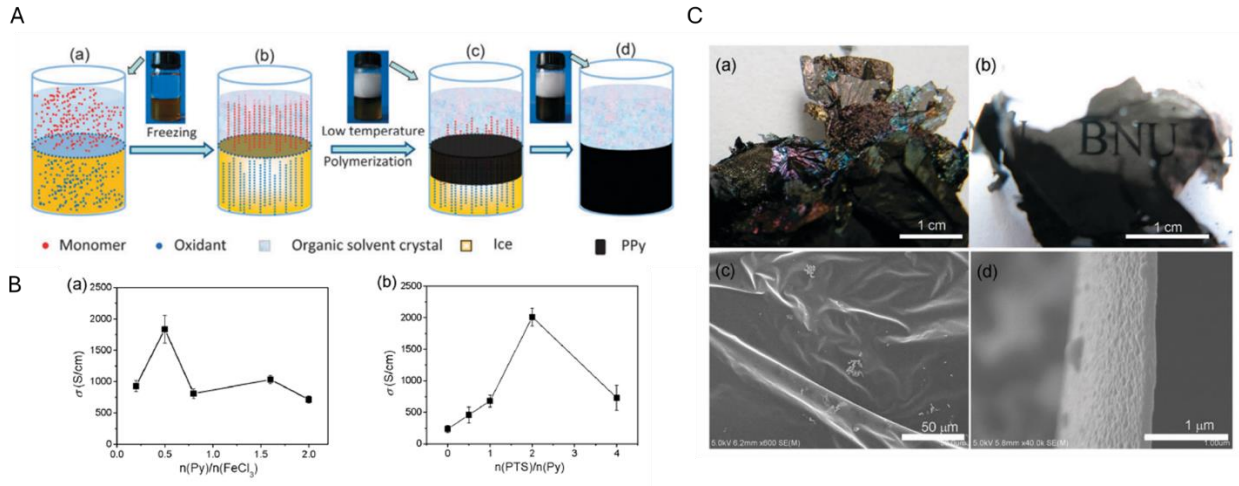

Figure 2.10. Schematic illustration of the FIP procedure with actual and SEM images of PPy films prepared with different molar ratios of pyrrole to $FeCl_3$.[4]

Yuanyuan Sun et al. synthesized flexible polypyrrole foams using a melamine template through in-situ interfacial polymerization.[5] They constructed MF/PPy composites, where melamine foam (MF) served as a template with a high surface area and as an excellent compressible skeleton. For the synthesis, they used iron chloride and p-TSA as the oxidant and dopant, respectively, with pyrrole monomer dissolved in cyclohexane as the oil phase. The MF was cut and immersed into the aqueous phase, followed by adding oil components every 4-5 minutes to achieve full foam coverage by polymer molecules. After polymerization, samples were washed and dried in a vacuum drying oven at 60 degrees for 12 hours. This composite material was used as an electrode for a symmetric supercapacitor, showing an areal capacitance of 2.685 F/cm^2. (Figure 2.11) Despite the excellent surface area and capacitance of template-assisted materials, they are not suitable for applications in smart, wearable, small-scale devices. Since, micro-sized devices require a more compact and thin architecture of the electrode, for better ion diffusion. The thicker and bulkier film slows down the ion exchange process.

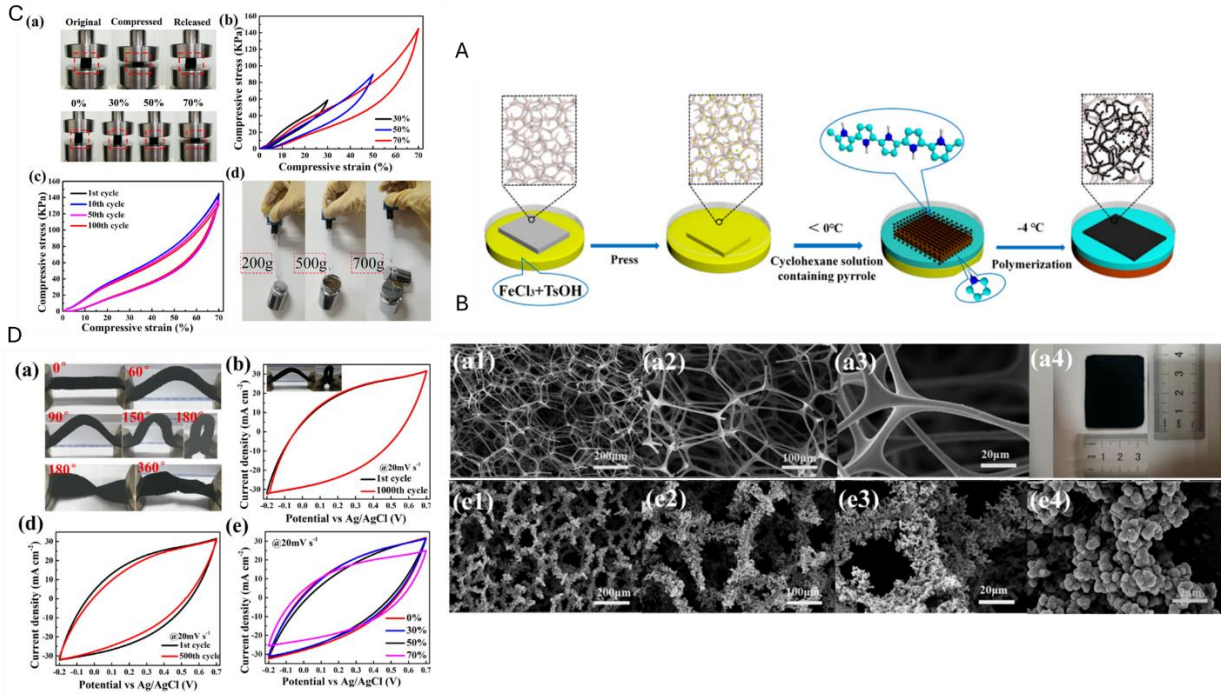

Figure 2.11 A schematic illustration of interfacial polymerization of MF/PPy composite with actual and SEM images of material and other characterization analysis results.[5]

2.3.3 Bicontinuous microemulsion polymerization.

Bicontinuous microemulsions (BMEs), also known as Winsor III MEs or middle-phase MEs, are characterized by their low viscosity, isotropy, thermodynamic stability, and spontaneous formation from mixtures of water, oil, and surfactants.[99] The dynamic morphology of BMEs is primarily determined by the hydrophilic-lipophilic balance (HLB) of the surfactants used in the system. When this balance is optimal, BMEs often exhibit a bicontinuous structure where water and oil phases coexist on a microscopic scale, as shown in Figure 2.7. In systems stabilized by neutral surfactants, achieving this bicontinuous phase can be challenging due to high sensitivity to temperature variations.[2] In contrast, ionic surfactant-stabilized systems are less temperature-sensitive, with the stability and phase behavior primarily influenced by the concentration of salts (electrolytes) and cosurfactants.

BMEs have garnered significant attention as templates for synthesizing polymeric materials with unique porous structures. Researchers have produced polymer blocks with continuous porous architectures by incorporating monomers as the oil phase and initiating polymerization through [100]

redox[101] and photo[102] initiators. These materials are valuable for applications such as monolithic columns and ultrafiltration membranes.

Recent advances have focused on the mesoscale structural control of self-supported swollen soft gels derived from BMEs. These include porous gels[103,104], composite gels[103,105], and bicontinuous gels [103,106], extensively studied for their potential in soft and self-assembly materials. (Figure 2.12) The gelation process within BMEs has led to the development of BME organogels, hydrogels, and hybrid gels, each exhibiting unique structural properties. The formation of these gels involves complex interactions and competition among several factors: the immobilization of the BME structure by gelation, mesoscopic phase separation during gelation, and the time-dependent transformation toward a thermodynamically stable structure.[107]

The resultant BME gels maintain their bicontinuous structure and exhibit ionic conductivity, indicating that the aqueous phase remains continuous within the composite gels. This continuity and structural integrity make BME gels promising candidates for novel soft material applications in electrochemistry and analytical fields. Studies on electrochemistry within BME gels have provided valuable insights into their mesostructures, including observations of structural changes and hysteresis, highlighting their potential as functional materials for advanced technological applications.[6]

Continuously porous conducting polymers provide numerous substantial benefits that expand their potential applications in various industrial and technological sectors. The porous structure of these materials enables efficient charge transfer and ion exchange, which is particularly advantageous for energy storage applications like supercapacitors and batteries due to their high surface area. This increased surface area provides more active sites for electrochemical reactions, resulting in higher capacitance and energy density[108]. Furthermore, the interconnected porous network within these polymers creates pathways for rapid electrolyte diffusion, thereby reducing resistance and facilitating quicker charge and discharge cycles.

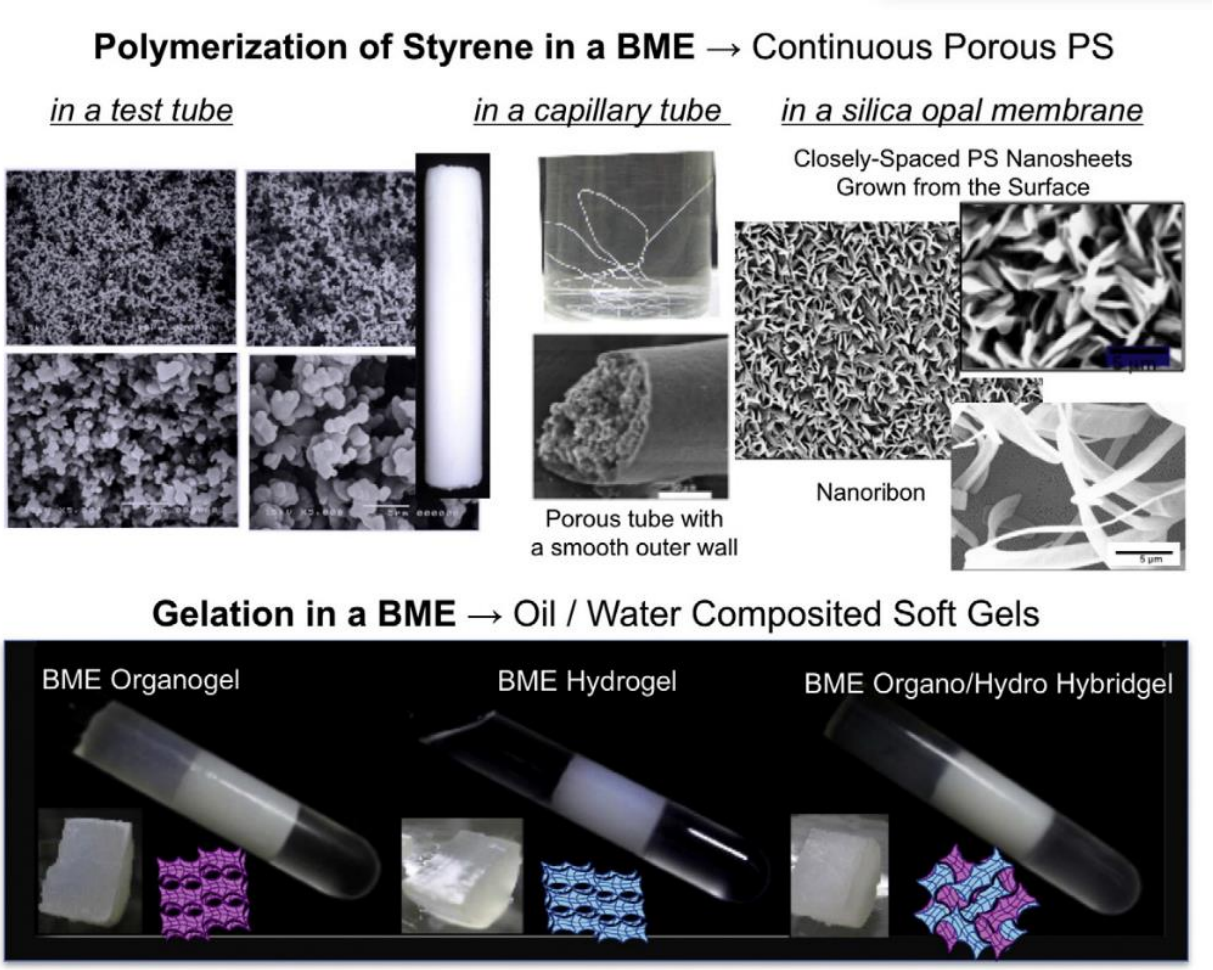

Figure 2.12. Different continuously porous polymer materials are synthesized by polymerization or gelation in BME solutions.[103]

Additionally, the catalytic activity of these materials is improved by their porosity. The large number of pores improves the overall efficiency of catalytic processes by increasing the exposure of catalytic sites. It makes them ideal for sensors, fuel cells, and other catalytic systems that need high activity and selectivity[109]. Continuously porous conducting polymers demonstrate exceptional structural integrity and mechanical flexibility, which are essential for creating flexible devices and wearable electronics. They are optimal for use in flexible batteries, stretchable sensors, and other bendable electronic components due to their capacity to preserve performance in the face of mechanical stress and deformation[110].

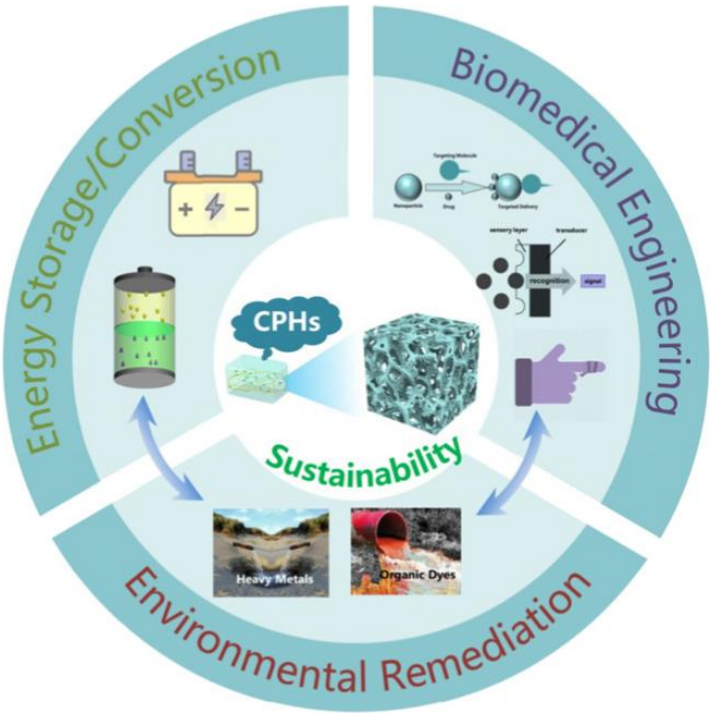

Figure 2.13. Areas of the main application for conducting polymer hydrogels.[6]

Furthermore, these polymers exhibit substantial potential for environmental applications. Their porous nature facilitates the effective adsorption and degradation of pollutants, making them useful in air filtration systems and water purification techniques. In addition to their potential for advanced energy storage systems and flexible electronic applications, continuously porous conducting polymers are also advantageous for environmental remediation and sustainable technologies due to their high surface area, enhanced electrochemical properties, and mechanical robustness.[6] The optimization of these materials could result in even greater efficiencies and broader applications as research advances, thereby reinforcing their role as a critical component of next-generation technologies.

2.4 Properties of conducting polymers

Conducting polymers have excellent physical and chemical properties, making them attractive for various applications. According to the nanoparticles incorporated into the polymer matrix, the inherent properties of CPs can be elevated and extended.

- **Mechanical properties**

The mechanical properties of polymer materials are mainly influenced by monomer structural arrangement and crystallinity. Additionally, macroscopic properties like pressure and temperature also affect the distribution of monomer units due to higher molecular motion in certain conditions.

When the temperature reaches the glass transition temperature T_g, the polymer changes to a rubbery state. As a result, the mechanical characteristics of the material also undergo some changes.[16] The toughness and strength parameters of conducting polymers depend on the molecular weight of the polymer, chain entanglement, and processing conditions.[111] While polymers may not have as high tensile strength as metals or ceramics, many techniques and synthesis strategies help improve the mechanical strength of CPs, such as crosslinking and blending with fillers, making them suitable for structural applications. Different carbon-based fillers are applied to synthesize mechanically stable hybrid conducting polymers, such as graphene and its derivatives, carbon nanotubes, polymer blends, and inorganic nanoparticles. The flexibility of CPs is attributed to the nature of the polymer chains. [16] Typically, conducting polymers have long, flexible polymer chains with relatively weak intermolecular forces, which allow them to bend and stretch easily. Including the fillers in the polymer matrix also positively affects the flexibility of the polymer material. However, the synthesis approach is also critical. Pristine and hybrid conducting polymers generally have elastic and viscoelastic properties, meaning they can flow or deform over time under constant stress. It also depends on the fabrication technique and composites used. Moreover, CPs are very attractive for industrial-scale production due to their processability and formability, allowing them to be shaped into various geometries using various processing techniques.[35] These techniques include solution casting, spin coating, 3D printing, and electrospinning. This versatility in processing enables the fabrication of CP-based films, fibers, coatings, and complex structures with tailored mechanical properties for specific applications.

- **Thermal stability**

The molecular structure of conducting polymers, the nature of the doping agents, and the synthesis method employed strongly influence the thermal stability of polymer materials. Polymers with highly conjugated backbones commonly show better thermal stability due to aromatic rings and strong intermolecular interactions, such as p-p stacking.[82] The addition of stabilizing composites to the polymer matrix, such as antioxidants (phenols, phosphites), fillers (silica, titanium dioxide), nanoparticles (graphene, metal oxides), and polymeric blends (polyimides, polyurethanes, epoxy resins), may also improve the thermal stability of conducting polymers.[84] The higher thermal resistance is essential for applications exposed to harsh thermal conditions, such as high-temperature gas sensors, automotive electronics, and aerospace components. However, it should

be noted that excessive thermal exposure can lead to the degradation of polymer chains, resulting in a loss of mechanical properties and conductivity.

- **Optical properties**

The delocalized p-electron system along the conjugated backbone of CPs allows them to absorb and emit light across various wavelengths. Structural modifications, the doping level, and the molecular weight of the polymer can also adjust the optical absorption. The transition from insulation to a conducting state affects the changes in the optical properties. [70] This property is valuable for electrochromic devices, light-emitting diodes, or smart windows. The fluorescence and photoluminescence properties make them ideal candidates for light-emitting diodes (LEDs), organic photovoltaics (OPVs), and sensors.[112]

- **Chemical and environmental stability**

Crosslinked polymers are well known for their exceptional resistance to chemical and environmental degradation, making them highly suitable for use in harsh conditions. Their molecular structure heavily influences the stability of CPs to the specific dopant employed, and the inclusion of stabilizing additives or coatings. Due to their conjugated backbones and aromatic rings, CPs such as polyaniline (PANI) and polythiophene (PTh) have excellent chemical resistance. These structural features confer intrinsic stability against oxidation and reduction reactions. However, degradation can still occur due to exposure to strong acids, bases, or oxidative environments, resulting in a loss of mechanical properties and conductivity. CPs can be influenced by factors such as humidity, temperature, and UV radiation, which can affect their stability. Other techniques are utilized, such as applying protective coatings, adding stabilizers, and combining with more stable polymers. For example, UV stabilizers and antioxidants can significantly enhance the durability of CPs against the effects of photodegradation and oxidative stress.[40,112] Moreover, encapsulating them within inorganic matrices or creating composites with nanoparticles can significantly improve their ability to block environmental pollutants. Enhancing the chemical and environmental durability of CPs is essential for their sustained use in areas like electronics, sensors, and protective coatings. It will guarantee consistent performance and reliability even in different environments.[6]

- **Redox activity**

The exceptional redox activity of conducting polymers is a fundamental property that drives their broad spectrum of applications in electronic and electrochemical devices. The redox activity of

CPs is defined as their capacity to undertake reversible oxidation and reduction reactions, which enables them to shift between various oxidation states. Their polymer backbone contains conjugated π-electron systems, which facilitate the transfer of electrons during redox processes. Polypyrrole (PPy), polythiophene (PTh), and polyaniline (PANI) are among the most extensively investigated CPs for their redox properties. In PANI, for example, the polymer can switch between leucoemeraldine (completely reduced), emeraldine (partially oxidized), and pernigraniline (totally oxidized) states, each with its own electrical and visual characteristics.[113] This reversible redox switching is essential for applications such as electrochemical sensors, supercapacitors, and rechargeable batteries, where the material's capacity to store and discharge charge efficiently is the highest priority. Additionally, the redox activity of CPs is influenced by the morphology of the polymer, the nature of the dopant, and the electrolyte used in the electrochemical environment. Doping introduces charge carriers into the polymer matrix, increasing conductivity and redox responsiveness. For instance, dopants such as camphor sulfonic acid can substantially enhance PANI's redox kinetics and stability. Additionally, the redox properties of CPs can be further improved by nanostructuring conducting polymers into nanowires, films, or composites, which enables more efficient electron and ion transport and increases the surface area.

- **Charge storage capacity (Pseudocapacitance)**

Polyaniline (PANI), polypyrrole (PPy), and polythiophene (PT) are conducting polymers with conjugated backbone architectures that allow for electron delocalization. This electrical structure supports the doping process by allowing the polymer to accept or donate electrons, thereby storing charge. Oxidation or reduction of the polymer occurs during the charging process, which involves the incorporation of ions from the electrolyte to preserve electrical neutrality. This process, known as ion intercalation, dramatically increases the material's capacitance.

Conducting polymers exhibit pseudocapacitance due to their reversible oxidative processes at or close to the electrode surface.[42] In contrast to conventional capacitors, which store energy through electrostatic interactions, pseudocapacitors utilize faradic processes. These processes are distinguished by their rapid charge and discharge cycles, facilitated by their fast kinetics.[33,110] Conducting polymers exhibit a substantially higher specific capacitance than conventional capacitors due to the additional charge storage caused by redox reactions.

The high capacitance, lightweight nature, and flexibility of conducting polymers make them highly advantageous for use in supercapacitors. They are employed in applications requiring rapid energy

delivery and storage, including portable electronics, electric vehicles, and smart devices. Conducting polymers are well-suited for wearable and flexible electronics due to their mechanical flexibility and capacity to operate within a broad temperature range.[29]

- **Sensitivity**

Conducting polymers are employed in various applications, such as industrial safety, environmental monitoring, medical diagnostics, and product quality control. Recent developments in the field include forming wearable and flexible gas sensors, integrating wireless communication systems for IoT applications, and improving sensitivity and selectivity through nanostructuring and composite formation.[30,37,114] The primary mechanism of gas sensing in conducting polymers involves adjustments in the polymer's electrical conductivity as it interacts with gas molecules. A change in the charge carrier concentration and, as a result, the electrical conductivity of the polymer can result from the donation or acceptance of electrons by a gas molecule when it interacts with the polymer.[41,74]

Conducting polymers possess a high surface area and the capacity to establish various interactions with gas molecules, such as hydrogen bonding, van der Waals forces, and π-π interactions. The adsorption of gas molecules onto the polymer surface depends on these interactions. The doping level of conducting polymers can be modified through the adsorption of gas molecules. For example, the conductivity of the polymer can be enhanced by electron-donating gases (such as ammonia) and decreased by electron-reducing gases (such as nitrogen dioxide).[115] The target gas concentration is detected and measured by this change in conductivity. Additionally, conducting polymers can be modified to be selective for particular gases by manipulating their chemical structure or incorporating functional groups that interact preferentially with the target gas. Doping with metal nanoparticles or combining with other polymers frequently improves the sensitivity of conducting polymer-based gas sensors.[114] The capacity of conducting polymers to endure reversible changes in conductivity is a critical property for gas sensing. This reversibility guarantees that the sensor can be repurposed numerous times without experiencing a substantial decrease in performance. The polymer's stability under various environmental conditions is also essential for practical applications.

CHAPTER 3. METHODOLOGY

3.1 Introduction

Different polymerization techniques can achieve various structural morphologies of conducting polymers. However, making uniform freestanding conducting polymer multifunctional films and porous template-free conducting hybrid gels is still tricky. We developed a scalable and straightforward synthetic approach for creating zero-dimensional (0D), two-dimensional (2D), and three-dimensional (3D) freestanding conducting polymer hybrid materials to address these challenges.

This study selected pyrrole as an ideal monomer candidate due to its structural versatility and adaptability to interface changes. Polypyrrole is a positively charged, nontoxic, and biocompatible heterocyclic polymer with oxidized nitrogen.[59] It is electroactive in both organic electrolytes and aqueous solutions.

The morphology of polypyrrole, especially its 2D and 3D structures, is a crucial parameter that strongly correlates with its functional properties. Two-dimensional materials are sheet-like nanomaterials with superior structure-property performance compared to zero-dimensional (0D) or one-dimensional (1D) structures. These materials possess excellent flexibility and optical, thermal, and electrical properties, making them suitable for integration into various devices with improved durability and mechanical stability. Additionally, their high surface area-to-volume ratio enhances their interaction with other substances. The atomic-scale thickness of 2D materials allows precise control over electrical and optical properties, which is crucial for advanced electronics applications. Despite the exceptional properties of 2D materials, 3D conducting polymers offer significant improvements due to their unique architecture.

The enhanced surface area of 3D interconnected networks facilitates efficient charge transport pathways, reducing resistance and enhancing the overall electrical conductivity of the material. The porous nature of 3D materials is crucial for energy storage applications, where electrode-electrolyte interactions are essential parameters that affect better ion exchange, high capacitance, and charge-discharge performance. Furthermore, 3D materials offer improved mechanical strength and flexibility, which are valuable for flexible electronics and wearable devices.[116] Tree-

dimensional architecture integrates well with other composites and allows for easy functionalization with various chemical groups or nanoparticles.

Traditional methods of synthesis of 2D and 3D conducting polymers face challenges such as controlling the morphology and uniformity of the polymer structure, which in turn impacts the material's electrical performance. Issues with template removal during template-assisted polymerization and limitations in developing freestanding nanosheets with high electrical conductivity also exist.[117] Achieving a high degree of polymerization and conductivity while maintaining processability and stability remains a complex task. Furthermore, conventional synthesis techniques involve multiple steps, use hazardous chemicals, and generate considerable waste, posing environmental and scalability concerns.

The bicontinuous microemulsion polymerization method presents a promising approach for synthesizing 2D and 3D PPy structures.[109] This method leverages the unique properties of microemulsions—thermodynamically stable mixtures of oil, water, and surfactants—to create a versatile and controllable environment for polymerization. The bicontinuous nature of these microemulsions provides a continuous network of both oil and water phases, facilitating the formation of complex polymer architectures without the need for templates or molds.

This study proposes a novel synthesis approach using bicontinuous microemulsion polymerization to fabricate 2D and 3D PPy structures. By manipulating key parameters such as oxidant concentration, surfactant type, and water-to-oil ratios, we aim to control the morphology and properties of the resulting ьmaterial precisely. This method simplifies the synthesis process and enhances the material's structural and functional characteristics. The introduction of this synthesis technique has the potential to overcome existing limitations and expand the application scope of polypyrrole.

Our work focuses on understanding the influence of various synthesis parameters on the morphology, porosity, and electrical properties of the PPy structures. Additionally, we investigate the potential applications of these novel PPy materials in areas such as flexible electronics, energy storage devices, and environmental sensing.

3.2 Fabrication of 2D PPy films

3.2.1 Materials

Pyrrole (≥98%, Sigma-Aldrich), cyclohexane (≥99%, Sigma-Aldrich), Triton X-100 (Sigma-Aldrich), n-butanol (99.8%, Sigma-Aldrich), anhydrous iron (III) chloride, FeCl3 (Sigma-Aldrich), p-Toluene sulfonic acid monohydrate, p-TSA (≥99%, Sigma-Aldrich), ammonia persulfate, APS (≥98.0%, Sigma-Aldrich), dichloromethane, DCM (anhydrous, ≥99.8%, Sigma-Aldrich), ethanol (absolute for analysis EMSURE, Sigma-Aldrich), benzene (≥99%, Sigma-Aldrich), cetyltrimethylammonium bromide, CTAB (≥98.0%, Sigma-Aldrich), sodium dodecyl sulfate, SDS (≥ 99 %, Sigma-Aldrich). Pyrrole was purified before use in an acidic aluminum chloride column.

3.2.2 Experimental section

In this work, the polymerization of conducting polymers at four different microemulsion interfaces, based on the type of surfactant applied—nonionic, pure (without surfactant), cationic, and anionic—was studied. Four ternary phase diagrams with bicontinuous microemulsion regions were investigated. Pyrrole monomer was freshly distilled under reduced pressure before use.

In this work, microemulsions with a certain concentration of oil, water, and surfactant obtained from the region on the phase diagram were mixed and named a bicontinuous nanoreactor.

Interfaces studied to synthesize 2D polypyrrole films:

- *nonionic surfactant system* - cyclohexane/Triton X-100/n-butanol/water
- *surfactant-free system (pure)* - ethanol/benzene/water and ethanol/dichloromethane/water
- *cationic surfactant system* - cetyltrimethylammonium bromide (CTAB)/n-butanol/water
- *anionic surfactant system* - sodium dodecyl sulfate (SDS)/butanol/water

- ***The nonionic surfactant system consists of the oil-surfactant/co-surfactant-water phases (cyclohexane, Triton X-100/n-butanol/ water.***

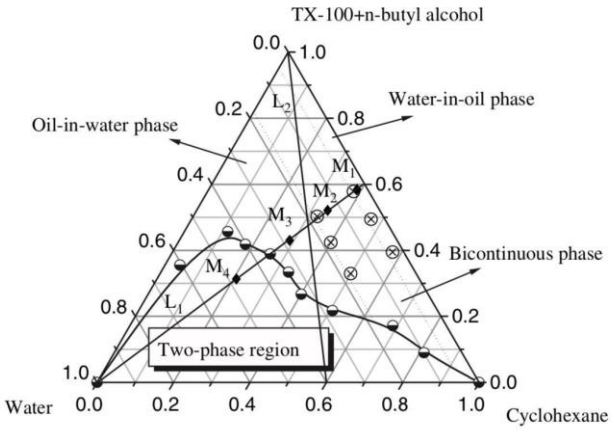

Figure 3.1 Pseudo-ternary phase diagram of the TX-100/n-butanol/cyclohexane/water reactor system at 25 C.[7]

- ***Preparation for synthesis.***

Preparatory work should be carried out before polymerization proceedings. The quick-check analyses were conducted to ensure that the selected region on the phase diagram is bicontinuous (BC). The evident difference in the BC region from W/O or O/W is in the transparency of the system after mixing all components (Figure 4.2). During this work, the optimal oil-to-monomer solubility ratio of 80:20 wt% was identified. After selecting the proper investigation areas, the monomer was introduced to the BME system.

Figure 3.2. Quick-check analysis of different nanoreactors without the addition of monomers to the system (nonionic system).

- ***Synthesis of 2D PPy films by the pseudo-ternary phase diagram of the nonionic surfactant system with TX-100/n-butanol/cyclohexane/water.***

In the standard experimental protocol, the pyrrole monomer was freshly distilled before use. Iron (ii) chloride ($FeCl_3$), with concentrations ranging from 2 to 20 mg/mL, or ammonium persulfate (APS), with concentrations from 1 to 15 mg/mL, was dissolved in DI water as an oxidant in the aqueous solution. Hydrochloric acid (HCl) was employed as a doping agent to adjust the acidity of the water fraction, maintaining a pH between 1 and 1.5. A surfactant solution of Triton X-100 and n-butanol in a 1:1 mass ratio was prepared. The monomer was dissolved in cyclohexane with an oil-to-monomer weight ratio of 80:20. Subsequently, three components were combined and mixed to establish a bicontinuous microemulsion, which was then left at room temperature for 24 hours to complete the polymerization reaction. The formed black films and powders of the polypyrrole were thoroughly washed with acetone to remove any unreacted oil and surfactant residues.

A systematic analysis of all points in the bicontinuous region was studied. The nanoreactor compositions are presented in Table 3.1. Table 3.2 shows the weight ratio distribution of reactor two as an example. The oil composition remains the same with the same monomer concentration; however, the water and surfactant concentrations were changed, respectively.

Table 3.1. Weight ratio composition of the nonionic surfactant system nanoreactors.

Reactor	Oil, wt%	Water	Surfactant/Co-surfactant
R1	40	5	55
	40	10	50
	40	20	40
	40	30	30
R2	50	5	45
	50	10	40
	50	20	30
R3	60	5	35
	60	10	30
	60	20	20
R4	80	5	15

Table 3.2. Monomer to Water weight ratio change in the Reactor.

Rector 1	Wt.%	Wt.%	Wt.%

	Overall oil (50%)	**Overall oil (50%)**	**Overall oil (50%)**
Oil: Monomer (80:20)	40:**10**	40:**10**	40:**10**
Surfactant/Co-surfactant	45	40	30
Water	**5**	**10**	**20**

- ***Synthesis of 2D PPY films by the pseudo-ternary phase diagrams of the surfactant-free systems with ethanol/benzene/water and ethanol/dichloromethane/water.***

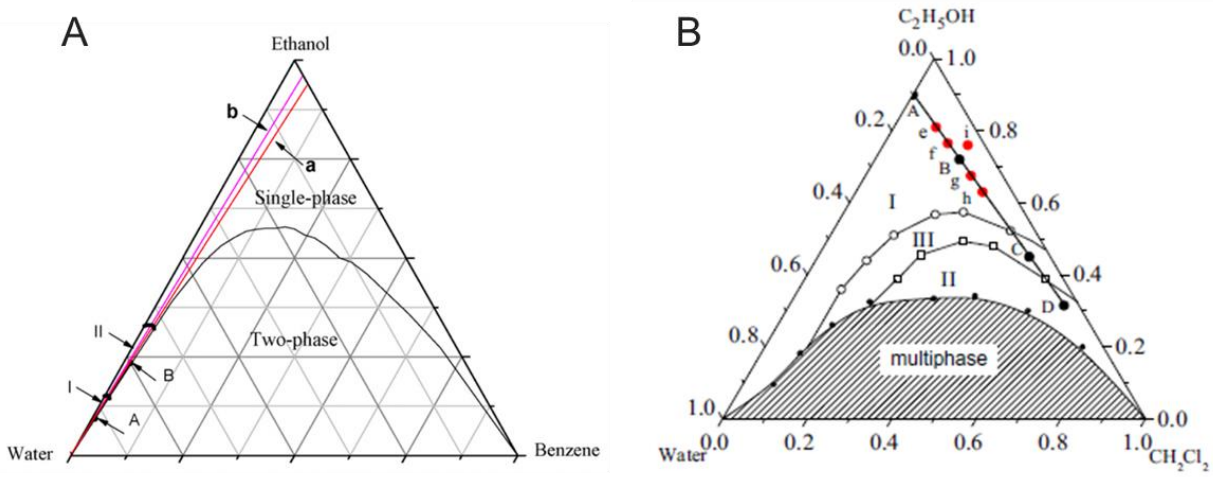

Figure 3.3. A. Phase diagram of benzene/ethanol/water ternary system at 25 C.[118] B. Phase diagram of DCM/ethanol/water ternary system at 25 C.[119]

Quick-check analyses were carried out to ensure the selected regions on the phase diagram are bicontinuous (BC). The synthesis of PPY in the dichloromethane/ethanol/water system followed the next procedure: from the phase diagram, three points with different water, ethanol, and dichloromethane mass ratios were selected, as shown in Table 3.3. Calculated amounts of monomer (oil: monomer ratio is 80:20 wt%) dissolved in dichloromethane and oxidant (5 mg/ml $FeCl_3$) were used for polymerization. The fabricated PPy films were washed with acetone to eliminate surfactant and oil residues. Only one point was selected for the benzene/ethanol/water system due to the very small BC region on the diagram. The nanoreactor comprises 30 wt% of

ethanol, 1 wt% of Benzene, and 69 wt% of water. The APS and $FeCl_3$ oxidants with concentrations of 2 and 5 mg/ml with pH 1.5 were tested.

Table 3.3. Selected points in the bicontinuous DCM/ethanol/water nanoreactor system.

Reactor	Oil: monomer ratio wt.%	Oil:water ratio wt%	Oxidant	Oxidant concentration
1	80:20	18:40	$FeCl_3$	5 mg/ml
2		25:23		
3		47:5		

- ***Synthesis of 2D PPy films by the cationic (CTAB) and anionic (SDS) surfactant reactor systems.***

As cationic and anionic interfaces, cetyltrimethylammonium bromide (CTAB)/n-butanol/cyclohexane/water and sodium dodecyl sulfate (SDS)/butanol/cyclohexane/water bicontinuous microemulsion systems were used. These systems facilitated the formation of bicontinuous microemulsions by the strategic combination of essential components. According to the literature, the composition of cationic microemulsion included 17.5 wt% CTAB, 35 wt% n-butanol, 12.5 wt% cyclohexane, and 35 wt% water. Conversely, the anionic system comprised 8 wt% SDS, 26.7 wt% butanol, 13.3 wt% cyclohexane, and 52 wt% water.[120] In both systems, the ratio of oil to monomer was maintained at 80:20 wt%, with pyrrole dissolved in the oil. Polymerization was initiated using 5 mg/mL $FeCl_3$, forming PPy black nanosheets and powders, which were subsequently cleansed with acetone to remove any unreacted oil and surfactant residues. For the preparation of 50 g of the cationic microemulsion, 8.75 g of CTAB was dissolved in 17.5 g of water, and 6.25 g of cyclohexane was added to the surfactant solution, after which the solution became turbid. After that, 17.5 g of n-butanol was added and stirred continuously until a clear and stable solution was achieved. Anionic microemulsion with SDS was prepared by dissolving 4 g of SDS in 26 g of water and 6.65 g of oil, and the liquid became turbid after mixing. After this, 13.35 g n-butanol was added under constant stirring until the solution became clear and stable.

3.3 Fabrication of 3D PPy Composites.

The 3D polypyrrole soft gels were synthesized using the ternary nonionic interface bicontinuous microemulsion polymerization method.

For the synthesis of 3D polypyrrole soft gel, different BC points and reactor compositions were studied, however as it was in case with 2D PPy, gels synthesized by 50/20/30 ratio of the nonionic interface demonstrated superior electrical properties. The reactor components can be easily adjusted to scale up the synthesis from small vials to larger bottles with varying diameters.

Oil-to-monomer ratio in the oil phase was 80:20 wt%, and to obtain a BME: 34.2 ml of cyclohexane, 6.9 ml of pyrrole, 21.6 ml of surfactant solution (triton X-100/n-butanol), and 13.3 ml of oxidant solution containing of equal molar concentrations of $FeCl_3$ and p-TSA (0.36 M) were mixed left to stabilize for 24 hours. Adding the aqueous solution at the end is crucial to ensuring fast polymerization. Right after the oxidant was added, the liquid quickly became black, signifying the start of the polymerization process. The obtained gel was cleansed by vigorously rinsing it with acetone and deionized (DI) water. Removing any remaining oil and surfactant residues was a crucial step to guaranteeing the quality of the final 3D polypyrrole product. The final product was dried in a vacuum oven at 80 degrees for 5 hours.

3.4 Synthesis of PPy@Ag/Co_3O_4 Ternary composite.

The Co_3O_4 nanoparticles were prepared using a hydrothermal reaction method. Initially, 0.237 g of $CoCl_2 \cdot 6H_2O$ was dissolved in 35 ml of DI water. 15 ml of 6% NH_4OH was added dropwise at a 1 ml/min rate to that solution. This mixture was stirred constantly for 1 hour at RT.[121] The resulting 50 ml mixture was transferred into a 100 ml Teflon-lined stainless-steel autoclave, where the hydrothermal reaction was conducted at 150 ℃ for 5 hours. The solid particles that developed after this reaction were gathered, rinsed many times with deionized water and ethanol using centrifugal force, and subsequently dehydrated at 100 ℃ in an oven for 12 hours. To synthesize the PPy@Ag/Co_3O_4 ternary nanocomposite, 0.169 g of $AgNO_3$ (5 wt. % of $CoCl_2 \cdot 6H_2O$) was introduced into the Co_3O_4 nanoparticles that had been synthesized earlier, while stirring continuously. The mixture underwent the identical hydrothermal conditions as previously described: the 50 ml mixture was placed into a 100 ml Teflon-lined stainless-steel autoclave, and the reaction was conducted at a temperature of 150 ℃ for a duration of 5 hours. The solid particles were gathered, cleansed via repeated centrifugation with deionized water and ethanol, and subsequently dehydrated at a temperature of 60 ℃ in a hot air oven. The nanoparticles that were

acquired were introduced into the monomer while undergoing BME polymerization. The reactor composition was 50/20/30 with oil-to-monomer ratio 80:20 wt%. The $FeCl_3$ oxidant concentration was 2 mg/ml and a pH of 1.5.

3.5 Synthesis of 3D PPy-Linker-N-CDots.

3.5.1 Synthesis of the Sebacoyl-Pyrrole Linker.

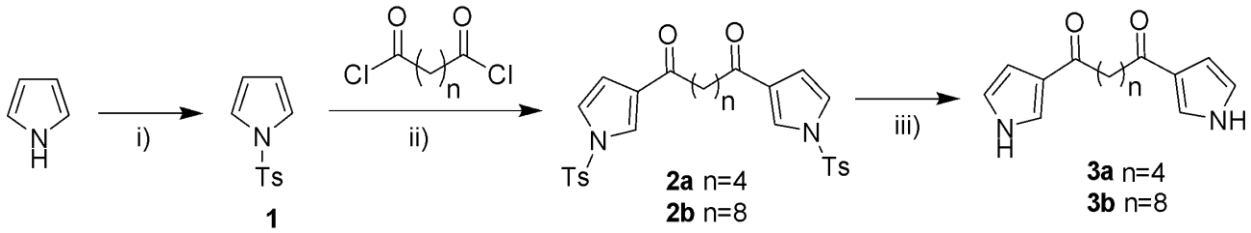

Scheme 3.1. A three-step process employed for the synthesis of the pyrrole dimers.[122]

(IV-A). ***N-p-Toluenesulfonylpyrrole (I).***

In THF (350 ml), pyrrole (10 g), KOH (16.74 g), and tosyl chloride (26.7 g) were prepared. The solution underwent reflux for a duration of four hours and was thereafter cooled to room temperature. Following this, diethyl ether (250 mL) was introduced, and the resulting mixture was transferred to a separatory funnel. The reaction mixture was rinsed with large quantities of water (3*250 mL), then with a saturated NaCl solution (2*200 mL). The organic layer was isolated, dehydrated using magnesium sulfate, filtered, and the solvent was evaporated under low pressure. The obtained grey solid was subjected to recrystallization using 60 mL of methanol, resulting in the formation of the intended fine white powder weighing 11.12 g.

(**IV-B**). ***Synthesis of the N-tosylpyrrole-2 alkyl compounds (II).***

In a nitrogen-filled room, 1.65 grams of adipoyl chloride or sebacoyl chloride in dry CH2Cl2 (20 mL/g) was added one part at a time to a solution of 2.67 grams of AlCl3 in dry CH2Cl2 (20 mL/g of AlCl3). It was cooled to 0 C after 10 minutes, and over the next 5 minutes, drops of a solution of 4.43 grams of N-tosyl-pyrrole in 10 milliliters of CH2Cl2 were added all at once. The solution had been stirred at a temperature of 0 °C for 2 hours, after which ice water was gently introduced. The resulting product was then extracted using diethyl ether in three separate portions of 200 mL each. The organic components were mixed, dehydrated using magnesium sulfate (MgSO4), separated using filtration, and the solvent was eliminated using decreased pressure. The findings

were purified using column chromatography utilizing a mixture of petroleum hexane and ethyl acetate (at a ratio of 3:2) as the eluent.

(IV-C). ***Synthesis of the pyrrole-2-alkyl compounds (III).***

An aqueous solution of 5 M NaOH was added to the mixture and left overnight. The mixture was then combined with a tosyl-protected pyrrole (1b) that had been dissolved in 100 mL/g of 1,4-dioxane. The solution was cooled and subjected to extraction using diethyl ether (3*100 mL). The organic substances were mixed and dehydrated using magnesium sulfate (MgSO4), and the solvent was evaporated using decreased pressure. The resulting products 1c were purified by column chromatography employing a hexane/ethyl acetate (3:2) mixture as the eluent.

3.5.2 Synthesis of 3D polypyrrole with linker composite.

A nonionic surfactant system was used to make 3D PPy, and ferric chloride was used as an oxidant in four different concentrations: 2 mg/mL, 5 mg/mL, 10 mg/mL, and 15 mg/mL. Two reactors were selected for this purpose, altering the monomer concentration to 10 wt%. To examine morphological changes, three mass ratios of monomer to linker were chosen: 0.25 wt%, 0.5 wt%, 1.0 wt%, and 4 wt%. To study the effect of the carbon length of linkers on the morphology of the obtained polymers, we used two carbon lengths of 6 and 10: adipoyl chloride and sebacoyl chloride. The reactor composition with linkers is presented in Table 6.2.

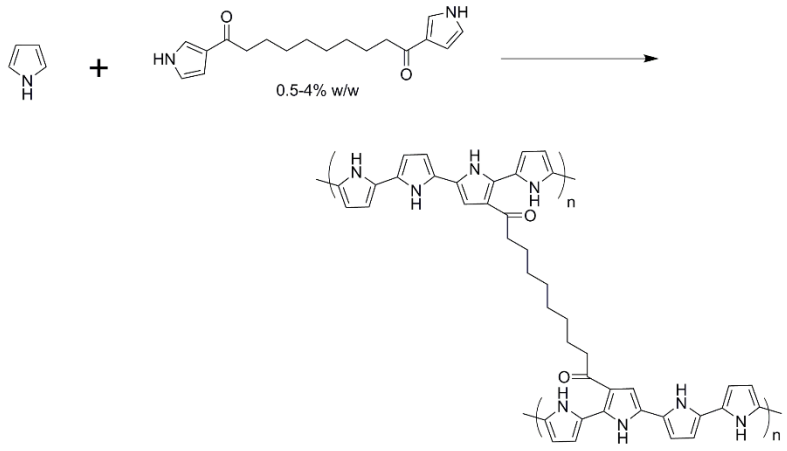

Scheme 3.2. The synthesis procedure of the PPY linker with sebacoyl chloride and adipoyl chloride.

3.5.3 Synthesis of N-Carbon Dots.

The synthesis of Nitrogen-doped Carbon Dots followed the procedure described in the literature.[123] Briefly, citric acid (1.4 g) and ethylenediamine (1787 µL) were dissolved in DI-water (33.3 mL) under vigorous stirring. Then, the solution was transferred to a poly(tetrafluoroethylene) (Teflon)-lined autoclave (50 mL) and heated at 250 °C for 5 h. After the reaction, the reactor cooled to room temperature naturally. The brown-black and transparent products were filtered and subjected to a dialysis tube to obtain pure CDs. The synthesized blue carbon dots have a 41% quantum yield fluorescence.

3.5.4 Synthesis of 3D PPy-Linker-N-CDs.

To synthesize 3D polypyrrole, a pure interface (surfactant-free system) was employed to avoid quenching the carbon dots with the iron chloride solution. Therefore, a benzene/ethanol/water (BME) system was used, with ammonium persulfate (APS) as the oxidant and hydrochloric acid (HCl) as the doping agent. Nitrogen-doped carbon dots (N-CDots) were added to the oxidant solution at the very end of the microemulsion formation process.

Table 3.4. The design of an experiment for 3D porous PPY fabrication with Sebacoyl chloride.

Types of Linkers	Linker weight %	Oil:Water ratio	Surfactant	Oxidant	Oxidant concentration
Adipoyl Linker	4%	50:10	Triton X-100/Butanol	$FeCl_3$	5 mg/ml
	1%				
	0.5%				
	0.25				
Sebacoyl Linker	4%	50:10	Triton X-100/Butanol	$FeCl_3$	5 mg/ml
	1%				
	0.5%				
	0.25%				

3.6 Fabrication of 3D PPy-CoO soft gel.

3.6.1 Materials

Pyrrole (≥ 98%, Sigma-Aldrich), cyclohexane (≥ 99 %, Sigma-Aldrich), Triton X-100 (Sigma-Aldrich), n-butanol (99.8 %, Sigma-Aldrich), anhydrous iron (III) chloride (Sigma-Aldrich), p-Toluene sulfonic acid monohydrate, and pTSA (≥ 99%, Sigma-Aldrich). Pyrrole was purified by acidic aluminum oxide column before use.

Poly(vinyl alcohol) (M_w 89,000-98,000, Sigma-Aldrich), sulfuric acid (95–98%, Sigma-Aldrich), Poly(vinylidene difluoride) (PVDF, ≥ 86%, Sigma-Aldrich), *N*-Methyl-2-pyrrolidone (NMP, 99.5%, Sigma-Aldrich), acetylene black.

Cobalt (II) oxide (CoO) (Sigma-Aldrich).

3.6.2 Preparation of 3D PPy-CoO gel.

The synthesis of polypyrrole-cobalt oxide composite was carried out under the same procedures as that of pure 3D polypyrrole gels. In this case, different concentrations of cobalt oxide (0.5 wt%, 1.0 wt%, and 3 wt%) were mixed with pyrrole monomer at the beginning of the reaction, followed by the addition of other components (cyclohexane, surfactant, and oxidant solution).

3.6.3 Fabrication of 3D PPy and 3D PPy-CoO micro-pseudocapacitors (MPCs).

The working electrode was prepared using the slurry casting method. The slurry is composed of 80 wt% of active material (pure PPy or nanocomposites PPy-CoO), 10 wt% of acetylene black, and 10 wt% of PVDF with ≤ 1 ml of NMP (based on the total mass of the electrode). The obtained slurry was cast by a doctor blade on the PET/Cr/Au substrate with a thickness of 30 μm and dried under vacuum at 100 °C for 5 hours. The electrolyte was a PVA/H_2SO_4 solution prepared as follows: 1 g of PVA was dissolved in 10 ml of deionized water and stirred for 2 hours at 95 °C until complete dissolution of the PVA. After cooling the solution, 1 g of sulfuric acid was added and stirred overnight.

The bicontinuous nature of the system facilitates the formation of the 3D porous network of PPy with CoO nanoparticles, resulting in a composite soft gel with enhanced electrochemical, mechanical, and structural properties, which are crucial for high-performance supercapacitor applications. The porous nature of the electrode material is essential in developing energy storage devices due to its ability to facilitate ion transport and accommodate volume changes during electrochemical cycling stability tests.

3.7 Fabrication of 3D PPy-Graphene composite gel.

3.7.1 Materials

Pyrrole (≥ 98%, Sigma-Aldrich), cyclohexane (≥ 99 %, Sigma-Aldrich), Triton X-100 (Sigma-Aldrich), n-butanol (99.8 %, Sigma-Aldrich), anhydrous iron (III) chloride (Sigma-Aldrich), p-Toluene sulfonic acid monohydrate, and p-TSA (≥ 99%, Sigma-Aldrich), graphene nanoflakes (China). Pyrrole was purified before use. Deionized (DI) water was used throughout the experiments.

Poly (vinylidene difluoride) (PVDF, ≥ 86%, Sigma-Aldrich), *N*-Methyl-2-pyrrolidone (NMP, 99.5%, Sigma-Aldrich), acetylene black.

3.7.2 Synthesis of 3D PPy-Graphene composite.

The synthetic approach was the same as for the PPy-CoO composite. The 50/20/30 nonionic bicontinuous nanoreactor was selected with an 80:20 wt.% ratio of oil-to-monomer. $FeCl_3$=p-TSA=0.36 M. Three composite gels were synthesized, such as Ppy-Gr 0.5wt.%, Ppy-Gr 1.5wt%, and Ppy-Gr 3.0 wt.%.

3.7.3 Fabrication of flexible gas sensor.

A polymer slurry was prepared using the method described in previous work. Briefly, the slurry consisted of 80 wt.% polypyrrole-graphene (PPy-Gr), 10 wt.% acetylene black, and 10 wt.% polyvinylidene fluoride (PVDF). The solvent N-methyl-2-pyrrolidone (NMP) volume was adjusted based on the loaded mass, not exceeding 2 ml. The sensor substrate was polyethylene terephthalate (PET) coated with a 100 nm layer of chromium/gold (Cr/Au). The electrodes were fabricated using laser cutting. Subsequently, the prepared slurry was cast onto the electrode using the Doctor Blade technique. The sensors were then dried under vacuum at 100°C for 5 hours.

3.8 Characterization techniques.

- **Morphology analysis**

All investigated materials' morphology images and surface analysis were studied with scanning electron microscopy (SEM) using the ZEISS Crossbeam 540 and transmission electron microscopy (TEM) from the JEOL JEM-1400 Plus. Samples were coated with a 5 nm layer of gold for SEM imaging. The surface roughness of the synthesized materials was investigated using a complex AFM spectrometer (Horiba LabRam Evolution). A profilometer from the Dektak XT

Stylus Profiler was used to study the thickness and additionally gave valuable insights into roughness.

- **Structural analysis**

The structural and molecular analysis of synthesized materials was carried out by the Fourier transform infrared (FTIR) technique using a Nicolet iS10 spectrometer and a Raman spectrometer from Horiba LabRam Evolution. The IR spectra were collected in the wavenumber range 400-4000 cm-1, and the Raman spectra were excited with laser emitting wavelengths of 532 nm. The X-ray diffraction (XRD) study was conducted using a SmartLab (Rigaku, Tokyo, Japan) high-resolution X-ray diffractometer to check polymer materials' crystallinity and phase structure. Energy-dispersive X-ray spectroscopy (EDX) is used to study the elemental composition of materials.

- **Surface area**

The specific surface area, pore volume, and size of the 3D PPy composite soft gels were measured by a nitrogen porosimeter (Autosorb IQ, Anton Paar) at 110 °C under a nitrogen gas atmosphere. Weighted samples were outgassed in a vacuum at an elevated temperature. The surface area data was collected using the Brunauer–Emmett–Teller (BET) method, while pore size was identified using the Barrett-Joyner-Halenda (BJH) method. Contact angle measurements to evaluate the hydrophobicity or hydrophilicity of the surface were also taken.

- **Thermal characterization**

Thermogravimetric weight loss of the materials was measured using a Thermal Analyzer (STA) 6000 in the temperature range of 30-800 °C at a rate of 10 °C per minute with a fixed airflow rate of 30 ml per minute.

- **Electrical and Electronic Characterization**

The sheet resistance of polypyrrole films was measured by the Four-Point Probe Method. A semiconductor Hall Effect Measurement was carried out to determine carrier concentration, mobility, and type (n-type or p-type). To study the electrochemical properties and capacitive behavior of synthesized materials, cyclic voltammetry (CV) was carried out. The charge transfer resistance and capacitive behavior were measured by electrochemical impedance spectroscopy (EIS). Galvanostatic Charge-Discharge tests were carried out to evaluate materials' specific capacitance, energy density, and power density.

- **Optical Characterization**

UV-visible spectroscopy was used with the Shimadzu UV 2600-i spectrometer to study the material's optical properties. Emission properties and sample quenching were studied by photoluminescence spectroscopy (PL) and a confocal laser scanning microscope (LSM 780) from Zeiss.

CHAPTER 4. FABRICATION OF POLYPYRROLE FILMS

4.1 Results and Discussions

The bicontinuous microemulsion polymerization method has received a lot of interest as a soft template for producing polymeric materials with unique structures and continuously porous structures. The uniqueness of the synthesis technique is in its capacity to create materials with diverse dimensional architectures—0D, 2D, and 3D—simply by increasing the concentration of the oxidant and dopant or adding cross-linkers to the polymer matrix. This structural versatility, from nanoscale thin films to macroscale porous gels, allows for the fabrication of materials with tailored properties to suit specific application needs. The polymerization of conducting monomers in the presence of surfactant leads to the formation of microemulsions, where surfactant molecules arrange themselves into a continuous phase with a co-continuous interpenetrating void phase. Upon polymerization, monomer molecules distributed within these continuous phases give rise to solid networks that mirror the emulsion morphology and use it as a template for building a porous nature.[103] These thin-layered surfactant interfaces in the BME reactors are the leading platforms for controlling the morphology-property parameters of CPs. Figure 4.1 illustrates the interfaces with different surfactants and how polymer molecules are attached to the surfactant molecules and grow based on the charge of the surfactant.

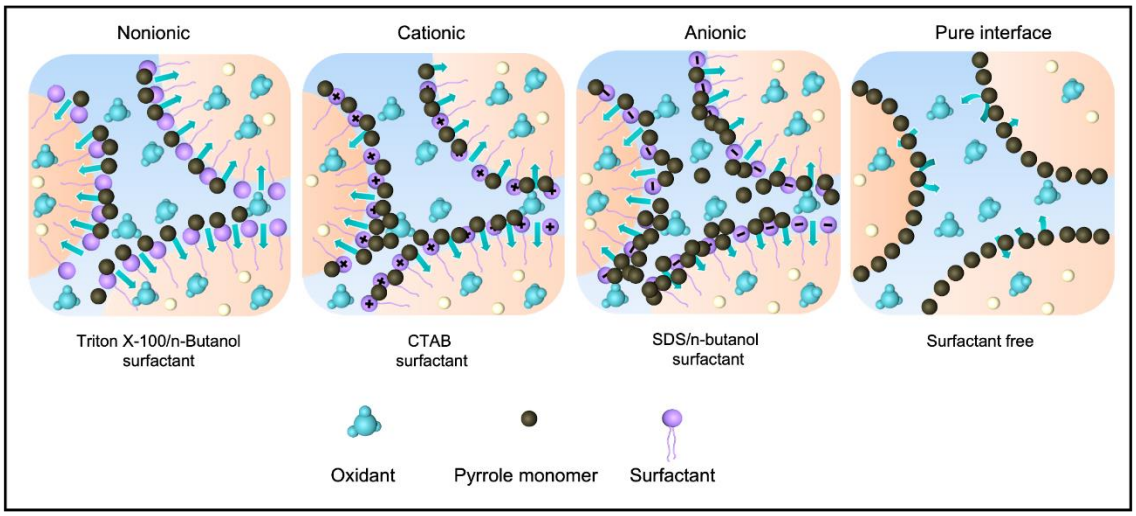

Figure 4.1. Schematic illustration of the continuous structure of interfaces and monomer templating behavior according to the surfactant.

During the polymerization process, we observed various morphological structures of polypyrrole, influenced by multiple factors. The role and concentration of each component in the reactor were

found to be particularly significant in the fabrication of 2D films.[8] Since microemulsion polymerization is a hardly controllable polymerization process, changes in the chemical composition of the BME solution can lead to substantial deviations from the expected morphology and properties of the synthesized material. SEM images of the morphological changes of the polypyrrole are demonstrated in Figure 4.2.

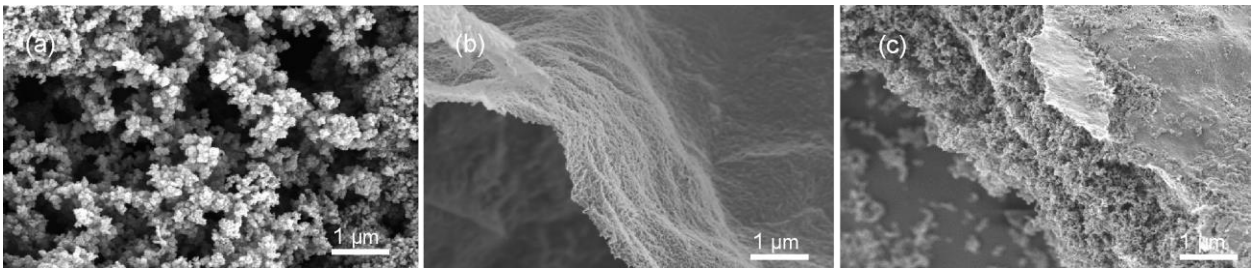

Figure 4.2. SEM images of the different reactor morphologies of polypyrrole obtained by the BME polymerization method (a) particles, (b) 2D film, and (c) 3D porous bulk.

The critical parameters affecting the morphology of the obtained conducting polymers are:

- interface thickness and surfactant charge;
- monomer (oil) phase content and oxidant (water) content ratio;
- oxidant concentration and solution pH, type of doping agent;
- linker concentration in the formation of layered films;

A descriptive analysis of the influence of these factors will be provided later.

4.1.1 Role of surfactant charge in microemulsion polymerization.

Surfactants stabilize the microemulsion system by reducing the interfacial tension between the aqueous and oil phases, leading to the formation of microdroplets or bicontinuous structures. These structures are characterized as nanoreactors where polymerization takes place, influencing the polymer growth, size, and chain distribution. Each type of surfactant impacts the reaction and resulting polymer characteristics. Here is an overview of the conclusions collected during the experimental work discussing the effect of the surfactant on polymer morphology.

Types of surfactants and their characteristics:

- *Nonionic Surfactant Interface*

This type of surfactant stabilizes microemulsion through steric rather than ionic mechanisms because it is less sensitive to pH changes and the aqueous solution's ionic strength. Nonionic surfactant Triton X-100 with co-surfactant n-butanol influenced the morphology of polypyrrole by

facilitating more uniform and smaller micelles, leading to the formation of polymers with more consistent morphologies. The lack of ionic charge means that the surfactant does not participate in electrostatic interactions with the monomer or growing polymer chain, which results in more constrained polymer growth and a smooth surface texture with 25-150 nm scale thickness. The morphology of 2D polypyrrole synthesized by nonionic bicontinuous microemulsion is shown in Figure 4.3. The obtained polymers proved the effect of nonionic surfactant molecules on the structure of polypyrrole.

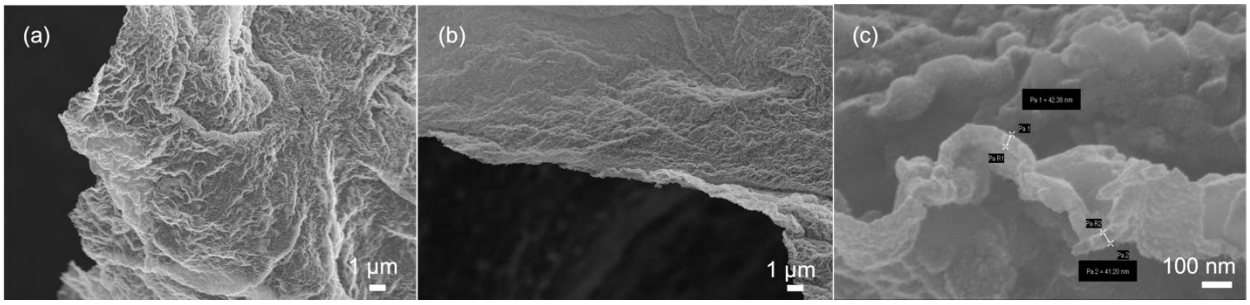

Figure 4.3. SEM images of PPy films synthesized by the nonionic (cyclohexane/Triton X-100/n-butanol/water) bicontinuous microemulsion polymerization method.

- *Surfactant-free (Pure) Interface*

This interface type is characterized by the absence of the surfactant, resulting in reduced control over the polymerization site and phase boundary. It leads to the more extensive, uncontrolled growth of polymer aggregates. The films of polypyrrole obtained by this interface were dense and thicker, and depending on the type of oxidant and its concentration, the polymer morphology also changed. The average thickness of PPy films obtained by this interface was around 400 nm – 1 µm; Figures 4.4 and 4.5 demonstrate SEM images of films made of surfactant-free interfaces. The effect of oxidants will be discussed later.

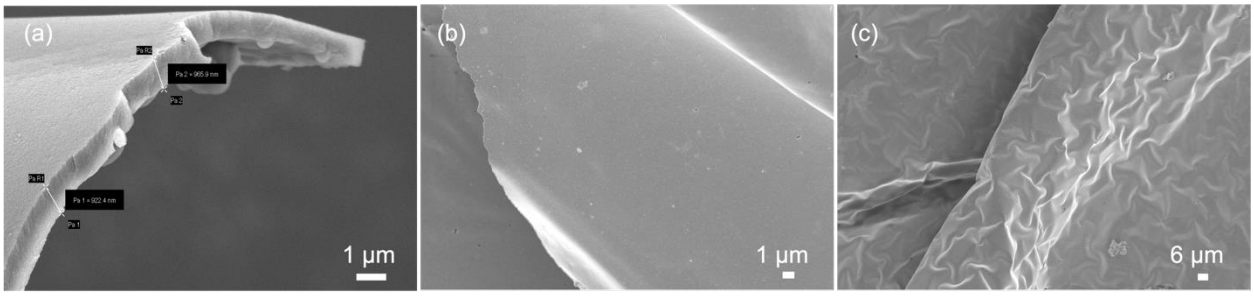

Figure 4.4. SEM images of PPy films synthesized by surfactant-free (benzene/ethanol/water) bicontinuous microemulsion polymerization method.

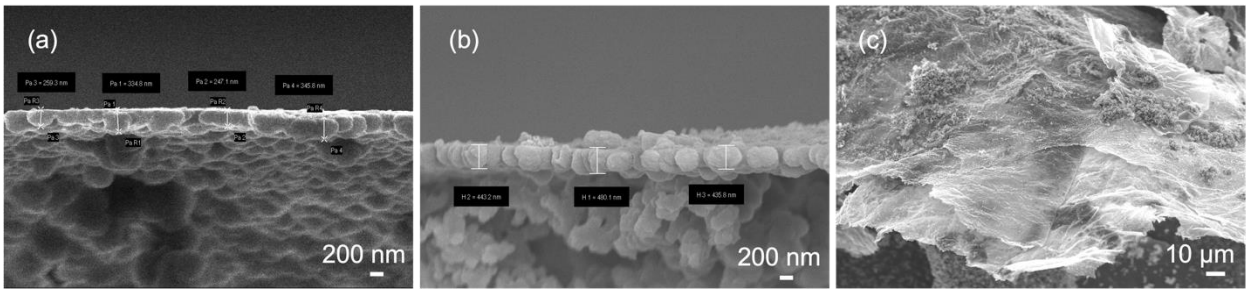

Figure 4.5. SEM images of PPy films synthesized by surfactant-free (DCM/ethanol/water) bicontinuous microemulsion polymerization method.

- *Cationic surfactant Interface*

The cationic surfactant CTAB introduces a positive charge at the micelle interface, significantly affecting the polymerization of inherently anionic or neutral monomers like pyrrole. The positive charge on the surfactant attracts the monomer molecules to the micelle interface, leading to a higher local concentration of monomer at the polymerization matrix. This interaction resulted in a denser, packed, and, in some regions, more branched polymer distribution. The higher attraction also leads to the vertical growth of polymers, which results in the formation of more porous and thick films. The thickness of the obtained polymer thick films was more than 15 μm. (Figure 4.6)

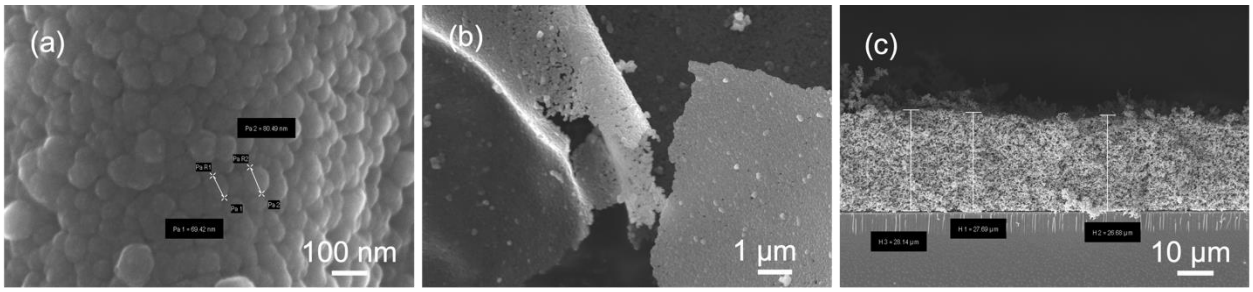

Figure 4.6. SEM images of 2D PPy synthesized by the cationic surfactant (CTAB/n-butanol/cyclohexane/water) bicontinuous microemulsion polymerization method.

- *Anionic surfactant Interface*

The negative charge of anionic surfactant, as SDS repeals anionic monomers, affects the polymerization kinetics as well as the structure of the polymer. The presence of an anionic surfactant resulted in the formation of more porous and softer structures due to weaker interactions with the polymer chain as it grew. The use of anionic surfactant also tailors the pore size and distribution within the polymer matrix. Moreover, the bicontinuous nature of microemulsion

polymerizes monomers with continuous open pores, which can be seen from the SEM image in Figure 4.7 of the polymer structure.

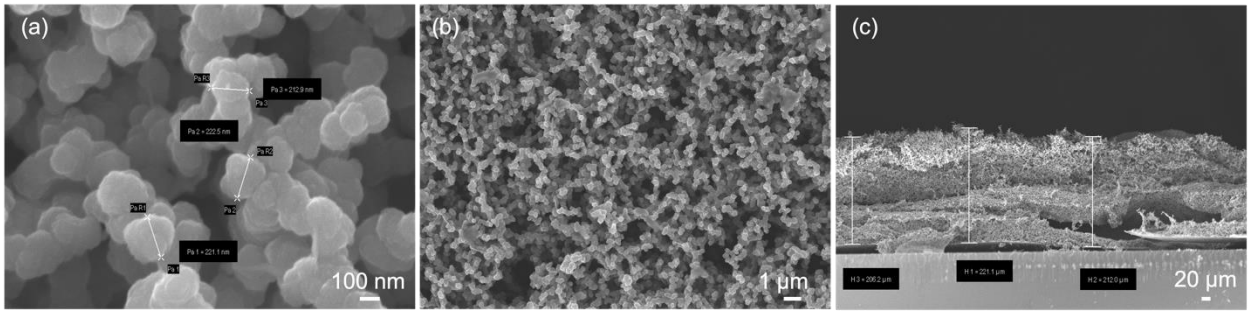

Figure 4.7. SEM images of 2D PPy synthesized by the anionic surfactant (SDS/n-butanol/cyclohexane/water) bicontinuous microemulsion polymerization method.

4.1.2 Surfactant effect on reaction kinetics.

Polymerization of polypyrrole in a bicontinuous microemulsion system involves three key stages: initiation, propagation, and termination.

Nonionic surfactants tend to have a minimal effect on the polymerization rate compared to ionic surfactants. They help to stabilize microemulsion, forming a balanced reaction medium without interfering with monomer reactivity. In this system, $FeCl_3$ acts as an oxidizing agent, generating radicals to initiate polymerization, while p-TSA is a doping agent, enhancing the electrical conductivity of the final polymer.

The oxidative polymerization is as follows:

$$n C_4H_5N + FeCl_3 \rightarrow (C_4H_3N)_n + FeCl_2 + 2HCl$$

In the microemulsion system:

$$n C_4H_5N + FeCl_3 + \text{p-TSA} \rightarrow (C_4H_3N)_n \text{ doped with p-TSA} + FeCl_2 + 2HCl$$

The reaction initiation begins with $FeCl_3$ by oxidizing pyrrole monomers, forming reactive radicals to initiate chain growth. This process is followed by the propagation step, where monomer units continuously attach to the growing chain. The termination occurs when the radical recombination takes place, completing the polymer chain growth.

Oxidant concentration, doping level, and monomer concentration all influence the polymerization rate.[2] Lower concentrations of oxidants and monomers result in a slower polymerization, while

higher concentrations speed up the initiation process, but this may lead to aggregation or structural defects if not controlled. Bicontinuous microemulsions require more time to stabilize.[124] Consequently, all reactors with four interfaces were left for at least 12 hours for stabilization. It is also noteworthy that while polymerization can be completed within a few hours, the resulting films tend to be more brittle, complicating the accurate measurement of electrical properties. Figure 4.8 demonstrates the three stages of polymerization - initiation, propagation, and termination - during PPy film formation. In this process, termination proceeds quickly, with visible film formation within seconds of initiation, confirming the dynamic, interconnected nature of the bicontinuous nature of microemulsions.

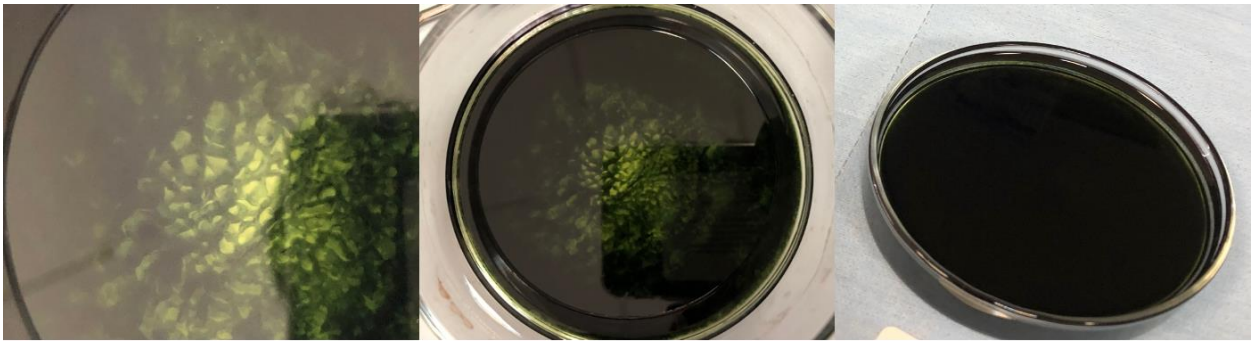

Figure 4.8. The initiation, propagation, and termination phases of the polypyrrole film formation process.

4.1.3 Monomer (Oil) phase content and oxidant (Water) content ratio effect on morphology of synthesized polypyrrole.

Monomer concentration is a critical factor influencing both the rate and degree of polymerization. The thickness of the 2D PPy films is also heavily dependent on the monomer-to-oxidant ratio. Experimentally, it was found that low monomer concentrations, and consequently a reduced oil phase, resulted in very thin 2D films with thicknesses ranging from 25 nm to 150 nm. However, given that this is an interfacial polymerization, the optimal concentration and distribution of each phase and component must be carefully controlled. Figure 4.9 shows three reactors with identical water phase weight percentages but varying oil phase concentrations. In all cases, the concentration of ferric chloride is maintained at 2 mg/ml, with a pH of 1.5.

According to the SEM images, a smaller amount of oil results in incomplete film growth. (Figure 4.9) Specifically, when the oil phase is insufficient, the polymerization process does not proceed

uniformly, leading to gaps and discontinuities in the film. Since the monomer concentration depends on the oil composition, a low concentration cannot complete polymerization. Conversely, excess oil can disrupt the balance between the oil and water phases, producing poor film morphology characterized by surface defects or uncontrollable polymer growth. The mechanism is illustrated in Figure 4.10a,b,c,d.

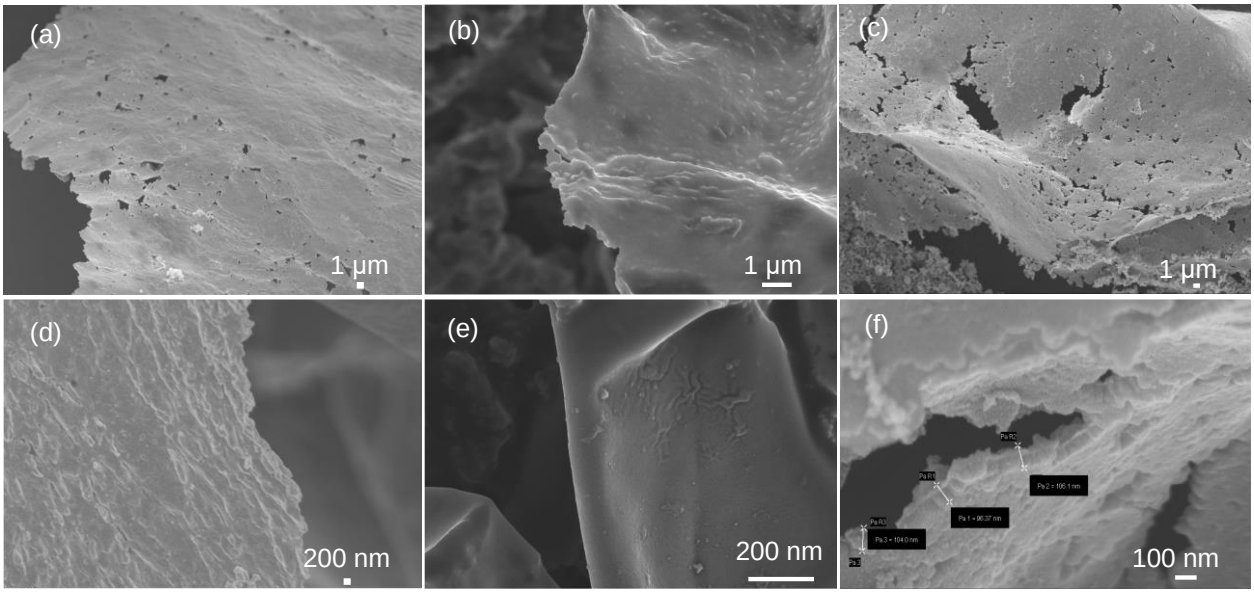

Figure 4.9. SEM images of three reactors with the same oxidant concentration $FeCl_3$ (2 mg/ml) and water phase (5 wt%) at the nonionic surfactant interface (a,d) **Reactor 50/5/45**, (b,e) **Reactor 60/5/35**, and (c,f) **Reactor 80/5/15**.

The reduced aqueous phase means that the particles have fewer interactions due to decreased attractive forces, which contributes to the formation of voids and cracks within the film structure. These structural imperfections highlight the necessity of maintaining an optimal balance between the oil and water phases to achieve a uniform and defect-free film. Therefore, determining the optimal ratio of monomer to oxidant is crucial. The appropriate balance of monomer and oxidant concentrations, along with the careful control of the oil and water phases, is essential for the fabrication of high-quality PPy films. Experimentally, we concluded that the most uniform, thin, and conductive films could be fabricated by a nonionic surfactant interface; therefore, the rest of the investigations were conducted using this BME interface. In this regard, the monomer-to-oil ratio is one of the critical parameters for the polymerization of polypyrrole. In this study on the

synthesis of polypyrrole, various oil-to-monomer ratios, including 95:5, 80:20, 65:35, and 50:50, were examined. The volume composition of the reactor 50/20/30 is demonstrated in Table 4.10. It was concluded that the 80:20 weight ratio is optimal for synthesizing uniform single-layer films. Lower oil content in terms of o-to-l:water ratio resulted in the formation of bulkier and branched structures. (Figure 4.11)

Table 4.1. Reactor composition and different oil: monomer ratios.

50/20/30	**(Oil:PY Ratio) 95:5**	**(Oil:PY Ratio) 80:20**	**(Oil:PY Ratio) 65:35**	**(Oil:PY Ratio) 50:50**
Cyclohexane	12.2ml	10.27 ml	8.3 ml	6.42 ml
Pyrrole	0.518 ml	2.07 ml	3.6 ml	5.17 ml
Water (FeCl3)	4 ml	4 ml	4 ml	4 ml
Triton X-100/Butanol	6.5 ml	6.5 ml	6.5 ml	6.5 ml

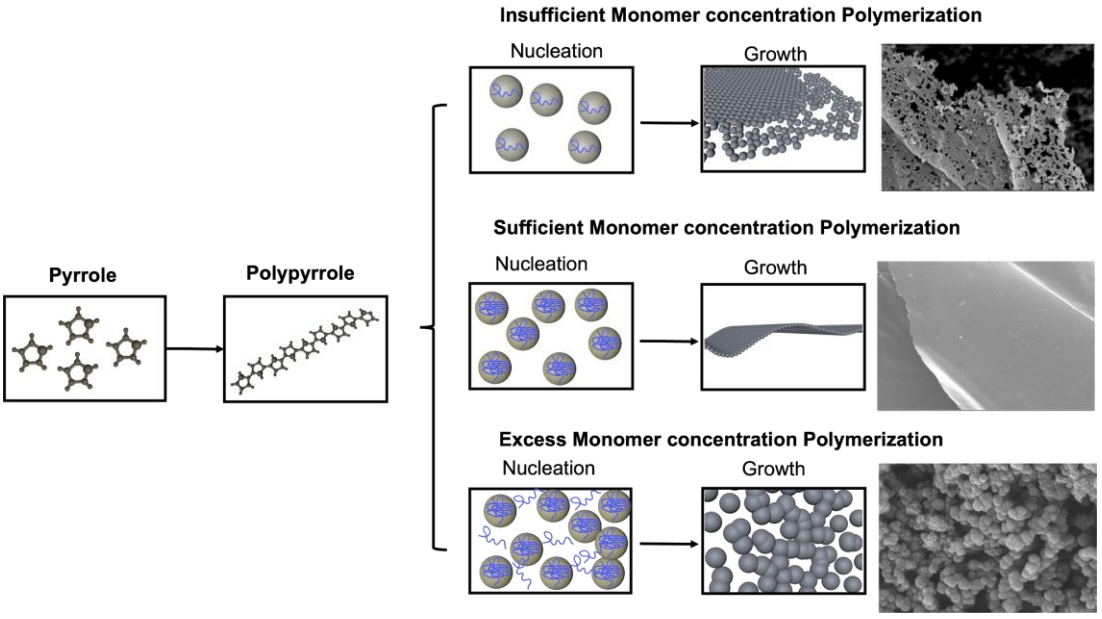

Figure 4.10. Different morphologies were obtained by BME polymerization with different monomer concentrations, including not-complete 2D nanosheet formation, complete 2D nanosheet, and particle networks.

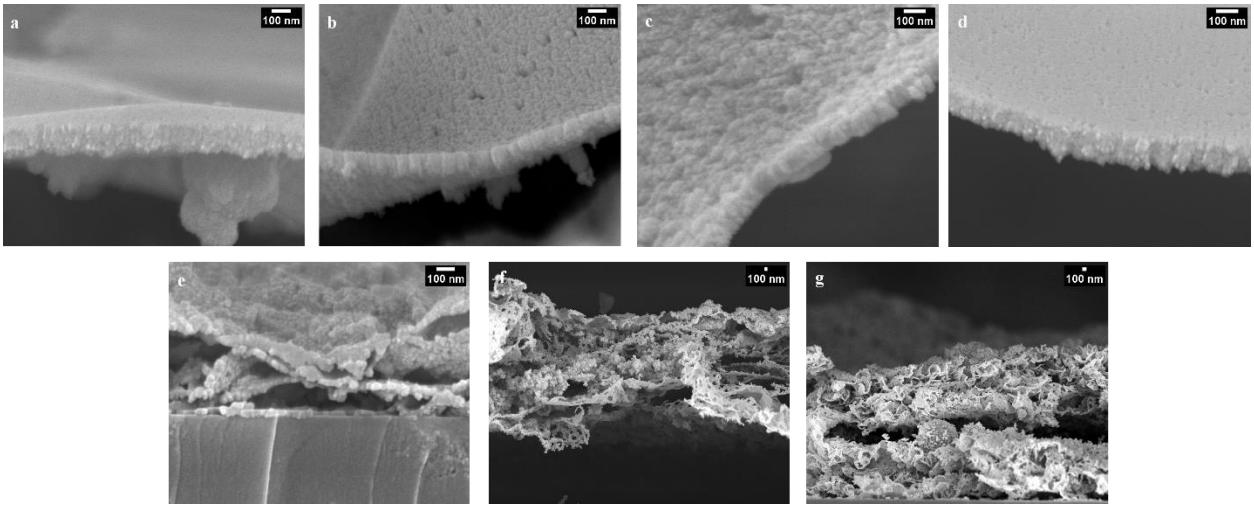

Figure 4.11. SEM images of PPy morphologies obtained by nonionic (Triton X-100/n-butanol) bicontinuous reactor systems with different oil-to-water ratios: a) 80/5; b) 60/10: c) 50/10; d) 50/20; e) 40/30; f) 30/20; g) 30/30.

4.1.4 The oxidant concentration and solution pH, type of doping agent effect on morphology of synthesized polypyrrole.

The water phase content, oxidant concentration, type of doping agent, and solution pH are critical parameters that significantly influence the polymer's final structure and the polymerization rate. Table 4.2 provides a comparative analysis of the effects of oxidant concentration on the morphology of polypyrrole and the impact of water phase distribution on the polymer structure.

Table 4.2. Comparative analysis of the effects of oxidant concentration on the morphology of polypyrrole and the impact of water phase distribution on the polymer structure.

High water phase content	Low water phase content
- Higher water content can create larger micelles and provide more space for the polymer to grow, resulting in more porous and branched structure. - Enhances the hydrophilic interactions that affect the aggregation and distribution of monomer chains.	- Lower water content creates smaller micelles, leading to more confined polymerization. - The limited space in smaller micelles facilitates the formation of dense and compact polymer structures.

High oxidant concentration	Low oxidant concentration

- Faster polymerization with increased rate of initiation and propagation phases. - The rapid consumption of monomer units, combined with limited time for monomer distribution, leads to the formation of numerous polymer nanoparticles. This results in a more porous morphology. - Thicker films.	- Slower polymerization allows more time for monomer diffusion and the gradual growth of polymer chains. - In cases of sufficient water phase in the nanoreactor, slower diffusion of nanoparticles with very small diameters results in uniform crosslinking, leading to uniform films. - Thin films.

The SEM images of PPy films obtained by lower concentrations of oxidant are shown in Figure 4.12. Polypyrrole nanosheets were synthesized through the assembly of PPy nanobeads. At low oxidant concentrations ($FeCl_3$, 5 to 20 wt.% of water), the polymer chains of PPy primarily grow in a bidirectional manner due to the limited number of nucleation sites, which allows the growth process to dominate over nucleation. In contrast, at low monomer ratios, the high abundance of oxidants creates numerous nucleation sites, making nucleation the dominant process relative to growth. (Figure 4.10 e,f,g) Consequently, the formation of PPy nanoparticles is favored at low monomer ratios rather than the formation of 2D nanosheets. Figure 4.13 shows that the variation in oxidant concentration ($FeCl_3$ 0.01 M, 0.36 M, and 0.71 M) within a uniform reactor configuration led to a noticeable increase in the thickness of the material. In this experimental context, the reactor size is held constant to isolate the influence of oxidant concentration on material thickness. This relationship between oxidant concentration and material thickness is critical to the investigation, offering insights into the intricate interplay between reactant chemistry and resulting material properties.

As the oxidant concentration rises, the availability of reactive species amplifies, promoting a higher rate of material deposition. Consequently, more material is deposited onto the substrate within the same time frame, leading to an increased material thickness.

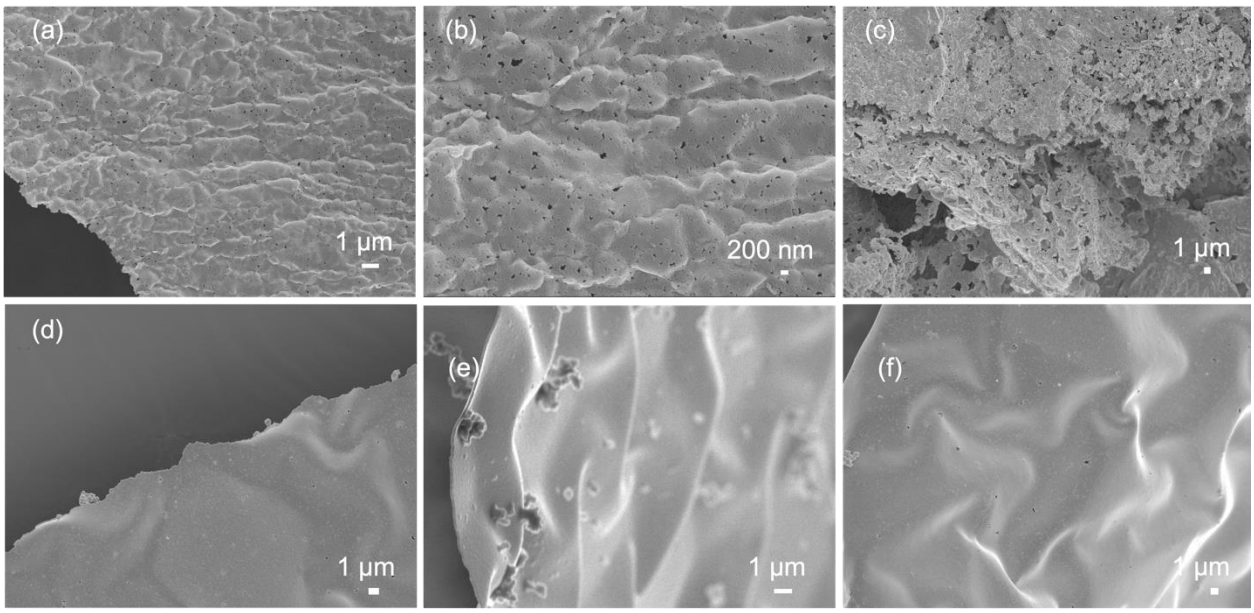

Figure 4.12. SEM images of one reactor 50/20/30 with the oil-to-monomer ratio of 80:20 wt% and different oxidant concentrations: (a,b,c) $FeCl_3$ 2 mg/ml, (d,e,f) $FeCl_3$ 5 mg/ml.

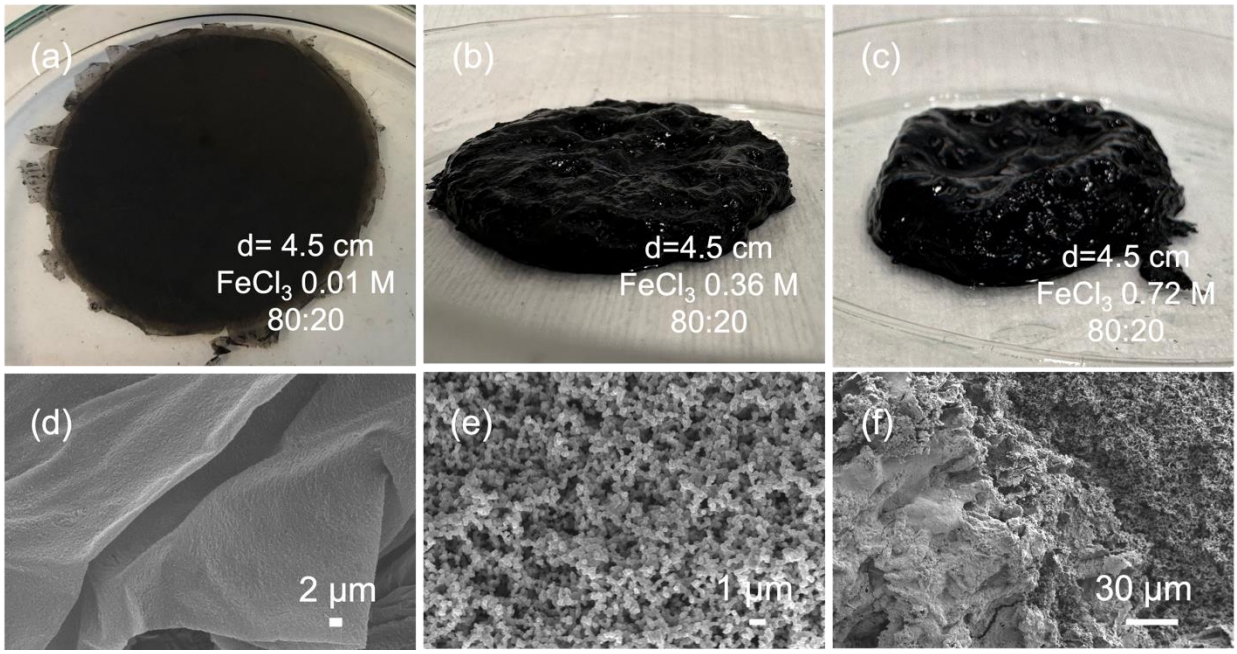

Figure 4.13. Actual photos and SEM images of Polypyrrole morphologies obtained at higher oxidant concentrations, but the same reactor size (d-4.5 cm), and Oil: Py ratio (80:20 wt%): (a,d) $FeCl_3$ at 0.01 M; (b,e) 0.36 M, and (c,f) 0.72 M, within 50/20/30 nanoreactor.

4.1.5 The water and surfactant ratios effect on multi-layered polypyrrole nanosheet formation.

Appropriate manipulation of the interface is critical for constructing mono-layered, double-layered, and even multi-layered 2D freestanding nanosheets, as shown in Figure 4.14. The wavy and wrinkled nature of the bicontinuous microemulsion affects the formation of multi-layered sheets, including wrinkled film surfaces. Adjusting system parameters, such as increasing the water content or manipulating the surfactant content, results in the distribution of monomers across several oil-water phases, facilitating the formation of multi-layered films. However, due to their wrinkled nature, the packing efficiency of these films could be improved.

Figure 4.15 illustrates the effect of water content on the formation of nanosheets synthesized by the nonionic interface, with water content gradually increasing from 10 wt.% to 30 wt.%. When the amount of water and surfactant in the bicontinuous nanoreactor exceeds 30 wt%, many-layered polymer sheets are formed. This occurs as monomer concentrations are relatively reduced, which is a significant factor in forming multi-layered film structures. The water-to-surfactant ratio is a crucial parameter in achieving the layered structure of the film. It was observed that the trend of packed layers increased with the rise in water content in the nanoreactor system.

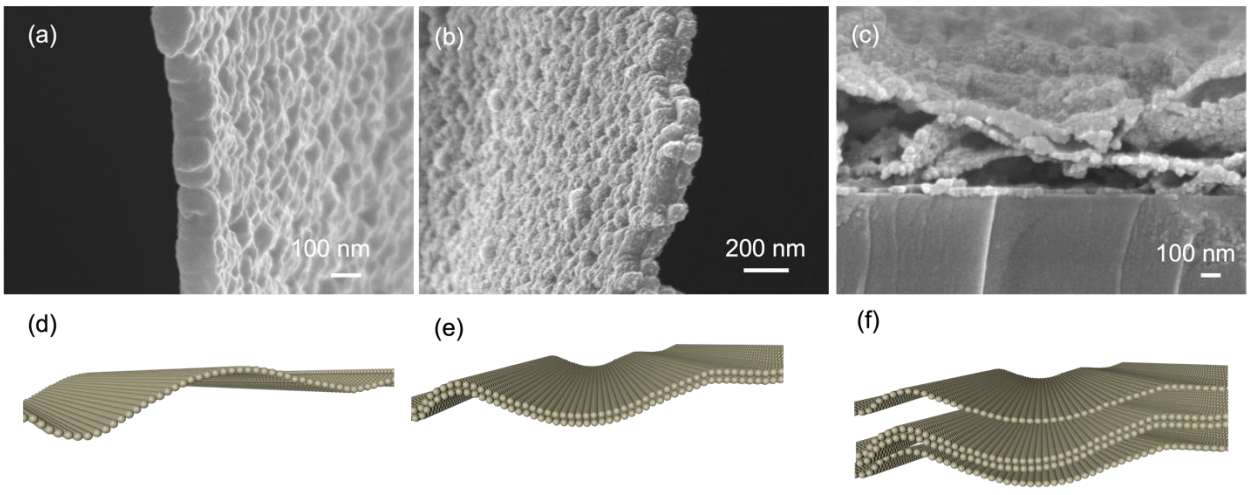

Figure 4.14. SEM images and molecular models of PPy films obtained by nonionic interface nanoreactors: (a,d) mono-layered PPy from reactor 60:10, (b,e) two-layered PPy from reactor 60:15, and (c,f) multi-layered PPy from reactor 40:30.

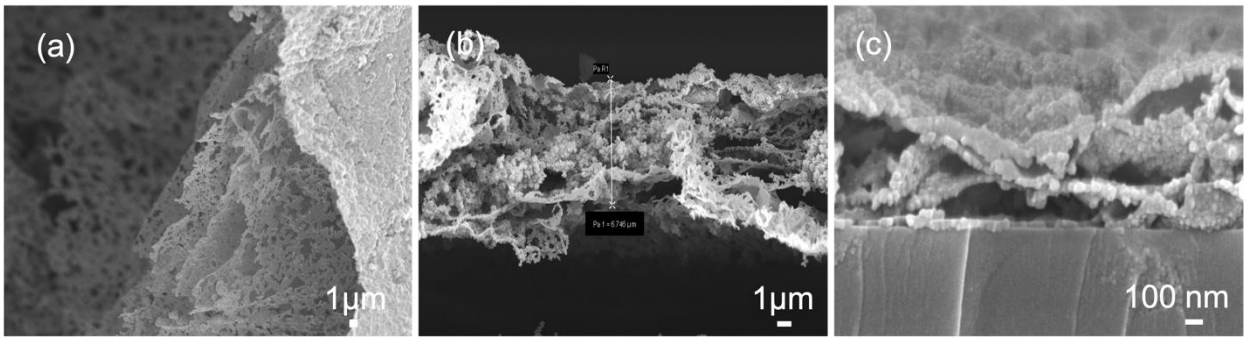

Figure 4.15. SEM images of reactors with a lower monomer concentration and higher water and surfactant contents at the nonionic interface. (a) **Reactor 30/30/40**, (b) **Reactor 30/20/50**, and (c) **Reactor 40/30/40**.

4.2 Scalability assessment of the proposed polypyrrole synthesis approach.

The transmittance, size and thickness of the obtained 2D films demonstrated a positive correlation with the size of the nanoreactor. Using the same weight ratio composition for the reactants and maintaining identical monomer and oxidant concentrations but varying physical sizes of reactors (bottles with diameters of 9 cm and 4.5 cm), resulted in denser and darker films in a smaller reactor.(Figure 4.16a) In contrast, a larger surface area for monomer distribution led to formation of thinner and more transparent films, as illustrated in Figure 4.16b. Additionally, lower monomer and oxidant concentrations also lead to the formation of more transparent films. This approach offers a scalable strategy for fabricating large films simply by adjusting the reactor dimensions and compositions to control the optical and structural properties of film.

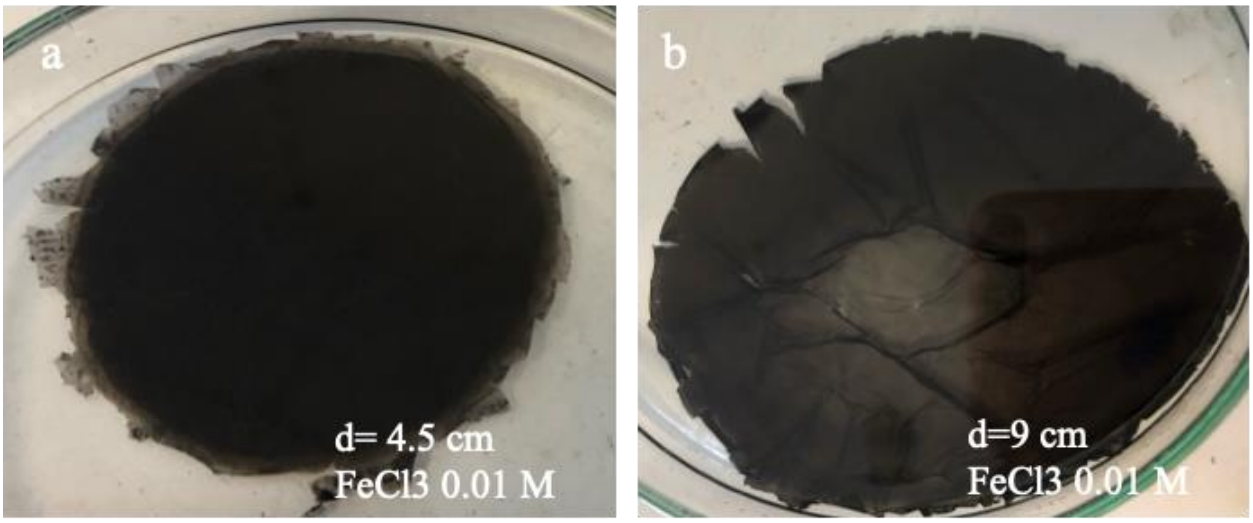

Figure 4.16. The scalability of the proposed approach is demonstrated on the actual photos of 2D PPy films fabricated by 50/20/30 reactor at the same oxidant concentration $FeCl_3$ 0.01 M, but different reactor sizes: a) Reactor 1 with d=4.5 cm, b) Reactor 2 with d= 9 cm.

4.3 Morphology-property studies of polypyrrole films.

Conjugated polymers exhibit increased conductivity with the addition of doping agents. The oxidation reaction removes electrons from the π-conjugated double bond and forms a radical cation in polypyrrole. This leads to crystal lattice deformation and the formation of polarons and bipolarons. Overall, the conductivity mechanism of the polypyrrole can be described by the transportation of bipolarons and anions and the moving of electrons along the polymer chain.

Polymerization of pyrrole monomers takes place in our reactor systems, with the presence of $FeCl_3$ and HCl as doping agents. Depending on variables included in the morphological investigations, polypyrrole nanosheets can range in thickness from 25 nm to 400 nm. The electrical characteristics of PPy films are greatly influenced by these factors, as seen in Table 4.3. This table presents the mean conductivity values derived from four distinct reactors. Our reactors, which have been specifically constructed with four different interfaces, provide precise control over the electrical characteristics of the materials being manufactured. Nanosheets produced using the pure interface reactor system (DCM system) exhibited the highest conductivity, 219 S cm^{-1}, as a result of the absence of an interfacial barrier and the effortless transportation of doping agents into the polymer matrix. The nonionic interface at the ideal oil-to-water ratio (50:20 wt%) achieved a conductivity of 145 S cm^{-1}, which is the second highest. This interface has no impact on the transit of doping molecules.

Furthermore, the electrical properties of 2D conducting polymers are significantly influenced by the ratio of monomer to oxidant, which contributes to their uniformity and relatively low thickness. This range of electrical conductivity is contingent upon the uniformity of the 2D conducting polymers. When cationic and anionic interfaces were used, the synthesized materials had more pores and uneven shapes, which made the space between particles bigger and decreased their ability to carry electricity. 2D PPy nanosheets generated from neutral and pure interfaces exhibit a conductivity that is ten times greater than that of 2D conducting polymers that have been

previously reported. By manipulating the interface and adjusting the doping conditions, it is possible to precisely adjust the electrical characteristics of conducting polymers.

Table 4.3. The average electrical conductivities of 2D PPy film obtained by four different interfaces.

BME System	Oil/Water	Sheet Resistivity (Ohm/sq)	Conductivity (S/cm)
Non-ionic	60:10	776±20.6	**145±4.12**
Surfactant-free (DCM)	47:5	95	**219**
Surfactant-free (Benzene)	1:69	6640	7.69
Anionic	13.3:52	231	0.22
Cationic	12.5:35	2490	0.15

Hall measurements of polypyrrole films have confirmed its p-type semiconducting nature. The analysis revealed a sheet concentration of 1.62×10^{12} cm^{-2} and high carrier mobility of 3.02×10^{4} $cm^2V^{-1}s^{-1}$. These values indicate that the PPy film possesses excellent charge transport properties, which are critical for enhancing the performance of electronic devices. The high mobility suggests efficient movement of holes through the polymer matrix, reducing resistive losses and improving the overall electrical conductivity. This characteristic, combined with the significant sheet carrier concentration, underscores the potential of PPy films in applications such as flexible electronics, sensors, and other advanced electronic devices that require high-performance conducting materials.

The thermogravimetric analysis (TGA) of the 2D polypyrrole films made with nonionic surfactant-based BME and surfactant-free BME demonstrates variations in their thermal stability and the degradation characteristics. (Figure 4.17a) In contrast to common expectations, the surfactant-free PPy film exhibits enhanced thermal stability, as illustrated in the graph, where it retains weight at elevated temperatures prior to substantial disintegration. This indicates that the surfactant-free film possesses a denser structure, likely attributable to more compact molecular packing resulting from the absence of surfactant molecules that would otherwise disturb the polymer network. Both films exhibit two principal weight loss events: the initial occurring at approximately 100–150°C, associated with the evaporation of moisture and volatile chemicals, and the subsequent event between 300–600°C, linked to the degradation of the PPy backbone. The film based on nonionic

surfactants decomposes more swiftly, perhaps due to surfactant-induced porosity, resulting in diminished structural cohesion. The residue detected at elevated temperatures indicates carbonaceous material, implying incomplete decomposition in both instances. The findings highlight that the surfactant-free synthesis method yields denser films with superior thermal stability, rendering them potentially more appropriate for applications necessitating higher thermal performance.

To study the crystallographic characteristics of 2D polypyrrole, XRD analysis was conducted. The XRD spectrum of 2D PPy shows a broad peak centered around $2\theta = 20°$, indicating an amorphous or poorly crystalline structure (Figure 4.17b). The broad peak indicates the semi-crystalline structure with some ordered domains within a polymer-disordered matrix.[21] We see more distinct peaks on the XRD curve of polypyrrole than 2D polypyrrole. The most evident peak appears at around $2\theta = 18°$, supported by an additional peak at a higher angle. This suggests the successful incorporation of linkers into the polymer matrix, resulting in improved structural order with some degree of crystallinity.

The formation of the pure 2D PPy material was confirmed by FTIR spectroscopy (Figures 4.17c). Different samples of nonionic surfactant polymer films were studied. The presence of the minor peaks at bands 3500–3600 cm^{-1} corresponds to N-H stretching vibrations.[4] The 3000-2900 cm^{-1} characteristic peaks are attributed to the =C-H stretching.[3] The peaks observed at 1558 cm^{-1} and 1475 cm^{-1} are assigned to a carbonyl stretching bond. Meanwhile, peaks at 1699 cm^{-1} represent C=N bonds, and 1304 cm^{-1} stand for C-N bonds, respectively. The C-H bond wagging can be detected at 911 cm^{-1} and 783 cm^{-1} peaks.

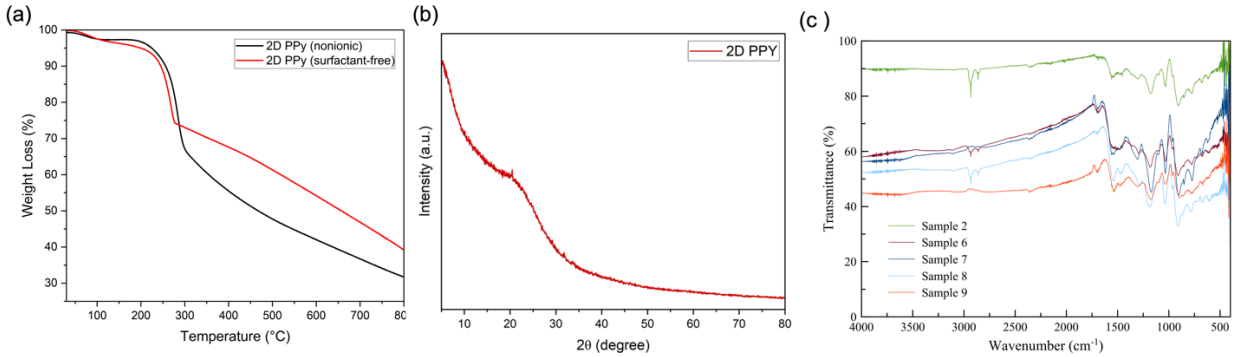

Figure 4.17. A) The TGA graphs of 2D polypyrrole made in nonionic and pure reactors. B) XRD spectra of 2D polypyrrole. C) FTIR spectra of pure 2D PPy film. D) IR spectra of pure 2D PPy films.

CONCLUSIONS

In conclusion, a general, simple, and scalable synthetic strategy has been successfully developed to design and fabricate two-dimensional (2D) and three-dimensional (3D) conducting polymers and their nanocomposites. This innovative approach leverages four distinct bicontinuous interface nanoreactors, including pure, nonionic, cationic, and anionic. Critical parameters such as the nature of the interfaces, the thickness of interface phases, monomer-to-oxidant ratios (including the ratios between monomers, linkers, and oxidants), oil-to-monomer, water-to-surfactant and doping levels were systematically studied and identified as critical factors influencing the morphologies and electrical properties of the conducting polymer materials. Without a molecular layer, the pure interface produced 2D nanosheets with the highest electrical conductivity compared to other interfaces, significantly surpassing literature-reported values for 2D-sheet conducting polymers. Furthermore, 3D polypyrrole materials were successfully synthesized in the bicontinuous reactor system with the inclusion of unique linkers. In the synthesis of the nanocomposites, carbon dots were evenly dispersed phase and added to the mixture of monomers and linkers, enhancing the composite's properties.

This proposed approach shows great potential for the design and scalable production of advanced conducting polymers and their 2D, 3D, and nanocomposites. This method's promising results and flexibility pave the way for future developments and applications of conducting polymers in various advanced technological fields.

CHAPTER 5. FABRICATION OF 3D POLYPYRROLE

5.1 Introduction

Due to the rising demand for effective, high-performance devices, the development of advanced materials for energy storage and sensing applications has received considerable attention in recent years.[6] Conducting polymers, known for their excellent electrical properties and environmental stability, have emerged as promising candidates. Among these, polypyrrole stands out due to its high conductivity, ease of synthesis, and versatile applications. However, conventional synthesis methods often result in materials with limited porosity, which can hinder their performance in practical applications. We present a new way to use the bicontinuous microemulsion polymerization method to make 3D networks of continuously porous polypyrrole. [116] The bicontinuous microemulsion polymerization method makes it possible to create a unique open-cell porous structure that makes the material much better at moving charge carriers which is a crucial parameter for energy storage and sensing applications.[109] The unique interconnected porous network of developed 3D polypyrrole gels allows better electrode-electrolyte interactions with improved ion diffusion which leads to superior electrochemical performance compared to other porous materials.[116]

Bicontinuous microemulsion polymerization methods utilizes the surfactant molecules as a soft template for polymerization of monomers and this template can be easily removed by washing without affecting to the physical and electrochemical properties of the synthesized conducting polymers. While removal of a hard template during traditional templating methods can introduce defects and reduce conductivity.[28,108,125]

The following chapter will provide a deeper understanding of the relationship between morphology and property characteristics of 3D polypyrrole soft gels. The comprehensive analysis of factors influencing the surface area, porosity, physical and electrical properties of the synthesized materials will be discussed in detail.

5.2 Results and Discussions

5.2.1 Self-Crosslinking Synthesis of 3D PPy soft gels.

The synthesis of 3D PPy soft gels was successfully achieved by a one-step, scalable, bicontinuous microemulsion polymerization method. A schematic illustration of the process is shown in Figure 5.1. The bicontinuous microemulsion was formed in a nonionic nanoreactor composed of an intricate balance of water, oil, surfactant, and pyrrole monomer. In this nanoreactor system, monomer molecules were evenly distributed among all layers, which allowed a uniform initiation of the polymerization process after adding the oxidant solution and led to the development of a 3D interconnected network. The formation of the continuously porous morphology is assisted by surfactant molecules, which serve as a template around which the polymerization proceeds.

The uniqueness of the synthesis technique is in its capacity to produce materials with diverse dimensional architectures—0D, 2D, and 3D—simply by increasing the concentration of the oxidant and dopant. This structural versatility, from nanoscale thin films to macroscale porous gels, allows for fabricating materials with tailored properties to suit specific application needs.

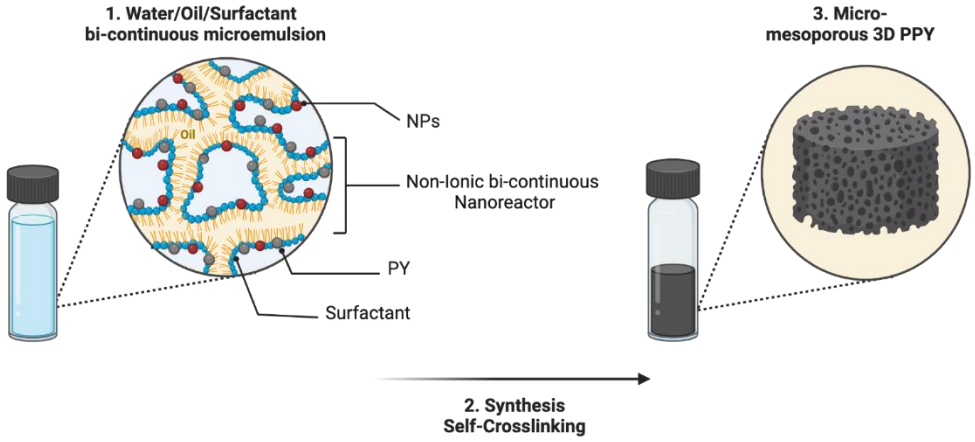

Figure 5.1. Schematic representation of the self-templated 3D PPy soft gel formation.

Figure 5.2 demonstrates the versatility of the polypyrrole structures synthesized by this method. The 2D PPy nanosheets have an average thickness ranging from 25 to 200 nm, whereas the 3D PPy composites are significantly more voluminous, with a thickness extending up to 6 mm. The SEM images of the material in Figures 5.2d, e, and f show the continuously interconnected, pore-

rich structure of the 3D PPy soft gel, which is favorable for applications where fast mass transport and high surface accessibility are required.

5.2.2 Physical Characterization.

TEM techniques investigated the morphology and microstructure of the synthesized 3D PPy soft gels. Figure 5.3A demonstrates a dark, overlayered structure, which indicates the porous morphology of the materials. Fourier transform infrared (FT-IR), Raman spectroscopy, and X-ray diffraction (XRD) analyses have been carried out to confirm the structural features of the materials further.

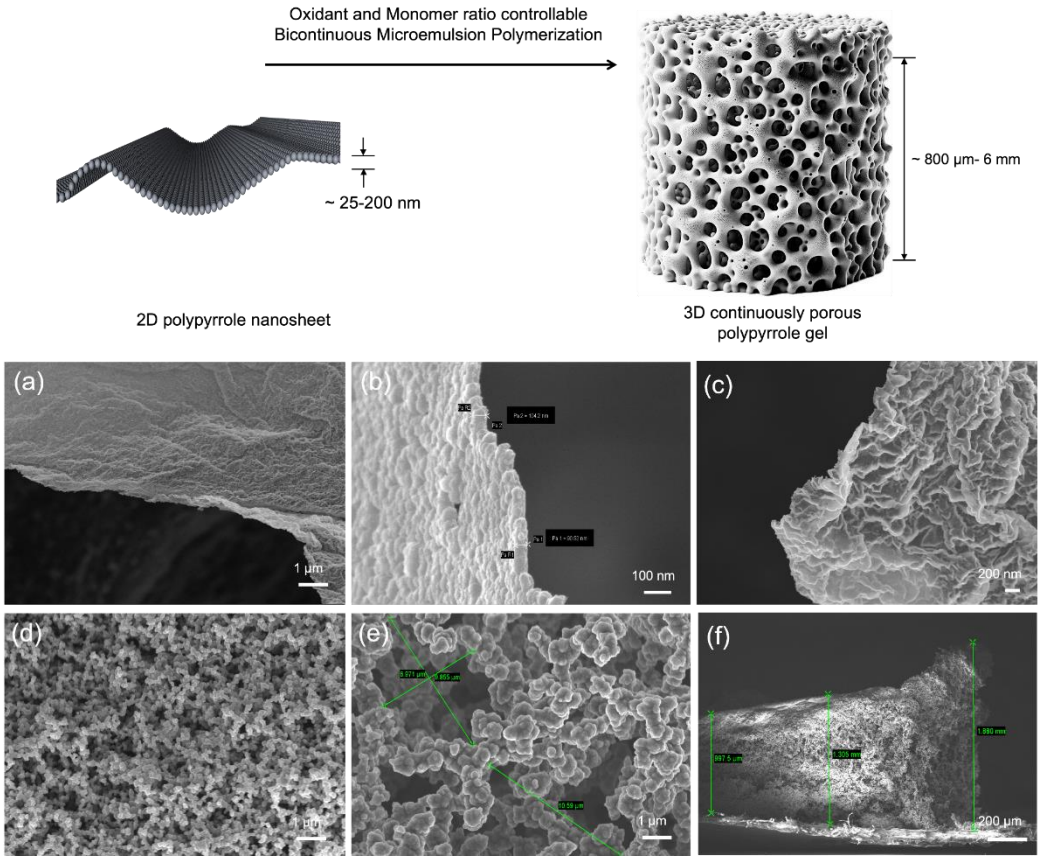

Figure 5.2. Comparative structural analysis of polypyrrole materials synthesized by bicontinuous microemulsion polymerization. (a, b, c) SEM images of 2D polypyrrole nanosheets with a 25 to 200 nm thickness range with different magnification views. (d, e, f) SEM images of 3D polypyrrole soft gels with a macroscopic thickness of approximately 800 µm to 6 mm.

The IR spectra of the pure 3D PPy soft gels are shown in Figure 5.3B. The peaks at 1533 cm^{-1} and 1450 cm^{-1} correspond to the C=C/C-C stretching vibrations in the fundamental polypyrrole ring, which are essential for the electrical conductivity of the PPy[44–46]; the ones at 1278 and 1359 cm^{-1} indicate the C-N stretching vibration[46,113], while the peak at 1030 cm^{-1} reveals the characteristic adsorption peak of the O=S=O stretching, which indicates the p-TSA dopant in the PPy[46]. The 962 and 889 cm^{-1} peaks are associated with out-of-plane C-H and =C-H bending vibrations.[126]

X-ray diffraction (XRD) analysis was used to learn more about the structure of the material that was synthesized (Figure 5.3C). A broad hump at 2θ=20° indicates an amorphous or semi-crystalline nature of polypyrrole[58]. The amorphous nature of polypyrrole is beneficial for applications where flexibility and mechanical stability are essential, such as flexible electronics or sensor devices.

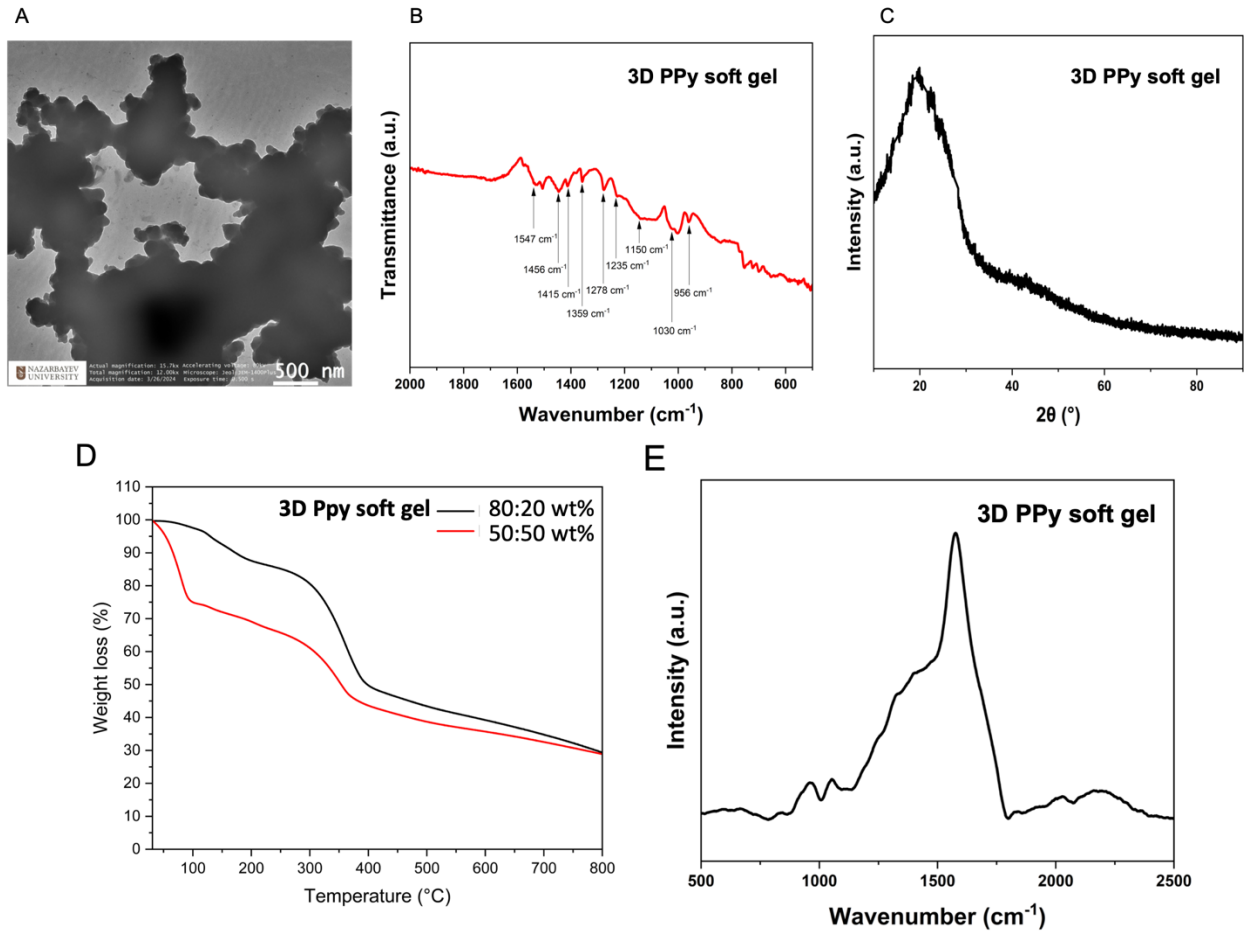

Figure 5.3. A) TEM image of 3D PPy soft gel; B) FTIR curve of pure 3D PPy soft gel; C) XRD spectra of 3D PPy soft gel; D) TGA curves of 3D pure PPy soft gel with 80:20 et% and 50:50 wt%. E) Raman spectra of 3D PPy soft gel.

The thermal and mechanical stability of polypyrrole soft gel were investigated by thermogravimetric analysis (TGA). (Figure 5.3D) The TGA curves of 3D PPy soft gels with 80:20 wt% and 50:50 wt% oil-to-monomer ratios show distinct thermal behaviors. The 80:20 wt% gel shows higher residual mass at elevated temperatures, indicating better thermal stability due to improved network cohesion. The higher oil content may contribute to a more compact and cohesive gel, slowing thermal degradation. The 50:50 wt% gel shows more weight loss over the same temperature range, indicating a less stable structure. This highlights the importance of the oil-to-monomer ratio in tuning the thermal properties of 3D PPy soft gels.

Further characterization of 3D PPy gels was based on the resonance spectra results of Raman Spectroscopy. The min peak (Ag) was detected at 1577 cm^{-1}, which indicated the C=C symmetrical stretching.[127] Peaks at 1379 cm^{-1} and 1315 cm^{-1} related to the inter-ring C-C stretching.[127,128] The stretching vibrations at 1245, 1050 cm^{-1} indicate ring (σ ring) deformation mode.[129] Band at 985 cm^{-1} is associated with the deformation of dipolaron and polaron. [127,128] (Figure 5.3E)

5.3. Structure-Property studies of pure 3D PPy soft gels.

A comprehensive investigation was conducted to investigate the primary factors influencing the structural, morphological, and electrical properties of synthesized 3D PPy gels. The study examined the factorial dependence of the synthesized polymer material on various synthesis conditions, including reaction time, reactor diameter, component temperature, monomer concentration, and concentrations of $FeCl_3$ and p-TSA.

Experimental Factors and Conditions:

Reaction Time: 2 hours, 5 hours, and 24 hours.

Reactor Diameter: 25 mm and 45 mm.

Temperature of Components: room temperature (RT) and 0°C.

Monomer Concentration: oil: pyrrole (PY) ratios: 0.039 M (oil: PY ratio 95:5); 0.162 M (oil: PY ratio 80:20), 0.302 M (oil: PY ratio 65:35), and 0.4M (oil: PY ratio 50:50)

Concentration of $FeCl_3$ (p-TSA): concentration of $FeCl_3$ and (p-TSA): 0.0123 M, 0.031 M, 0.09 M, 0.15 M, and 0.36 M.

5.3.1 Results and Discussions

Based on previously synthesized polypyrrole using a nonionic surfactant bicontinuous microemulsion interface, it was determined that the optimal reactor composition within the nonionic system is a ratio of 50:20:30 (oil: water). Consequently, all subsequent experiments were conducted using this established reactor configuration. Variations in these experiments included modifications in oxidant concentration, adjustments in the doping agent, and changes in monomer concentration.

For 3D studies, different monomer concentrations, points on bicontinuous regions, and reactor compositions were observed. (Figure 5.4A) According to the results, the best electrical and morphological performance of 3D PPy gels was also achieved with the 50:20:30 ratio, validating the critical importance of the optimal ratio in the microemulsion system. In the initial phases of our research, we synthesized 2D PPy films using low concentrations of $FeCl_3$, ranging from 0.01 M to 0.1 M. From these tests; we observed that the highest electrical conductivity achieved was 219 S cm^{-1}. In our current study, we have extended the range of $FeCl_3$ concentrations from 0.01 M to 0.72 M to understand better how different oxidant concentrations influence the resulting electrical conductivity. Figure 5.4 B shows different stages of polymerization of 3D soft gel. In contrast, Figure 5.4C demonstrates obtained soft gels in their wet and dry states.

Table 5.1. Reactor composition and different oil: monomer ratios.

50/20/30	**(Oil:PY Ratio) 95:5**	**(Oil:PY Ratio) 80:20**	**(Oil:PY Ratio) 65:35**	**(Oil:PY Ratio) 50:50**
Cyclohexane	12.2ml	10.27 ml	8.3 ml	6.4 ml
Pyrrole	0.518 ml	2.07 ml	3.6 ml	5.2 ml
Water (FeCl3)	4 ml	4 ml	4 ml	4 ml
Triton X-100/Butanol	6.5 ml	6.5 ml	6.5 ml	6.5 ml

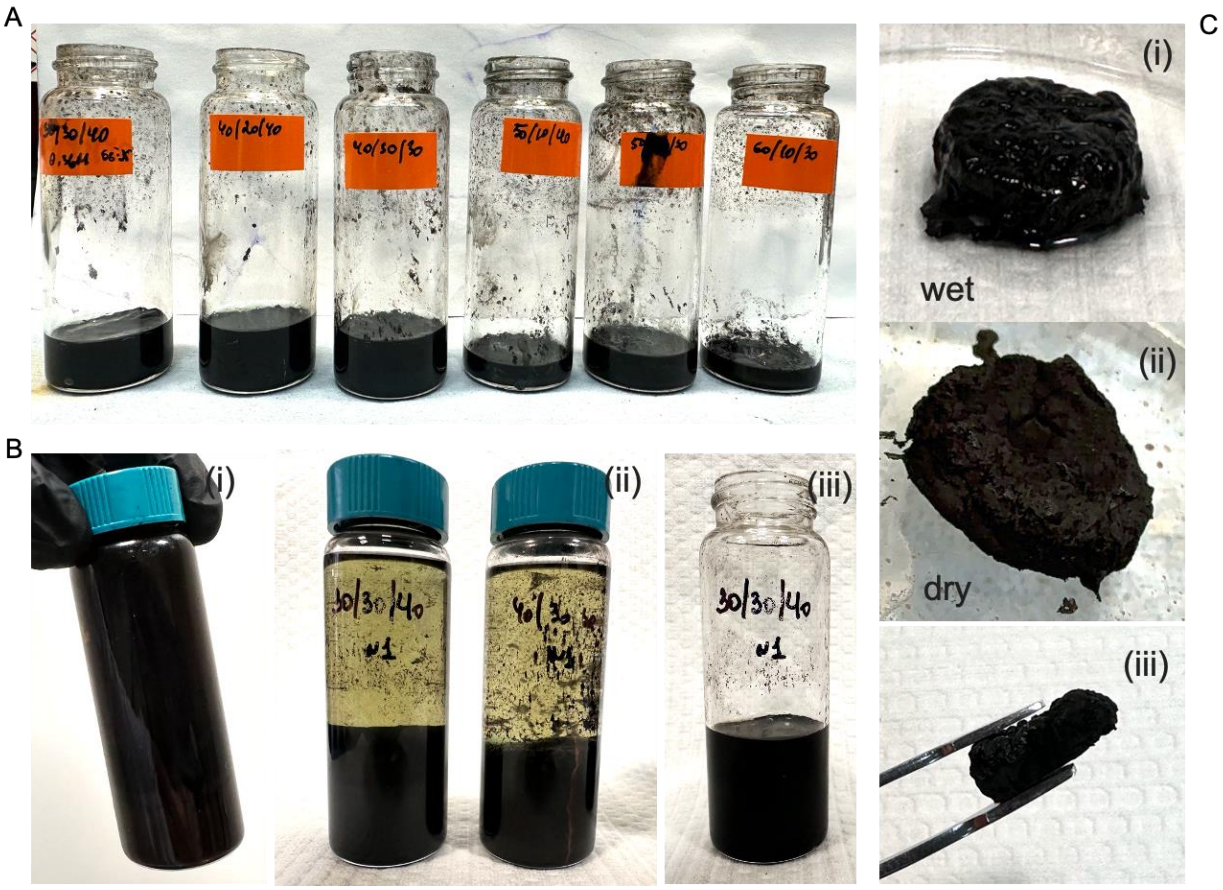

Figure 5.4. A) Polypyrrole gels synthesized by different reactor compositions. (30:30; 40:20; 40:30; 50:10; 50:20; 60:10); B) Stages of 3D PPy gels synthesis: (i) initiation of polymerization right after mixing of microemulsion; (ii) stabilization of microemulsion and gel formation; (iii) removal of oil and surfactant residues before washing. C) (i) Cleaned wet gel; (ii) dry gel; (iii) side view of dry gel.

5.3.1.1 The thickness of 3D Polypyrrole gels.

Several factors, including monomer concentration, oxidant concentration, reactor size, reaction time, and the oil-to-water ratio, strongly influence the thickness of the obtained polymers. The resulting polypyrrole gels exhibited thicknesses ranging from 2 to 10 mm.

- *Monomer Effect*

The monomer concentration is crucial in forming the 3D conducting polymer network within the bicontinuous microemulsion. As depicted in Figure 5.4A, various points in the bicontinuous microemulsion region of the phase diagram (30:30; 40:20; 40:30; 50:10; 50:20; 60:10) were investigated with gradual increases in the monomer ratio in the oil phase, starting from 5 wt%, 20

wt%, 35 wt%, and 50 wt%. In this scenario, only one oxidant concentration (0.36M) was presented, keeping the oxidant concentration constant while varying the reactor composition and maintaining the oil-to-monomer ratio at 80:20 wt%. Similar to the results observed in the synthesis of 2D PPy, the weight percentage of pyrrole monomer in the oil phase significantly influenced the thickness and morphology of the polymer. The same reactor composition and oxidant concentration but varying monomer weight percentages provide polymers with increased thickness, The films obtained were thick but not mechanically stable at lower monomer concentrations due to insufficient intermolecular forces. However, with a gradual increase in monomer concentration, the morphology improved, resulting in a continuously porous structure at 50 wt%. The polymer structure exhibited a layered film and spongy nature at lower monomer and oxidant concentrations. Theoretical principles support these observations. The increase in monomer concentration enhances the availability of polymerizable units, promoting more extensive crosslinking and network formation, leading to a more interconnected porous structure. Also, higher monomer concentrations facilitate better packing of the polymer chains and improve mechanical stability. Conversely, insufficient monomer concentrations result in less stable, layered, and spongy polymer structures.

- *Oxidant Effect*

Experimentally, we concluded that material thickness increases with an increase in oxidant concentration. The reason for this can be the effect of mass transport when a higher oxidant concentration increases precursor molecule flow to the substrate surface. Higher oxidant concentrations promote faster polymerization and particle growth.

In interfacial polymerization, oxidant concentration influences polymer thickness, making films thicker and more uniform. This is a result of the increased availability of oxidizing agents, which facilitate the rapid formation of polymer chains, thereby increasing the physical thickness of the material. Slower polymerization and less monomer availability result in thinner films at lower oxidant concentrations.

Furthermore, the morphology of polymer chains can be substantially impacted by p-TSA as a doping agent. The introduction of sulfonate groups into the polymer network by p-TSA during polymerization can have an impact on the growth and arrangement of polymer chains. The templating effect results in more organized and linked pore structures within the PPy network. P-TSA interacts with surfactants at the oil-water interface to stabilize microemulsion and distribute

monomers and oxidants evenly. Higher crosslinking densities provide stronger, linked pore structures, improving polymer mechanical stability and porosity. Doped polymers have more regular and linked pores than undoped PPy, according to studies.

5.3.1.2 Morphology of 3D PPy gels.

The structure of continuously porous polypyrrole produced using the bicontinuous microemulsion polymerization technique is affected by several aspects, including the concentration of the monomer, the concentration of the oxidant, the type of surfactant, and its concentration. The concentration of monomers directly impacts the availability of pyrrole units for polymerization thus, higher concentrations of monomer promote the generation of a more extensive network and crosslinking. Higher oxidant concentrations facilitate the process by offering a greater number of oxidative sites for pyrrole monomers, leading to an accelerated synthesis of polymer chains in a strong and consistently porous structure with enhanced mechanical stability and electrical conductivity. Surfactants play a vital role in stabilizing the bicontinuous microemulsion by decreasing the interfacial tension between the oil and water phases and regulating the size and distribution of pores. Nonionic surfactants promote the formation of microemulsions that are more stable, resulting in the creation of homogeneous and interconnected pores.

The formation of a continuously porous structure in polypyrrole synthesized via the bicontinuous microemulsion polymerization method can be explained through several mechanisms. (Figure 5.5) These include the bicontinuous microemulsion template, polymerization at the interface, the role of monomer and oxidant, and the formation and growth of pores. The polymerization rate influences pores' size and connectivity, with faster rates leading to smaller and more uniformly distributed pores. Generally, open-cell porous materials exhibit high surface area, and the interconnected pore structure allows for efficient fluid flow and mass transfer, making these materials ideal for use in heat exchangers, respiratory filters, and as scaffolds for tissue engineering. The open-cell structure also offers enhanced mechanical characteristics, including flexibility and better absorption. The unique composition of open-cell porous materials provides a mixture of exceptional functionality and effectiveness, making them adaptable and desirable in a wide range of industrial and biological applications.

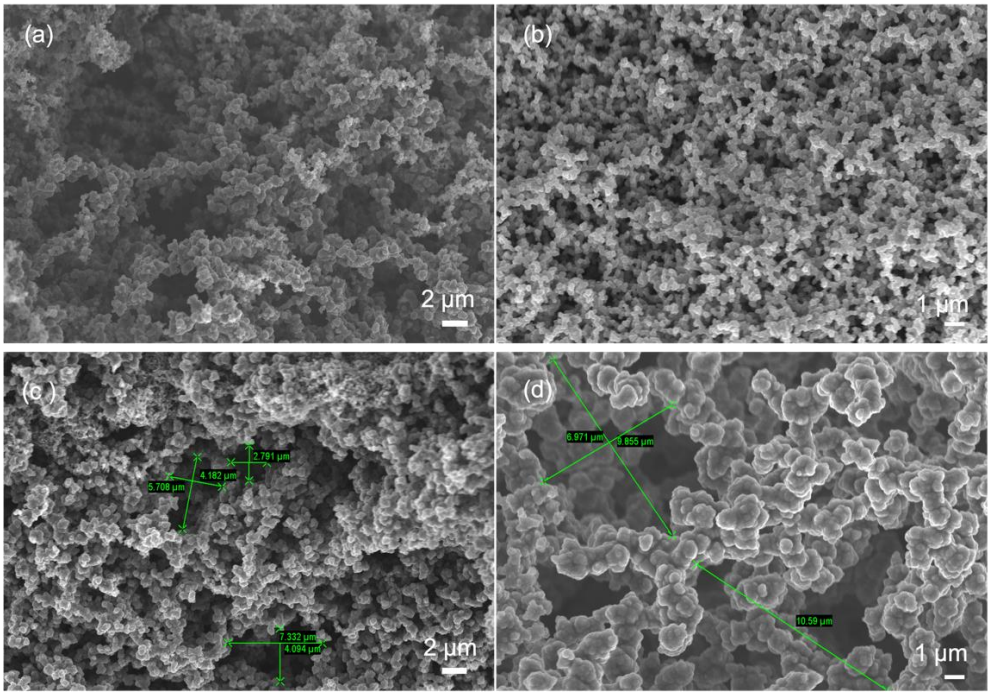

Figure 5.5 SEM images of 3D polypyrrole gels illustrating continuously porous structure.

Figure 5.6 shows the open-cell porosity of polypyrrole gels, demonstrating a 3D PPy-TiO_2 composite gel. Since titanium dioxide ($TiO_{2)}$ is a white powder, it evenly distributes across the polymer matrix and colors open voids on the side of the polymer, which are usually not visible due to the black color of polypyrrole.

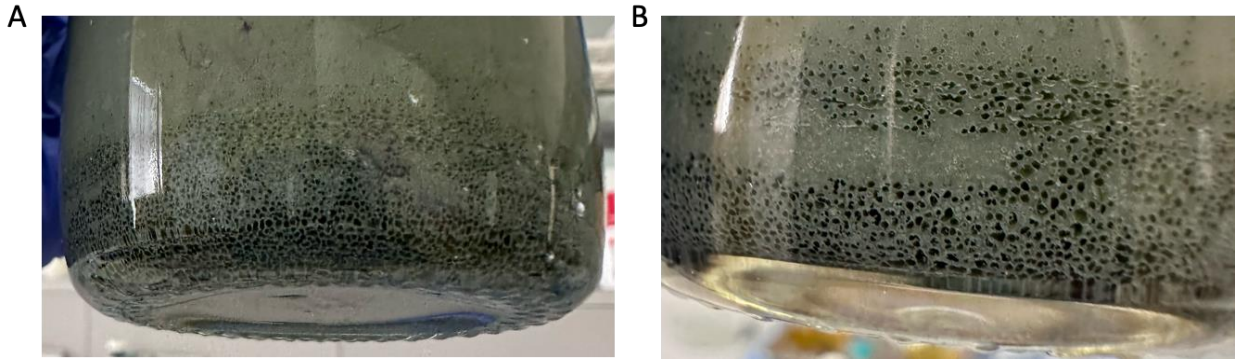

Figure 5.6. A and B are the actual images of the model 3D PPy-TiO_2 composite gel demonstrating the open-cell porosity on the back side of the polymer.

The size of the reactor significantly impacts the electrochemical performance, as well as the physical and mechanical properties, of polymers. As shown in Figure 5.7, maintaining the same oxidant concentration of 0.36 M $FeCl_3$, dopant concentration of 0.36 M p-TSA, and an oil-to-monomer ratio of 50:50 wt%, but varying the reactor diameters (25 mm and 45 mm), leads to a

significant decrease in the polymer thickness. This reduction in thickness has a direct impact on the material's overall electrical conductivity.

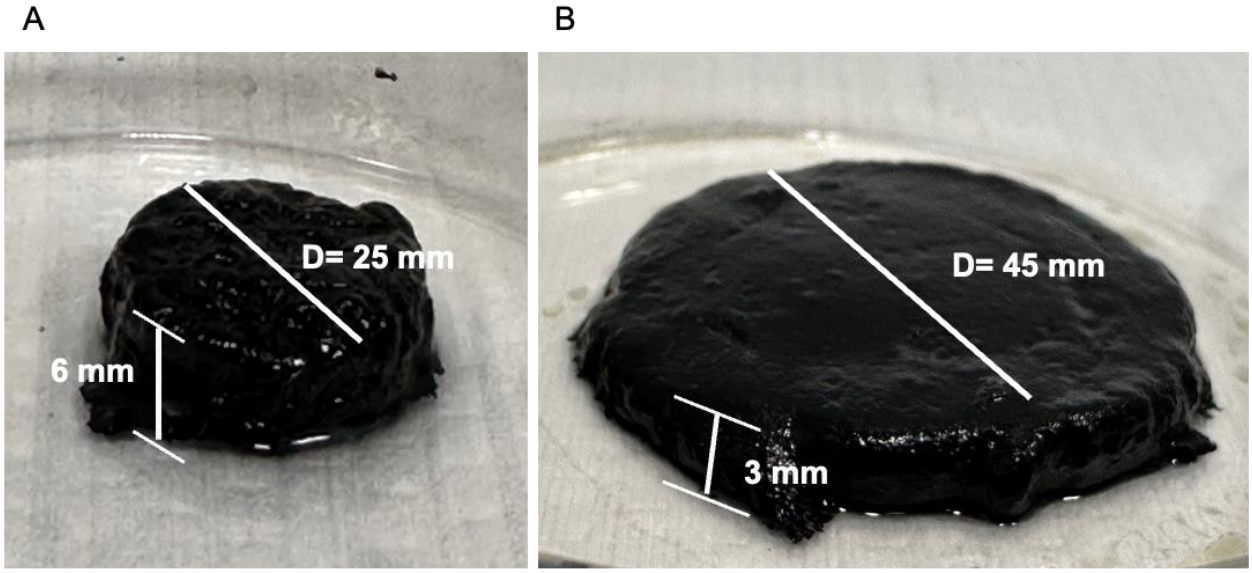

Figure 5.7. Impact of reactor diameter on the physical dimensions of polypyrrole gels.

5.3.1.3 Swelling behavior of 3D PPy gels.

The swelling studies were conducted using the dried weights (m_d) of four polypyrrole (PPy) samples with different oil-to-water ratios (30:30, 40:20, 40:30, 50:20), synthesized with an oil-to-monomer ratio of 50:50 wt% and $FeCl_3$=p-TSA=0.36M. Dry samples were placed in vials containing 10 ml of deionized (DI) water at room temperature and left to swell for various time intervals (t = 15, 30, 60, 120, 240 minutes, and 24 hours) until equilibrium was reached.

The wet, swollen samples were blotted with filter paper and weighed (m_s). The swelling ratio was calculated using the following equation:[6,130]

$$Swelling\ Ratio\% = \frac{W_s - W}{W_d} * 100\% \quad (1)$$

Where,

W_s – the weight of the swollen sample

W_d – the weight of the dry sample.

Hydrogels are three-dimensional polymer networks that absorb and retain significant amounts of water or biological fluids.[110] Their swelling capacity and ratio are critical properties that determine their suitability for various applications, such as drug delivery, tissue engineering, and wound care. A 3D polypyrrole soft gel synthesized in a reactor with an oil-to-water ratio of 50:20 exhibited the

best swelling capacity, achieving a high swelling ratio of 704% in water within 2 hours. (Figure 5.8B) This indicates a highly hydrophilic and porous network. The hydrophilic nature of the polymer was confirmed by water contact angle measurements, where the water droplet was immediately absorbed into the material upon contact with the surface. (Figure 5.8A) A well-structured hydrogel with substantial water-absorbing capabilities is characterized by this swelling capacity.

The elevated swelling ratio indicates a very porous structure, allowing substantial absorption of water, which is advantageous for applications necessitating extensive surface areas. The hydrophilicity of the gel is indicated by its capacity to incorporate a substantial quantity of water, which can be attributed to the effective distribution of dopants such as p-TSA and the presence of hydrophilic functional groups. The swelling behavior is determined by the crosslinking density of the polymer network, and the hydrophilicity and porosity of the gel are probably improved by doping it with p-TSA. This makes it well-suited for applications that benefit from significant swelling, such as scaffold materials in tissue engineering, where cell infiltration and nutrient diffusion are critical, sensors and actuators, and tissue engineering.

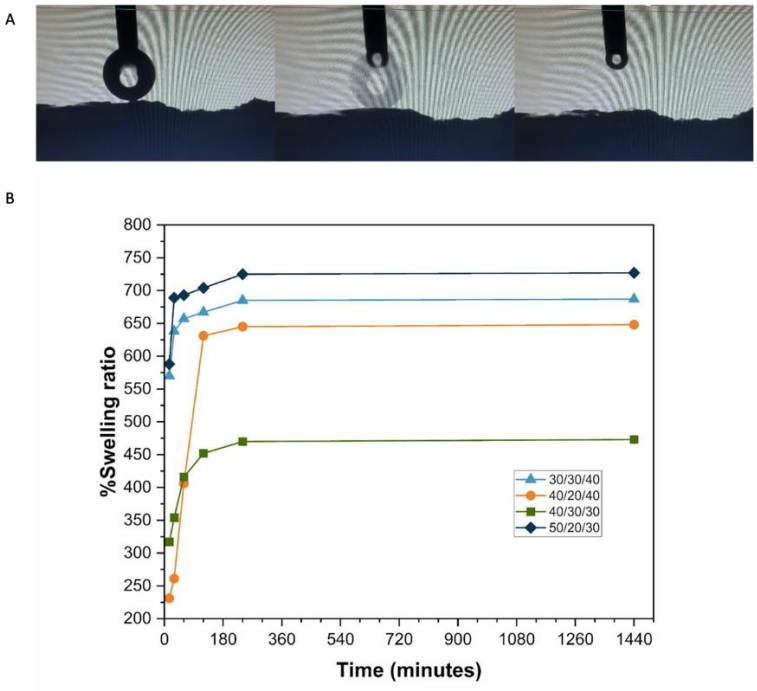

Figure 5.8 A) Super hydrophilic nature of the polymer by water contact angle measurements. B) The graphical representation of swelling kinetics of 3D polypyrrole soft gel.

5.3.1.4 Electrical Conductivity of 3D PPy gels.

Conductivity measurements were conducted using the two-probe method. Five rectangular pieces of each polymer sample were initially cut to exact dimensions. The electrical conductivity was calculated using the bulk conductivity equation. Below, detailed calculations are presented for one sample (95:5 oil weight ratio).

$$1 \text{ S/m} = 0.01 \text{ S/cm}$$

$$\sigma = \frac{1}{\rho} = \frac{l(m)}{R(\Omega)A(m^2)} \quad (2)$$

Where,

5 σ is the conductivity,
6 L is the length of the material,
7 R is the resistance,
8 A is the cross-sectional area

Given:

- Length L = 4 mm = 0.004 m
- Width W = 4mm = 0.004m,
- Height H = 250.2μm = 250.2×10^{-6} m,
- Average resistance R = 422.2Ω.

First, calculate the cross-sectional area

$A = W\times H = 0.004m\times250.2\times10^{-6}\ m=1.0008\times10^{-6}\ m^2$

Now, use the formula to find the conductivity:

$\sigma= 0.004/422.2\times1.0008\times10^{-6}$

Let us compute this:

$\sigma= 0.004 / 422.2\times1.0008\times10^{-6} = 0.004/4.22356336\times10^{-4} = 9.47$ S/m

The standard deviation (SD) of the resistance data for this sample was $\sigma_R= 4.62\Omega$

To calculate the propagated uncertainty for the conductivity ($\sigma\sigma$), we can use the error propagation formula for division, considering the relationship:

$\sigma= R\cdot A/L$

Given the standard deviation of resistance (σ_R= 4.62Ω), the relative uncertainty in the resistance is:

$$\sigma R/R=4.62/422.2$$

We then propagate this uncertainty to the conductivity. The relative uncertainty in conductivity ($\sigma\sigma/\sigma$) will be the same as the relative uncertainty in resistance ($\sigma R/R$) because the length and area are constants without uncertainty.

$$\sigma\sigma/\sigma = \sigma_R/R$$

So, we calculate the relative uncertainty:

Then, we calculate the absolute uncertainty in conductivity:

$$\sigma\sigma=\sigma\times0.01094$$

Given the previously calculated conductivity ($\sigma\approx9.47$ S/m):

$$\sigma\sigma = 9.47\times0.01094\approx0.1036 \text{ S/m}$$

Therefore, the conductivity with its uncertainty is approximately:

$$\sigma = \mathbf{9.47\pm0.10 \text{ S/m} = 0.097\pm0.10 \text{ S/cm}}$$

Table 5.3. Sheet resistance correlation between oxidant concentration and pyrrole concentration of the synthesized polypyrrole materials.

Oil:PY	**0.01 M**	**0.03 M**	**0.09 M**	**0.15 M**	**0.36 M**
95/5	163269 Ohm/sq	4564 Ohm/sq	764 Ohm/sq	691 Ohm/sq	419 Ohm/sq
80/20	21320 Ohm/sq	609 Ohm/sq	352 Ohm/sq	318 Ohm/sq	140 Ohm/sq
65/35	11840 Ohm/sq	320 Ohm/sq	160 Ohm/sq	41 Ohm/sq	122 Ohm/sq
50/50	5678 Ohm/sq	545 Ohm/sq	236 Ohm/sq	125 Ohm/sq	26 Ohm/sq

Table 5.3 presents the sheet resistivity data, offering insights into the impact of various parameters on the electrical characteristics of the films. The trend shows that monomer concentration decreases film resistivity, improving electrical characteristics. Furthermore, the impact of the oxidizing agent is also apparent, especially when considering a 1:1 weight percent ratio of $FeCl_3$ to p-TSA. This combination results in substantial changes

in resistivity, highlighting the importance of the oxidant in determining the film's conductivity.

The observations indicate that increasing the concentration of both monomers and oxidants leads to an increase in the thickness of the material. The synthesis procedure develops ultrathin 2D films with thicknesses ranging from 25 to 700 nm using lower concentrations. On the other hand, increased concentration leads to a transition to a three-dimensional shape defined by a very uniform and gel-like structure. This significant change emphasizes the responsiveness of the synthesis process to subtle changes in concentration and demonstrates the adjustable qualities of the resulting material properties.

Using p-TSA as a doping agent amplifies the electrical efficiency of the materials. A comparative investigation indicates that p-TSA is more effective than HCL in promoting electron transfer effects, suggesting a significant role in improving the electrical properties of the films.

Table 5.4 and 5.5. Electrical conductivity with standard deviation of 3D polypyrrole gels with different oil-to-monomer ratios and oxidant concentrations 0.15 M and 0.36 M.

Ratio (Oil:PY)	Average Resistance (Ω)	Height (m)	Conductivity Oxidant con. (0.15M) (S/cm)
95:5	422	250.2×10^{-6}	0.097±0.01
80:20	320	729×10^{-6}	0.0483±0.002
65:35	42	887.6×10^{-6}	0.268±0.093
50:50	45	751.9×10^{-6}	0.2959±0.052

Ratio (Oil:PY)	Average Resistance (Ω)	Height (m)	Conductivity Oxidant con. (0.36M) (S/cm)
95:5	696	712.65×10^{-6}	**0.0203**±0.0042
80:20	141	1.394×10^{-3}	**0.057**±0.00664
65:35	40	1.535×10^{-3}	**0.168**±0.030
50:50	25	3.412×10^{-3}	**0.1145**±0.033

A uniform resistivity distribution in a material is contingent upon the proper blending of reactor contents, which minimizes variations in resistivity among various regions. In practice It was

observed that the film's conductivity is negatively affected by its thickness, meaning that bigger films have lower conductivity while thinner films have higher conductivity due to several factors such as film morphology, chain alignment, interfacial effects, dopant distribution. The inclusion of p-TSA significantly impacted the material's electrical properties, resulting in increased conductivity and a shiny appearance that suggests greater conductivity and well-defined paths for electrical conduction.

The resistivity measurements revealed a consistent distribution over the material's surface, indicating effective doping and even integrating the dopant.

In addition, a sample with a ratio of 65:35 and an oxidant concentration of 0.36 M displays a remarkable and visually appealing metallic luster, as seen in Figure 5.9.

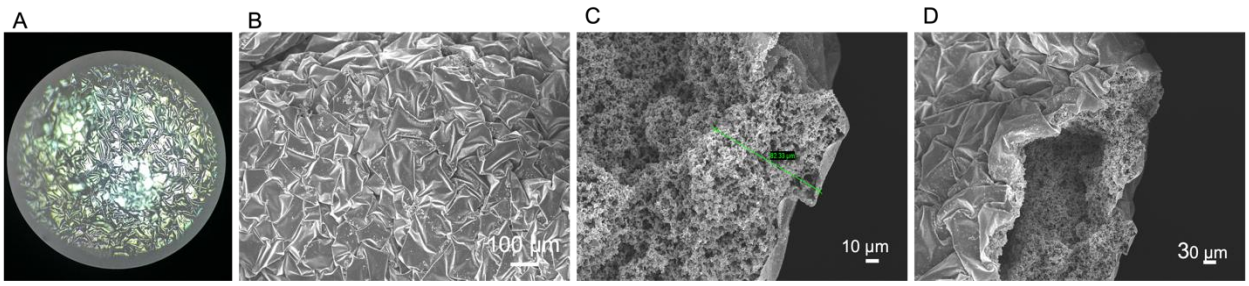

Figure 5.9. A) Metallic luster of PPy soft gel obtained from nonionic reactor with oil-to Py ratio 65:35, captured by optical microscope; B) SEM image of Polypyrrole soft gel with the oil-to-Py ratio 65:35; C) SEM image of the side part of oil-to-monomer ratio in the 50/20/30 reactor with the thickness identified. D) SEM image of PPy obtained from 65:35 ratio.

- **Surface area of PPy gels**

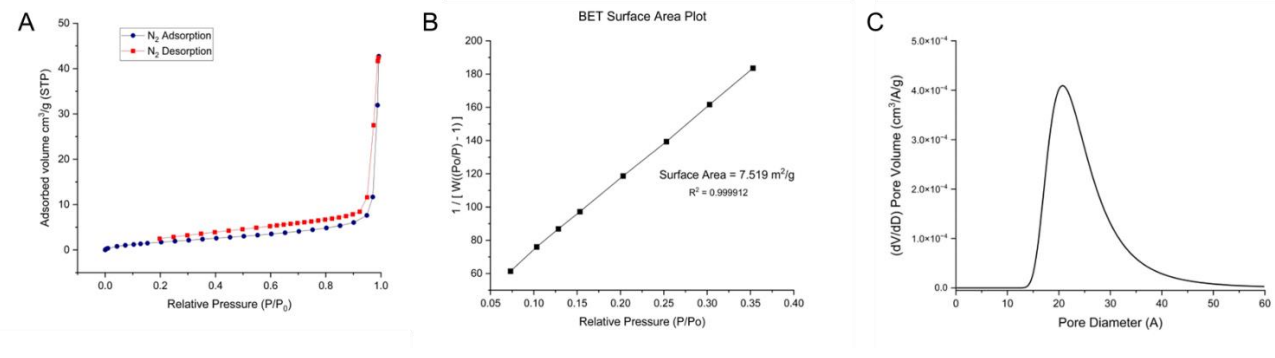

Figure 5.10. A) BET isotherm of Adsorption/Desorption of pure 3D PPy gel indicating Type IV isotherm; B) Brunauer-Emmett-Teller (BET) Surface Area Analysis of 3D PPy; C) Dubinin-Astakhov (DA) method curve showing the pore diameter of the material.

The surface area of the pure polypyrrole gel was found to be 7.519 m^2/g. (Figure 5.10A,B) This moderate surface area aligns with the nature of microemulsion-formed materials, which are expected to be micro- and mesoporous. The pore volume was also measured at 0.064 cm^3/g, and the pore radius Dv(r) was 16.968 Å. These characteristics place the polypyrrole gel within moderate surface area materials, typically ranging from 1 m^2/g to 100 m^2/g, typical for many polymers and certain metals. The pore volume of 0.064 cm^3/g suggests a significant fluid or gas storage capacity within the material, enhancing its potential use in filtration and energy storage devices. The pore radius of 16.968 Å places the material in the mesoporous category, with pores ranging between 2.0 Å and 50 Å, similar to materials like mesoporous silica and ordered mesoporous carbon known for their high surface areas and structural stability. (Figure 5.10C) The synthesis of 3D polypyrrole soft gel using BME polymerization methods results in a well-balanced continuously porous structure with a mix of features that make it suitable for multifunctional applications. The mesoporous nature of the material enables effective mass transport, while its moderate surface area guarantees an adequate number of active sites for chemical interactions. This polypyrrole gel is a promising candidate for applications involving material robustness and surface activity due to the equilibrium between its pore structure and surface area. This adaptability underscores the significance of microemulsion-based synthesis in developing advanced functional materials.

5.3.1.5 Temperature of solvents effect on 3D PPy gels.

It was concluded that low temperatures slow the polymerization process, while synthesis at room temperature with high oxidant concentration leads to rapid polymerization. For lower concentrations of oxidant and monomer, it is better to conduct experiments at room temperature. In contrast, for high concentrations of oxidants and composite materials, it is advisable to use pre-cooled solvents to ensure better mixing and uniform polymerization. This approach helps distribute nanoparticles evenly throughout the polymer matrix.

5.3.1.6 Reaction time.

The reaction time was studied and considered at 2-, 5-, and 24-hours intervals. It was found that 2 hours is insufficient to obtain mechanically stable materials, regardless of the concentration. When

oxidant and monomer concentrations are low, 2 hours is inadequate to form a complete film; it breaks easily and is difficult to remove from the reactor. Similarly, 5 hours is insufficient to achieve properly built films and gels. It was determined that 24 hours is optimal for synthesis, as the microemulsion requires time to stabilize and form interfaces after mixing. Depending on the surfactant concentration, stabilization time can vary. After 24 hours, all 2D and 3D materials are well-developed and mechanically stable, allowing them to be easily removed and washed without breaking.

CONCLUSION

We successfully synthesized 3D continuously porous polypyrrole gels with moderate porosity and high pore volume, making these materials promising candidates for energy storage applications. The electrical conductivity demonstrated by these 3D polymers is among the highest recorded for this type of bulk material. Our comprehensive study of the factorial dependence of property-morphology relationships in the synthesized materials provides a foundation for further investigation into their applications and potential modifications. The proposed methodology facilitates the fabrication of 3D hybrid conducting polymer gels. The next chapter will focus on 2D and 3D hybrid conducting polymer (HCP) composite materials and their diverse applications.

CHAPTER 6. APPLICATION OF HYBRID CONDUCTING POLYMERS SYNTHESIZED VIA BICONTINUOUS MICROEMULSION POLYMERIZATION METHOD

During this work we successfully synthesized the following composite materials and studied their applications:

- **2D PPy@Co_3O_4/Ag** composite film by non-ionic BME method for antibacterial behavior analysis.
- **3D PPy-Seb.Linker-N-CDots** for Heavy Metal Detection by surfactant-free BME method.
- **3D PPy_CoO** for Flexible Micro-supercapacitor for energy storage applications.
- **3D PPy_Graphene** for Flexible, ultra-sensitive hydrogen gas sensor at Room Temperature.

6.1 Bioelectrochemical Performance of Polypyrrole Films for Wastewater Treatment and Antibacterial activity of 2D PPy@Ag/Co_3O_4 Composite with *Bacillus Subtilis.*

6.1.1 Introduction

Wastewater treatment is an increasing global concern, growing at a rate of approximately 2% annually, and almost 48% of produced wastewater discharged into the environment untreated.[131] While several methods, including physical, chemical, and biological techniques are available, they have unsolved limitations such as low efficiency, high operational cost, energy consumption, and hazardous by-products.[132,133] As a result, there is an urgent need to develop innovative technologies for more effective wastewater management.

A bioelectrochemical system (BES) is a promising solution, capable of treating wastewater and recovering resources from wastewater.[133] This technology is efficient, simple, cost-effective, and easy to operate, but its operation depends significantly on the induced ability of electroactive bacteria to transfer electrons extracellularly to or from a solid electrode.[134] Bioaugmentation of BES with such bacteria has also been established as a promising strategy for improving wastewater treatment processes and resource recovery. Among these bacteria, *Bacillus subtilis (B. subtilis)* is of particular interest due to its ability to transform both organic and inorganic compounds in wastewater.[135] This Gram-positive bacterium demonstrates high nitrate reduction capability and extracellular enzyme activity. It can also grow under anaerobic conditions through nitrate ammonification and fermentation processes, making it an excellent candidate for biological wastewater treatment. However, the efficiency of BES remains a significant challenge.[22] Consequently, there has been no research on using 2D conductive polymers in BES for wastewater treatment. The proposed study would, therefore, investigate the novel bioelectrochemical system of 2D conductive polymers for improved wastewater treatment using *Bacillus subtilis.*

The physicochemical characteristics of 2D materials exceed the properties of existing 0D or 1D materials due to the porous structure, high specific surface area, better charge carrier separation, and the ability of host-guest species. The design of modified dimensional structures of conductive polymers adjusts electrical, mechanical, and optical properties and broadens the possible application fields of these materials. However, synthesizing 2D conductive polymers and their nanocomposites with tunable and controllable morphology and physical and chemical properties remains challenging.

The proposed approach allows the one-step fabrication of free-standing 2D polypyrrole nanosheets with nanocomposites by a bicontinuous microemulsion system to develop a multifunctional integrated system. The interconnected structure of the bicontinuous oil-water system under interfacial polymerization allows the fabrication of a layered PPy films. The fabricated 2D polypyrrole films serve as a solid working electrode, enhancing the electron transfer efficiency, bacterial growth, and metabolic activity of *B. subtilis*, which typically exhibit weak extracellular electron transfer (EET) activity due to non-conductive cell wall. Meanwhile, PPy@Ag/Co_3O_4 composite films will be tested for antibacterial performance, evaluating their ability to inhibit microbial growth. The conductive nature of PPy plays a critical role in the antibacterial mechanism by enhancing electron transfer, promoting ROS generation, and maintaining nanoparticle dispersion. These features, combined with the flexibility and biocompatibility of PPy, provide advantages over traditional non-conductive matrices, positioning the 2D PPy@Ag/Co_3O_4 composite as a promising material for antibacterial and environmental applications.

A key aspect of the research is focused on bacterial adhesion to 2D polypyrrole nanosheets and its impact on wastewater treatment efficiency. Bacterial adhesion is influenced by surface properties such as roughness, charge, degree of hydrophobicity, and hydrogen bonding capacity. To investigate interactions, Atomic Force Microscopy (AFM) was used to study surface properties and bacterial attachments on films synthesized with two different bicontinuous interfaces, nonionic and pure (surfactant-free). Bacillus subtilis are weak electricigens and crucial in many industrial biological processes. Improving EET capabilities of *B. subtilis* through conductive polymer electrodes may significantly enhance its metabolic activity and wastewater performance.

6.1.2 Results and discussions

6.1.2.1 Characterization of 2D PPy@Ag/Co_3O_4 films.

The TEM images provided offer detailed insights into the morphology and structure of the synthesized nanoparticles. Figure 6.1 (a) depicts Co_3O_4_Ag nanoparticles with a scale of 100 nm, highlighting the well-defined cubic shape of the nanoparticles and their uniform distribution. Co_3O_4 and Ag within the same framework suggest successful synthesis and potential synergistic effects in catalytic or electronic applications. Image (b), at a scale of 10 nm, focuses on Ag nanoparticles, revealing a high degree of crystallinity as evidenced by the lattice fringes. This level of detail confirms the formation of pure, crystalline Ag nanoparticles, which are crucial for their intended applications in antimicrobial activity and electronic conductivity. Image (c) presents Co_3O_4 nanoparticles at a 20 nm scale, showing larger cubic structures than the Ag nanoparticles.

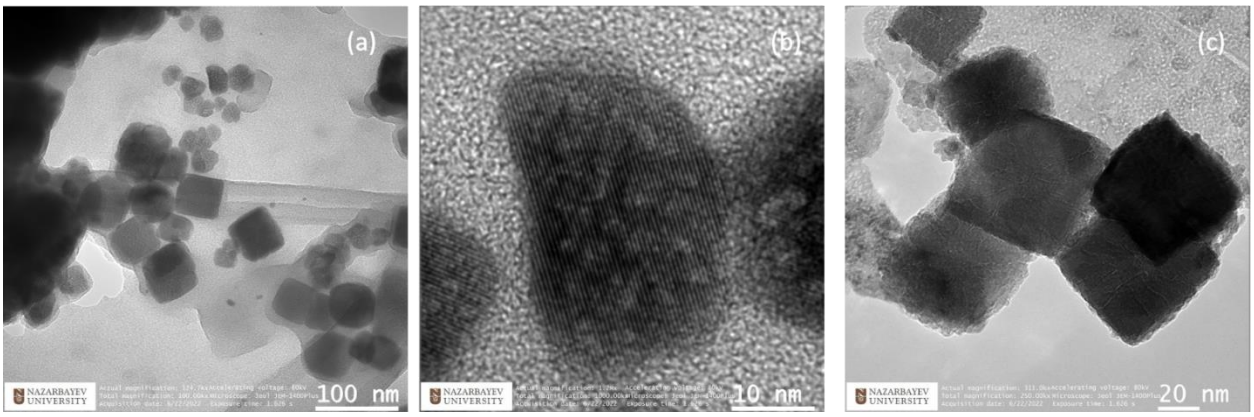

Figure 6.1. TEM images of (a) Ag/Co_3O_4_ NP, (b) Ag NP, and (c) Co_3O_4 NP.

Figure 6.2 A, B, and C show SEM and EDS analysis results of the Ag/Co_3O_4 nanoparticles, revealing a rough surface morphology with evenly distributed Ag nanoparticles on the Co_3O_4 matrix, suggesting a homogeneous synthesis process. Image B, an EDS mapping, illustrates the distribution of Co (in pink) and Ag (in red) elements across the sample. The uniform distribution further confirms the successful incorporation of Ag into the Co_3O_4 structure, which is essential for enhancing the composite's catalytic properties. Image C presents the EDS spectrum, quantitatively confirming the presence of Co and Ag in the sample. The peaks corresponding to Co and Ag indicate that Co makes up 87.4 wt% of the material, while Ag constitutes 12.6 wt%. This elemental composition aligns with the intended synthesis proportions and suggests that incorporating Ag into the Co_3O_4 matrix was successful. Images D and E are TEM images of the PPy@Ag/Co_3O_4 composite. In image D, the nanoparticles exhibit sizes ranging from approximately 27.92 nm to 97.41 nm, indicating a successful synthesis of the composite with a broad size distribution. The image highlights the composite nature of the material, where polypyrrole (PPy) effectively coats the Ag/Co_3O_4 nanoparticles, providing enhanced structural integrity and potentially improved functional properties. Image E, taken at a higher resolution of 20 nm, shows the detailed morphology and intimate mixing of the PPy with Ag/Co_3O_4 nanoparticles. This close interaction is crucial for applications that rely on efficient electron transfer and catalytic activity.

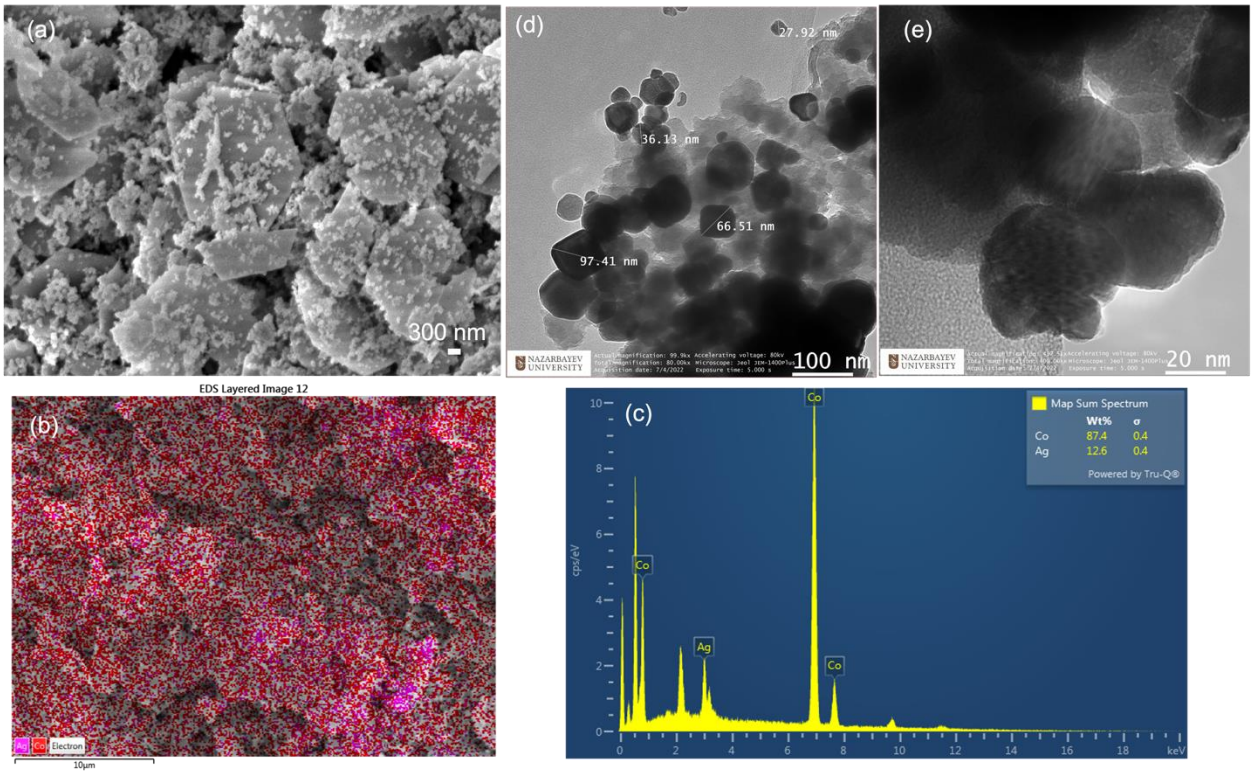

Figure 6.2. A,B,C are SEM and EDS elemental mapping of synthesized Ag/Co_3O_4 NPs. D and E are the TEM images of $PPy@Ag/Co_3O_4$ composite.

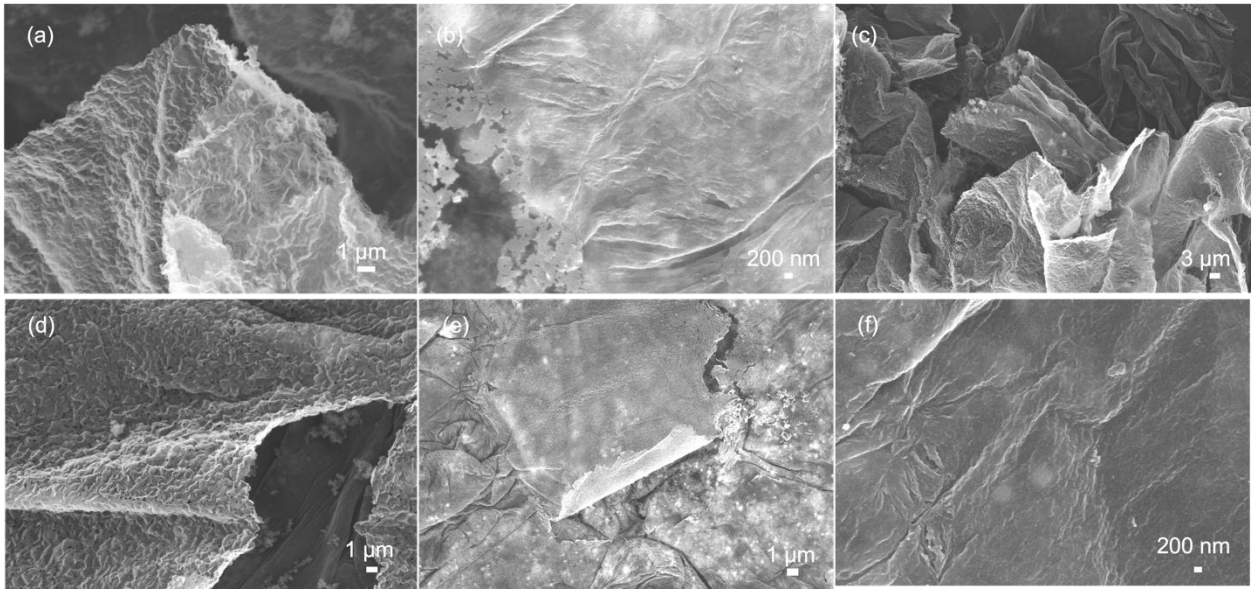

Figure 6.3. SEM images of $PPy@Ag/Co_3O_4$ composite film.

SEM images (Figure 6.3 and Figure 6.4) and EDS mapping analysis demonstrate the successful synthesis of $PPy@Ag/Co_3O_4$ composite films with varied morphologies, including rough, layered, smooth, and fibrous structures. The heterogeneity observed in these images indicates the complex

interactions between the components during synthesis. Such diverse morphologies are likely to contribute to the composite's multifunctional properties, making them suitable for various applications.

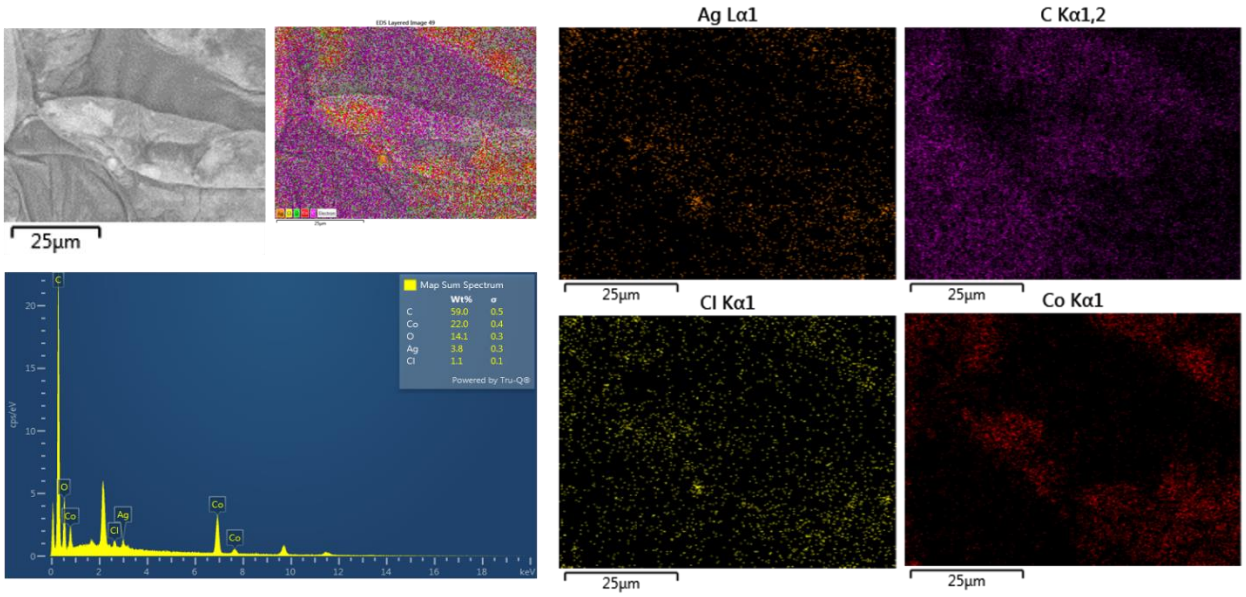

Figure 6.4. Elemental mapping (EDS) of PPy@Ag/Co_3O_4 composite film.

The X-ray diffraction (XRD) patterns presented in the graph provide critical insights into the crystalline structure of the pure PPy, PPy@Co_3O_4, and PPy@Ag/Co_3O_4 composites. (Figure 6.5) The XRD pattern of pure PPy indicates broad peaks around 20-25 degrees, which is characteristic of the amorphous nature of PPy. The red curve corresponds to the PPy@Co_3O_4 composite. The XRD pattern exhibits several sharp peaks, indicating the presence of crystalline Co_3O_4 within the composite. The prominent peaks at 2θ values around 31.3°, 36.9°, 44.8°, 59.4°, and 65.2° can be indexed to the (220), (311), (400), (511), and (440) planes of cubic Co3O4, respectively.[121]The blue curve represents the PPy@Ag/Co_3O_4 composite. This pattern shows the characteristic peaks of Co_3O_4 and additional peaks attributable to Ag. The peaks at 2θ values around 38.1°, 44.3°, and 64.4° correspond to the (111), (200), and (220) planes of face-centered cubic (fcc) silver, respectively. These Ag peaks alongside the Co_3O_4 peaks indicate that the Ag nanoparticles are well-distributed within the PPy@Co_3O_4 matrix. The combination of these materials is expected to enhance the composite's electrical conductivity, catalytic activity, and antimicrobial properties due to the synergistic effects of the metal and metal oxide components.

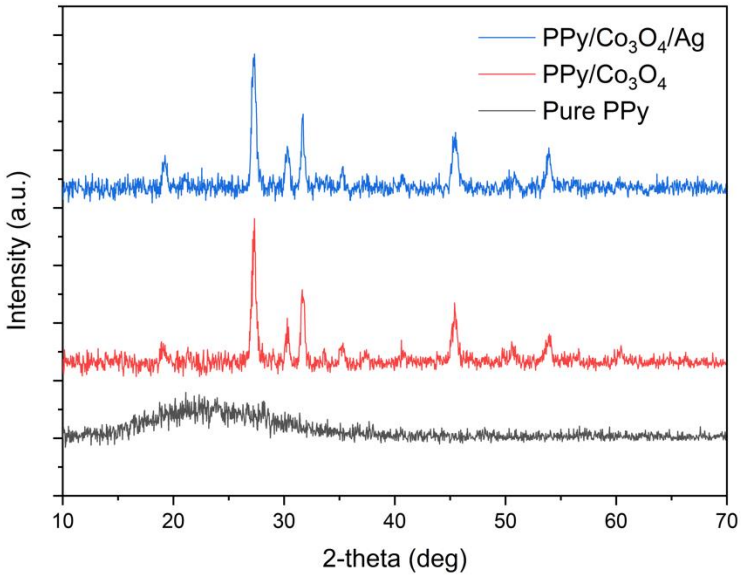

Figure 6.5. XRD spectra of Pure PPy film and PPy@Co_3O_4, PPy@Ag/Co_3O_4 composite films.

6.1.2.2 Characterization of Pure PPy nanosheets and their bacterial attachment properties. Pyrroles-based polymers (PPY) were synthesized using a bicontinuous emulsion system under two interface conditions: nonionic (PPY_NBC) and pure (PPY_PBC). Chapter 4 provides a detailed description of the experimental procedure. The films were characterized by atomic force microscopy to assess their surface morphology, electrostatic properties, and mechanical behavior.

Table 6.1. Mean values of the electrical, physical, and mechanical properties of 2D polypyrrole synthesized by nonionic and pure bicontinuous microemulsion interfaces.

Polymer Composition	Surface Potential (mV)	Roughness Ra(nm)	Young's Modulus (MPa)
PPY_NBC	240.0	231.7	198.3
PPY_NBC_Ag/Co_3O_4	-103.4	319.3	170.3

Polymer Composition	Surface Potential (mV)	Roughness Ra(nm)	Young's Modulus (MPa)
PPY_PBC	104.15	357.8	1993.9
PPY_PBC_NCDs	210.02	240.09	176.6

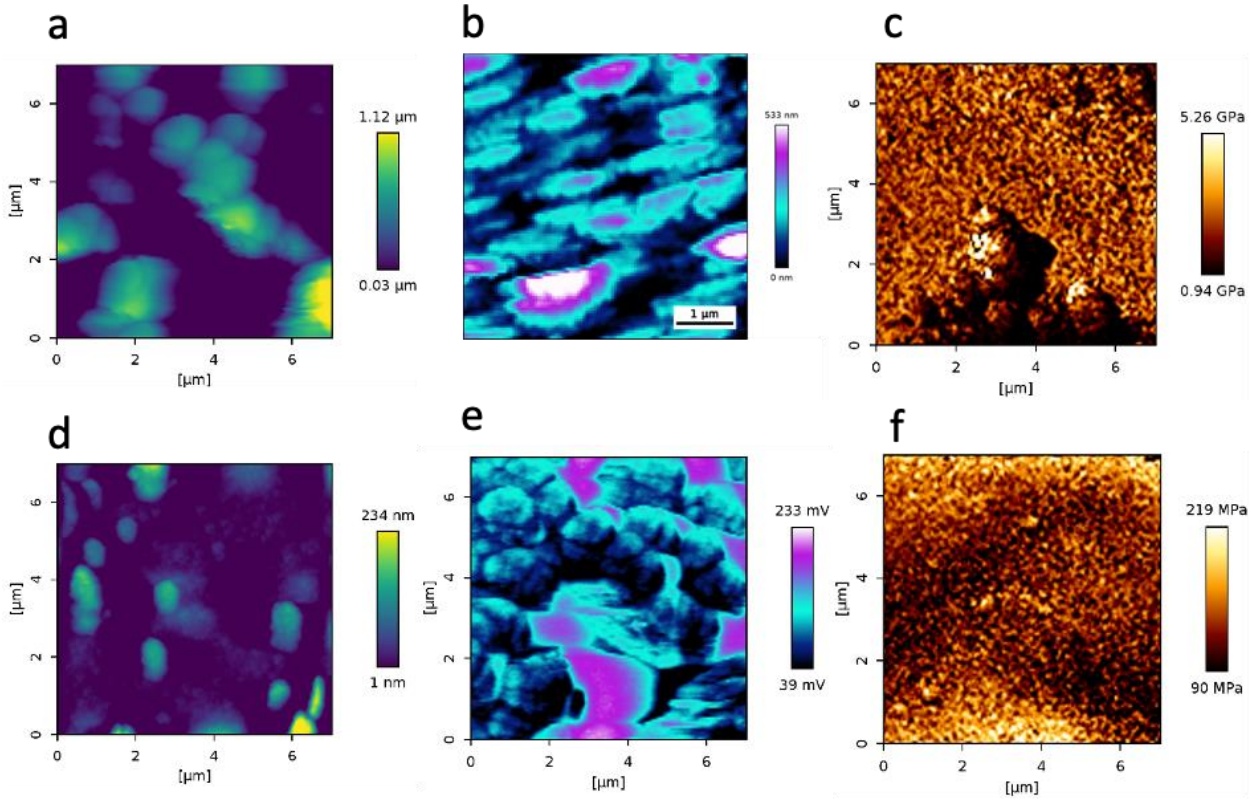

Figure 6.6. Topographic images of roughness, surface potential, and stiffness of PPY_PBC (a-c) and PPY_NBC (d-f) in a 7x7 µm region obtained by AFM measurements. Height and surface potential images were simultaneously obtained using KPM mode. Stiffness images were obtained using QI mode. The color bar represents the level/strength of the measured properties.

The AFM images revealed distinct differences in the surface topography between the PPY_NBC and PPY_PBC. (Figure 6.6) The top row of images (Figure 6.6 a,b,c) show the PPY_NBC composite, which exhibited a smoother surface with less pronounced features. In contrast, PPY_PBC composite in the bottom row (Figure 6.6 d,e,f) characterized by a rougher and more textured surface. The roughness (Ra) values quantitatively confirmed these observations, with PPY_NBC showing mean roughness of 231.7 nm and PPY_PBC a higher Ra of 357.8 nm. This higher roughness in PPY_PBC indicates greater surface irregularity, which could influence the material's interaction with the environment, particularly in applications requiring high surface area. AFM-derived surface potential images provided insight into electrostatic activity of the films. PPY_NBC showed a higher mean surface potential of 240.0 mV compared to 104.15 mV for PPY_PBC. This significant difference suggests that PPY_NBC has greater electrostatic activity,

which could elevate its performance in applications where surface charge plays a crucial role, such as in electronic devices, catalysis or sensing. The stiffness of the films was evaluated by Young's modulus. The PPY_NBC film had a mean value of 198.3 MPa, while PPY_PBC film had much higher mean value of 1993.9 MPa. The results concluded that bicontinuous synthesis method influences morphology and enhances the mechanical robustness of PPY_PBC films, making it a promising candidate for durable and structurally demanding applications. In contrast, PPY_NBC film's smoother surface and higher surface potential make it more suitable for applications where surface interactions and electrical properties are more critical. The films were then analyzed with a Leica Thunder Imager microscope using 20X and 100X objectives. The obtained images were processed using Imaris (Bitplane) and Fiji (ImageJ) software.

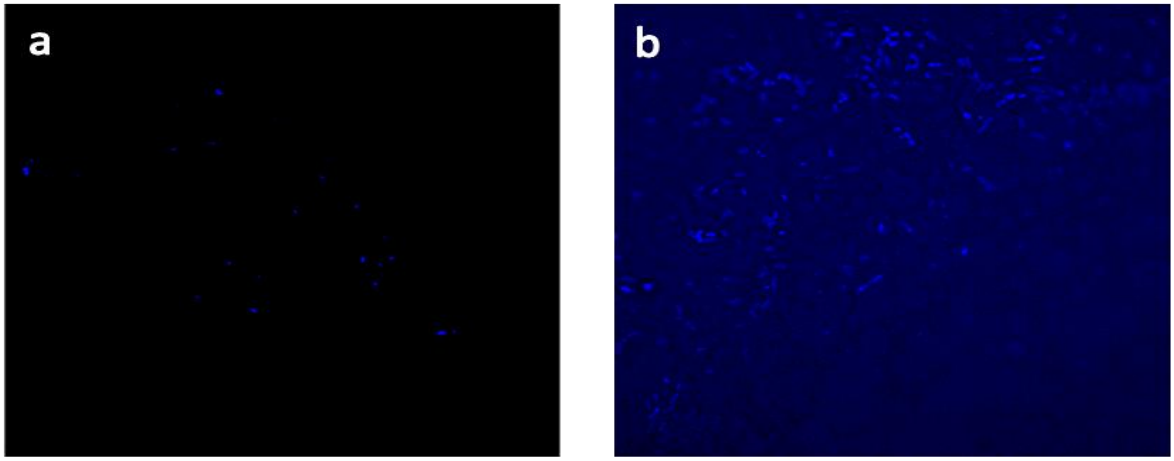

Figure 6.7. Microscopy images (x100) of B. Subtilis attached to the polymer film. The image shows *B.subtilis* with blue-emitted fluorescent staining attached to (a) PPY_PBC film and (b) PPY_NBC film.

This part of the study focused on a fundamental investigation of how the surface charge, film roughness and mechanical properties of conducting polypyrrole films influence bacterial adhesion. Figure 6.7 displays the blue-emitted fluorescent microscopy images of *B. subtilis* attachment to PPy films synthesized at two different interfaces: nonionic (PPY_NBC) and pure (PPY_PBC). As can be seen from the images, a higher population of attached bacteria on PPY_NBC, indicating stronger bacterial adhesion on nonionic interface. However, it was observed that the attachment strength did not correlate with the roughness or stiffness. For instance, PPY_PBC, which exhibited the highest Young's modulus (1993.9 MPa), but the

lowest population of attached *B. subtilis*. Conversely, PPY_NBC, with a lower Young's modulus (198.3 MPa) showed a comparatively higher population of attached bacteria. Similarly, although PPY_PBC had higher surface roughness (357.8 nm) compared to PPY_NBC (231.7 nm), it demonstrated lower bacterial adhesion, suggesting that roughness alone has minimal effect on attachment of *B. subtilis*. The key finding was that surface potential plays a dominant role in regulating bacterial adhesion. PPY_NBC, which had a higher surface potential 230 mV, supported better bacterial attachment than PPY_PBC with lower surface potential 104.15 mV. This indicated that the surface potential is the main factor influencing bacterial adhesion of synthesized PPy films.

Following adhesion studies, bioelectrochemical experiments were carried out to assess the performance of 2D PPy films as working electrodes in the presence of bacterial cells. These experiments were crucial for evaluating and understanding the interaction between *B. subtilis* cells and PPy electrodes, determining the influence of surface properties on electron transfer processes.

6.1.3 Designing the electrochemical setup with polymer films to study biofilm formation.

The polymer films were employed as a working electrode (WE) in the electrochemical cell and were applied to various substrates. During the experimental studies, several electrode designs were developed to optimize film attachment and electrical performance.

1. **Initial design:**

- A thin carbon paper (1 cm x 1 cm) was used as a substrate (Figure 6.8 (i)).
- Although the polymer film covered the surface entirely, the film's attachment was weak.
- Silicon glue was applied to improve attachment (Figure 6.8 (ii)), but the attachment remained insufficient.

2. **Optimized design:**

- To address these challenges, a new electrode system was developed using a carbon substrate covered with copper tape (Figure 6.8 (iii)).

- The polymer film was placed on top of the tape (Figure 6.8(iv)), resulting in significantly improved attachment and structural stability.

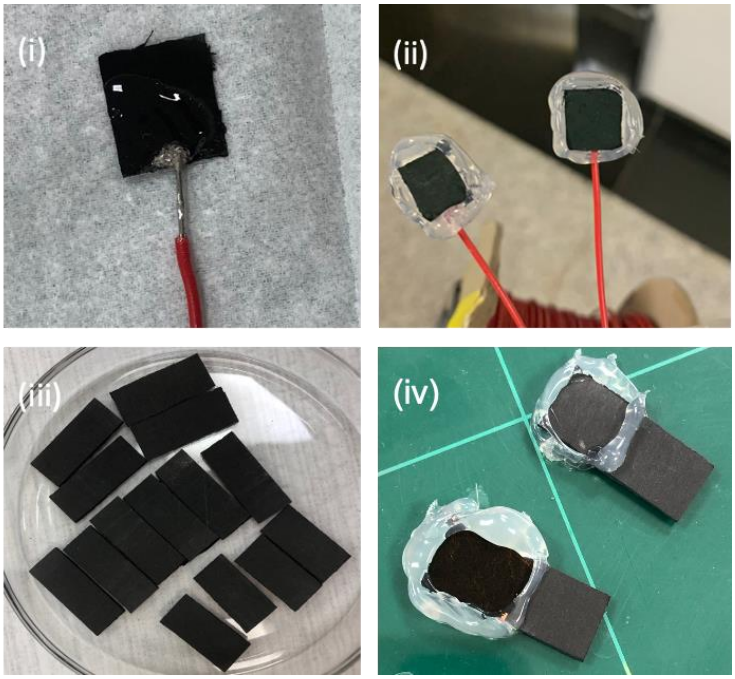

Figure 6.8. The design of the working electrode with a polymer film.

6.1.3.1 The bioelectrochemical cell assembly with polymer working electrode.

Bioelectrochemical cells (BECs) are specialized electrochemical systems that use microorganisms, such as bacteria or yeast, to facilitate electrochemical reactions. These cells facilitate the conversion of organic molecules into electric current through a combination of biological and electrochemical processes.

- Biofilm formation:

The bacteria are grown on the surface of an electrode, forming a biofilm that consists of a community of bacteria collaborating to oxidize or decrease organic molecules.

- Electron transfer:

Electrons generated during metabolic activity of the bacteria are transported to the surface of electrode, resulting in the production of an electric current.

Bioelectrochemical cells are used in wastewater treatment, bioremediation, and bioenergy generation. They provide a sustainable and efficient approach for converting organic materials into a usable form or eliminating impurities from water. This research explored the potential of conducting polymer film as the working electrode to enhance the performance of bioelectrochemical cells.

Figure 6.9. The bioelectrochemical cell is assembled with a polymer film.

6.1.4 Bacterial growth on PPy substrate results.

Bacillus subtilis growth rates were measured in 48-well plates using a Gen5TM Microplate Reader and Imager Software (BioTek Instruments). Growth was measured at 600 nm, and experiments were conducted in triplicates, with mean ± standard deviation (SD) values reported. Growth studies involved the use of a nutrient broth medium.

6.1.4.1 Bioelectrochemical analyses

- Chronoamperometry (CA)

CA is used to monitor the current output over time. It is a fixed-potential technique. Thus, it does not elicit a charging current that may interfere with the electrochemical signals, making it well-suited for weak electricians.[133] CA allows a direct, real-time measurement of electroactivity[134] and could provide reliable physiological details on the metabolic state of cells in the biofilm, thus

making it a suitable approach for distinguishing between live and dead cells – an essential feature lacking in all conventional gold standard methods for characterizing microbes.

In CA, the WE electrode is mostly poised at a single potential, which is optimal for the organism under study. The too-low or high potential may not elicit a measurable EET rate or negatively impact the organism, leading to membrane damage[135,136]. At high potential, the electrode itself or specific medium components may participate directly in the redox reactions, thus affecting the accuracy and reliability of the current output. Therefore, control experiments are always needed to ascertain that the current output is generated only from the biofilm cells. Furthermore, a typical CA curve for early biofilm formation on a flat electrode is like the sigmoid growth curve of any microbe, as current output often rises gradually within the first few hours, corresponding to rapid attachment and growth of cells, and becomes stable after a certain period, as the accumulation of non-conductive biofilms matrix block part of the electrode surface. Depending on the prevailing conditions, the current may remain stable and then decay over time, suggesting growth suppression, cell removal from the electrode surface, or even death due to a combination of depleted nutrients and accumulation of toxic metabolites.[137]

- Voltammetry: Cyclic voltammetry (CV) and differential pulse voltammetry (DPV)

Voltammetry is generally used to detect, characterize, and quantify redox species in electron transfer processes.[138] Contrary to amperometry (CA), voltammetry provides information only about the interfacial electron transport at the electrode surface but not metabolic current, at least at high scan rate values. However, Multiple cycles are possible, making it a technique of choice in studying intermediate reactions and monitoring the redox species' stability.[139]

In cyclic voltammetry (CV), the potential is scanned within a range and in both forward/positive and reverse/negative directions while the resulting current is recorded. The appearance of peak current(s) in the presence of biofilm cells but absent in the control with no biofilm cells indicates redox species produced by the biofilm cells that ferry electrons to the electrode surface.[138] However, the intermittent varied potentials may produce charging currents, so appropriate caution is advised when the CV is applied for weak electricigens. CV at low scan rates (e.g., < 5 mV/s) is suitable to observe turnover redox reactions, while higher scan rates are adopted to characterize redox reactions under non-turnover conditions. The pulse methods (e.g., DPV), where the potential

is either held constant or varied at a constant rate, could be used to mask the charging currents, thus increasing the analytical sensitivity.[133] In a typical pulse voltammetry method, a potential pulse (+/-) is over-imposed on a potential slope, and a short time between the pulses allows the redox pool at the interface to be recharged. The current is recorded before and after each pulse, and the difference (delta I) is plotted as a function of the pulsed potential.[139]

The present investigation involved performing cyclic voltammetry (CV), differential pulse voltammetry (DPV), and chronoamperometry (CA) on several experimental iterations. These tests were conducted utilizing a computer-controlled VSP multichannel potentiostat (Bio-Logic, France). Bacillus subtilis cells, with an initial inoculum of 0.5 optical density (at 600 nm), were cultivated in previously reported electrochemical chambers coupled to the potentiostat using solid-state electrodes (SPEs). Before conducting tests, the solid-phase extractions (SPEs) underwent a double surface sterilization process using 70% v/v ethanol. They were then rinsed three times with sterile deionized water, blotted, and left to air dry. The CV parameters were defined as follows: The initial potential (E_i) is -0.3 V compared to the Ag electrode, while the final potential (E_f) is 0.4 V compared to the Ag pseudo-reference electrode. The current is calculated by averaging the values obtained during the last 50% of the step length. The measurements were taken across 10 voltage steps, with scan speeds of 1 mV s^{-1} and 10 mV s^{-1} correspondingly. DPV studies were conducted in the same manner, with identical settings. CV and DPV analyses were performed at the start of the trial and then every 24 hours until the experiment concluded. Afterward, the CA was measured every minute using the set value E_i = 0.4 V vs. Ag for 48 hours. The electrochemical cells were kept at a constant temperature of 37 °C during incubation in a dry bath with the use of steel beads. Experiments were conducted using cyclic voltammetry and differential pulse voltammetry techniques. The scan rates used were 1 and 10 mV s^{-1}, and the potential range was between -0.3 and 0.4 mV.

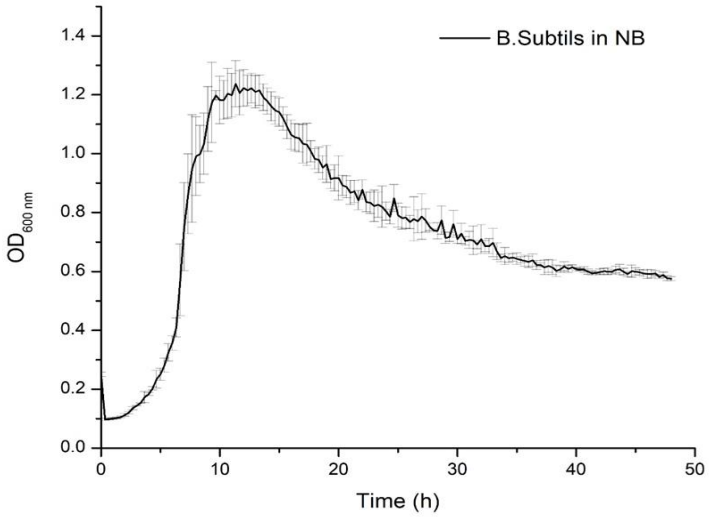

Figure 6.10. The growth pattern of *B. subtilis* in Nutrient broth medium for 48h.

The electrical charge (Coulombs) produced by each test condition was determined by converting the CA data using EC Lab® software (Biologic, France). Plots of growth and electrochemical data were compared to elucidate specific responses on bacterial electroactivity as the control. As presented in Figure 6.10, the lag phase takes almost 3-4 hours. Bacteria need this duration of time to adapt themselves to the environment and get ready for growth. The log phase starts immediately after the lag phase, and bacteria reach the maximum optical density value of 1.2 within 10-11 hours. After maximum growth, bacteria enter the death phase due to the lack of nutrients, physical condition, or injuries to the cell.

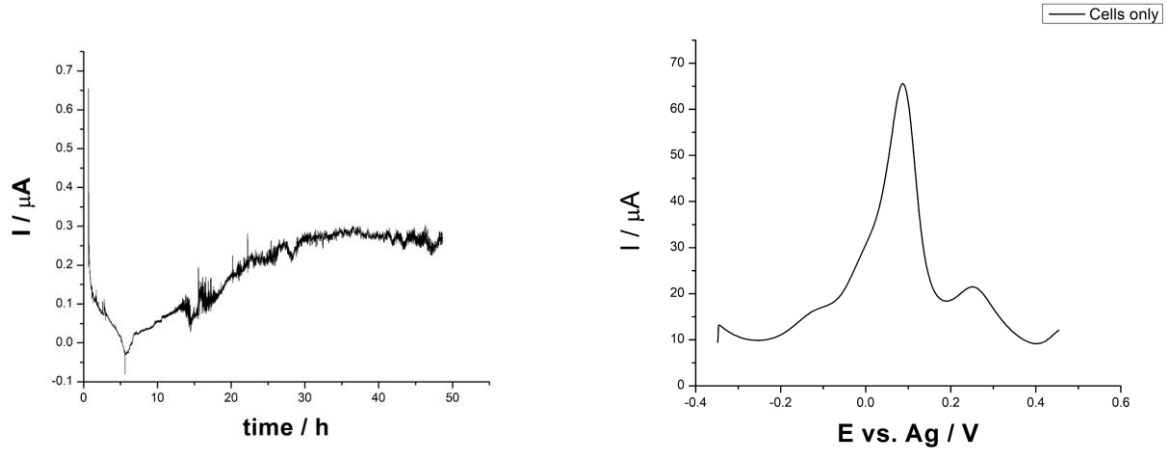

Figure 6.11. The current trend (left) and differential pulse voltammogram (right) of *B.subtilis* in Nutrient broth medium.

The current result from the bacteria as control confirms that *B. subtilis* is a weak electrician, and the produced current is less than 1µA. Differential pulse voltammogram of the bacteria also gives a peak potential of about 70µA, with a peak position of almost 0V.

In another experiment, we examined the electrochemical (EC) behavior of Bacillus subtilis bacteria using cyclic amperometry (CA) and differential pulse voltammetry (DPV) on both polymer-coated and non-coated substrates. The results are presented in Figure 6.11. The findings confirm that the polymer-coated substrate enhances the current compared to the non-coated substrate, with a significantly higher maximum charge for the coated substrate. The DPV peaks obtained from the polymer-coated substrate are not in the same position as those of the non-coated substrate. This could be attributed to the secretion of different materials in the presence of a polymeric substrate. Further experiments are required to obtain a more precise conclusion.

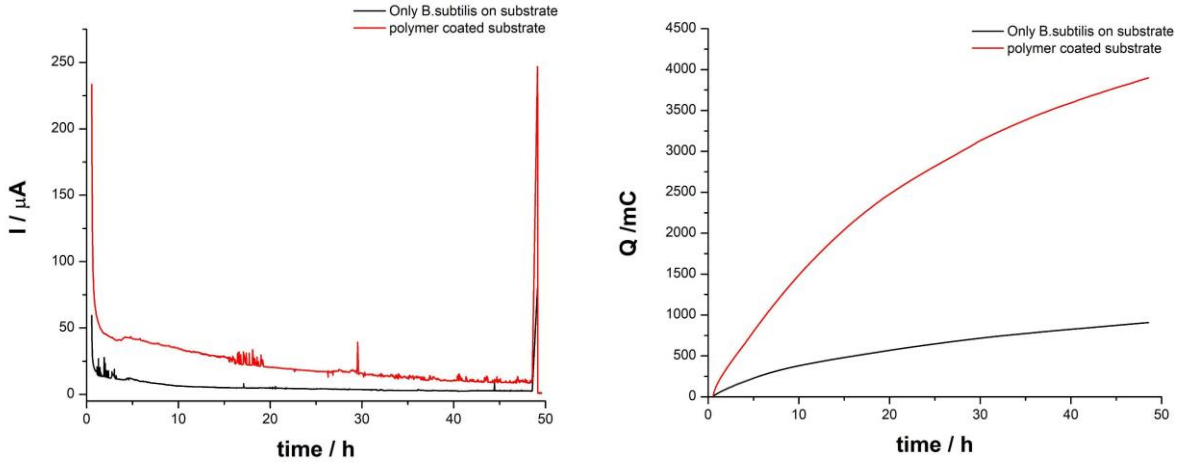

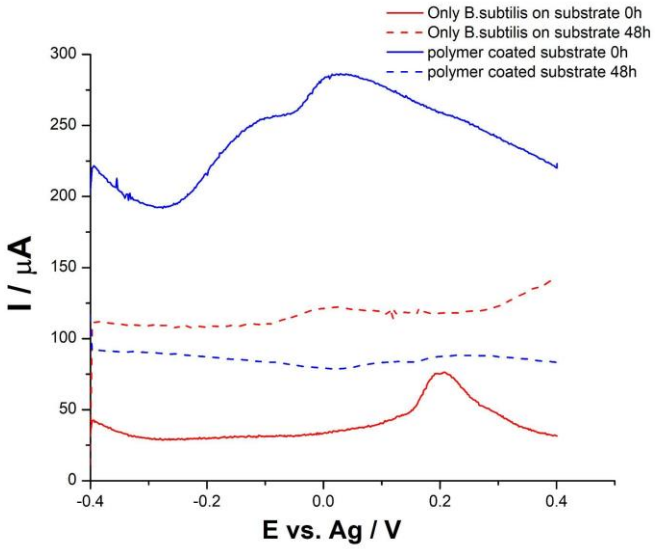

Figure 6.12. The current trend (upper left) and charge (upper right) and differential pulse voltammogram (bottom) of *B.subtilis* in Nutrient broth medium in the presence of polymer-coated graphite substrate and non-coated graphite substrate electrodesю

6.1.5 The utilization of PPy films in the treatment of wastewater.

Microorganisms are the main components involved in biological treatment procedures by breaking down organic material and eliminating nutrients from wastewater. However, incorporating PPy films into these processes can further enhance efficiency in several ways:

1. PPy films have a high capacity to adsorb organic molecules, heavy metals, and their anions/cations from water. This reduces the toxic load on the microorganisms in charge of biodegradation throughout the treatment process.
2. PPy films can serve as electrodes to catalyze the electrochemical oxidation of organic material in wastewater. The removal of nutrients and organic stuff can be improved with biological processes supplemented by this electrochemical oxidation procedure.
3. PPy films may act as a substrate for biofilm formation, providing a surface where microbial communities stick to a surface and cooperate to degrade organic material and extract nutrients from wastewater. PPy films may improve the efficiency of biological treatment methods by the development of biofilm on their surface.

Although PPy films offer potential benefits in biological wastewater treatment, their full benefits and limitations are not yet fully understood.[140-142] Further research is needed to comprehensively

explore their capabilities, particularly about biofilm development, adsorption efficiency, and catalytic performance. Thanks to their flexibility and tunability, PPy films hold great promise for customized wastewater cleaning solutions, offering new avenues for sustainable development.

The electrochemical activity of *Bacillus subtilis* demonstrated a significant increase in the presence of a PPy-coated substrate (Figure 6.12). This is an important finding since it is essential to eliminate impurities and raise the quality of the water for different purposes. Improvement of electroactivity can increase biodiversity and microbial bioactivity. Using *Bacillus subtilis* in wastewater treatment may be more effective due to its ability to control extracellular polymer substances by increasing the release of low molecular weight EPS and quorum sensing molecules and to regulate Na^+ and K^+ transporters by changing membrane potential and promoting ATP synthesis.

6.1.6 Antibacterial activity of PPy@Ag/Co_3O_4 composite film.

Recently, an essential area of research of advanced composite materials for antibacterial applications was developed due to the need for strong antibiotic treatments and the increasing prevalence of antibiotic-resistant bacteria. PPy composites have become desirable alternatives for various applications because of their unique physicochemical properties, especially those combining with metal and metal oxide nanoparticles, forming a multifunctional platform with possible antibacterial benefits.

One of the composite components, namely silver nanoparticles, is widely recognized for its feature to rupture bacterial cell membranes, produce reactive oxygen species, and interfere with microbial DNA replication.[135] The combination with Co_3O_4 provides the synergistic effect to improve its antibacterial performance since the metal oxide has good catalytic characteristics and moderate antibacterial activity. On the other hand, the increase of reactive oxygen species formation and bacterial cell damage can be achieved by the facilitation of electron transfer pathways due to the PPy's conductive nature. In addition, the polymer’s large surface area and porosity allow it to interact with bacterial cells more effectively, increasing its total antibacterial efficacy. The composite's mechanical robustness and chemical stability provide surface coatings susceptible to bacterial contamination in various medical equipment and water treatment systems.

The purpose of this section of the thesis work is to study the antibacterial characteristics of the PPy@Ag/Co_3O_4 composite. Our goal is to demonstrate the potential of our composite as an effective antibacterial agent by investigating the interaction processes and evaluating its

effectiveness in different scenarios. This work provides a route forward for the development of next-generation antibacterial technologies and advances our understanding of composite materials for antimicrobial applications.

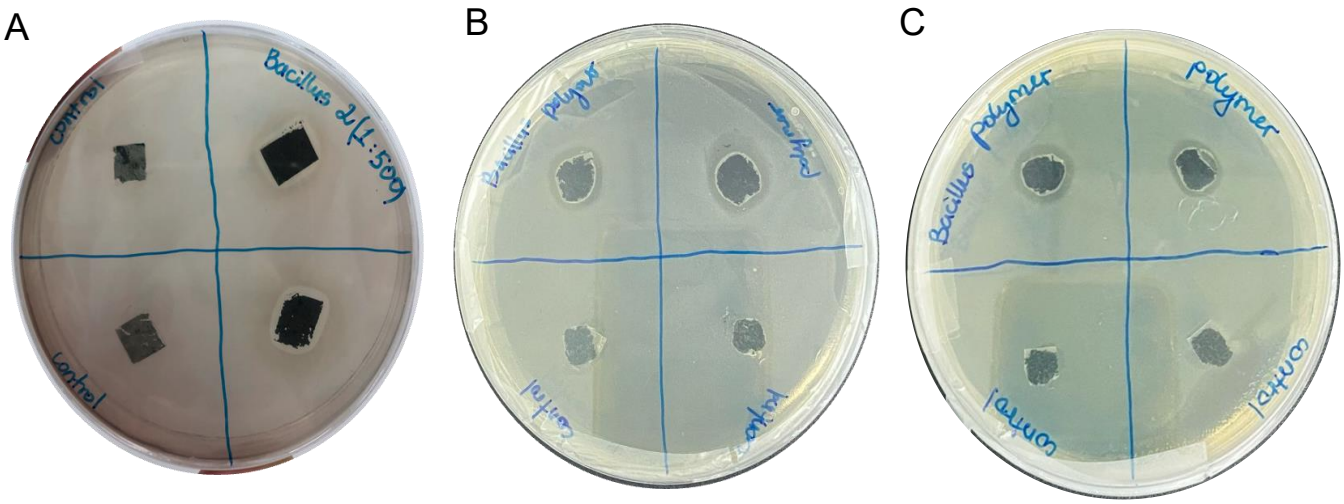

Figure 6.13. 2D PPy@Ag/Co_3O_4 composite films' antibacterial tests: A and B had a 500:1 Py: NPs ratio and C had a 1000:1 Py: NPs ratio.

In this work, two distinct ratios of pyrrole to nanoparticles (NPs), namely 1000:1 and 500: 1, were used to examine the antibacterial properties of PPy@Ag/Co_3O_4 composites. The antibacterial efficacy of these composites was evaluated by measuring the inhibition zones surrounding the samples after they were treated with *Bacillus subtilis*. Figure 6.13 demonstrates that the absence of inhibitory zones in pure PPy, which was utilized as the control, indicates no antibacterial activity. On the other hand, the distinct inhibition zones around the sample area with PPy@Ag/Co_3O_4 films exhibit strong antibacterial activity. The existence and size of these zones provide visual information about the material's capacity to stop bacterial growth. In addition, these above results suggest that the implementation of Ag and Co_3O_4 nanoparticles into the PPy matrix greatly improves its antibacterial properties. Compared to the 1000:1 ratio, the 500:1 ratio composite has a stronger antibacterial activity due to the higher concentration of nanoparticles. This means that there is a direct correlation between the antibacterial activity and the concentration of nanoparticles in the composite material.

CONCLUSION

This part of the study examined PPy-based composites for wastewater treatment applications. It has been demonstrated that pure bicontinuous systems were stiffer and rougher, making them ideal for structural applications. Whereas the introduction of Co_3O_4 and Ag nanoparticles greatly improved the PPy matrix's antibacterial properties. These findings demonstrate PPy-based materials' flexibility and versatility, giving customizable properties for varied applications.

6.2 Synthesis of 3D Polypyrrole-Sebacoyl Linker-N-Cdots Composite for Heavy Metal Detection.

6.2.1 Introduction

Nowadays, environmental pollution is a significant concern for all humankind. The shortage of water resources, the global temperature increase, the discovery of many new diseases due to air pollution, and the short list of urgent environmental issues. Heavy metal ions, such as iron ions (Fe^{3+}), are one of the significant contributors to environmental and health risks. The toxicity and non-degradability of iron ions damage ecosystems due to metal ion contamination. Increased industrial production, such as metallurgy, waste disposal, chemical, agricultural, and electronics, makes this problem even more severe. Efficient detection of toxic metals is essential for monitoring and mitigating hazardous consequences. Carbon dots (CDots) are a class of fluorescent nanomaterials considered a promising sensing material for heavy metal ion detection. The unique properties of CDots, such as excellent optical characteristics, fluorescence, photostability, and high quantum yield, make them very sensitive to environmental changes. The sensing mechanism of CDots in their ability to quench the fluorescence with the interaction of metal ions provides a measurable intensity signal, which can help quantify the presence and concentration of metals. Carbon dots can be functionalized with special ligands or surface functional groups that bind with Fe3+ ions, enhancing selectivity and sensitivity. The major advantages of carbon dots for metal ion detection include their rapid response and interaction with metal ions, which make them suitable for real-time monitoring, environmental stability and operational temperatures, biocompatibility, and environmental friendliness. In this work, we synthesized PPy-Linker-N-CDots films by bicontinuous microemulsion polymerization to create an iron ion sensor. Combining polypyrrole with carbon dots increases the sensitivity and makes detecting iron ions more efficient. Pure carbon dots exhibit self-quenching and agglomeration in a dry state while introducing carbon dots into the polymer matrix extends their working abilities and increases

fluorescence. Conducting polypyrrole facilitates the transfer of electrons and enhances the signal transduction process, which results in a more pronounced and detectable signal change upon interaction with heavy metal ions. Incorporating CDots into PPy films combines the advantages of both materials, creating a composite that is highly effective for heavy metal detection. Moreover, the mechanical stability and flexible nature of the polymer make it suitable for wearable and flexible sensor configurations. The PPy matrix protects carbon dots from environmental degradation, ensuring the sensor's long-term stability and durability.
For this work, we synthesized a unique sebacoyl chloride polypyrrole liner to make a multilayered 3D network. The presence of the linker in the polymer matrix allowed us to catch and fix carbon dots not only on the surface of the film but also within the polymer matrix.
The one-step synthesis approach for creating 3D PPy-Linker-Cdot films simplifies fabrication and reduces production costs.

6.2.2 Results and discussion

6.2.2.1 Physical characterizations

FT-IR spectra of pure polypyrrole and PPy with linker are shown in Figure 6.14. The introduction of linkers to the polypyrrole structure can be characterized by carbonyl stretching at ~1700 cm^{-1} and ~3000 cm^{-1} corresponding to sp^3 C-H, which starts appearing as the number of linkers increases.[122]

During polymerization, it was observed that the pyrrole monomer present in the linker composition competes with the free monomer particles in the reactor system to build the structure. This competition results in varying morphological formations of polypyrrole within the same reactor system. As the linker concentration increases, the structure becomes denser and more well-packed. The porosity decreases with higher linker concentrations; however, the layers tend to form a plate-like structure joined together. Adding the linker to the polymer matrix leads to different morphological structures.

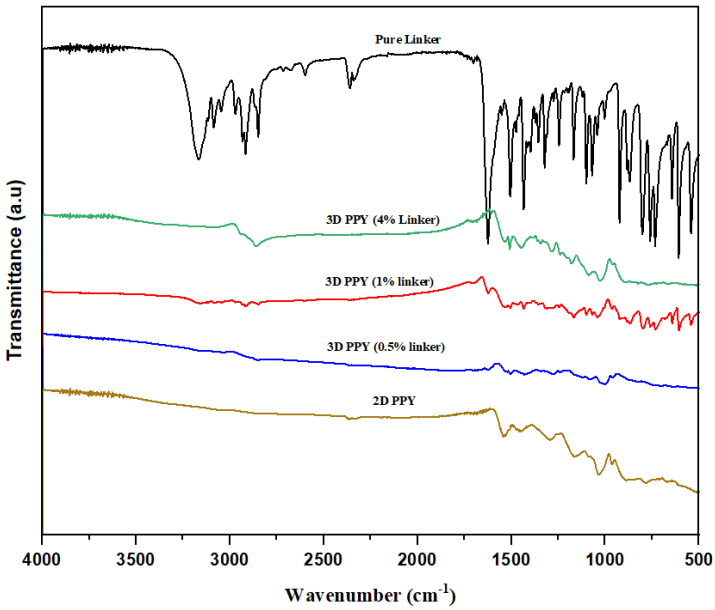

Figure 6.14. FT-IR spectra of pure PPy and PPy-Linker composite with different concentrations of linker.

In some cases, the reactor without the linker can produce a powder structure, while adding the linker can form a 2D film. The reactor may lack sufficient monomer concentration to build a uniform structure. However, when the linker with pyrrole monomer particles is added, it reacts with the PY particles and helps the film grow. So, a monomer-to-linker ratio of 1:100 shows small changes in shape when the monomer concentration is not high enough to form a film inside the system. The added particles from the linker help build a uniform structure. However, when the monomer concentration in the system is adequate, the addition of the linker leads to more particle growth, resulting in a more porous structure. In addition, increasing the ratio of monomer to linker from 0.5 wt.% to 4 wt.% promotes the development of layered plate-like structures (Figure 6.15). The alterations in morphology of 3D- PPy materials were verified using two distinct linkers, namely C6 and C10 lengths.

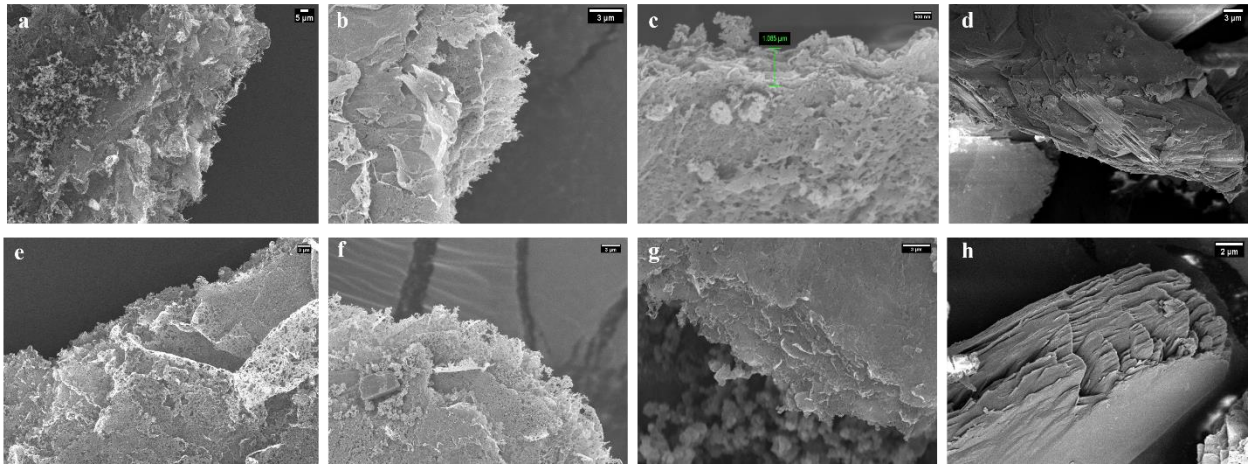

Figure 6.15. SEM images of 3D PPy material with a monomer to linker ratio effect, with the linker having 6 carbon chain lengths (a-d) and 10 carbon chain lengths (c-h). The concentration of the linkers in the monomer is: a) 0.25%; b)0.5%; c)1%; d)4%; e)0.25%; f)0.5%; g)1%; h) 4%.

In Table 6.2, we see the changes in the electrical properties of the film with the linker incorporated into the matrix. The thickness of the 2D film slightly increased, but the effect on conductivity was significant, almost increasing five times.

Table 6.2. Electrical conductivity of the 2D film without linker and with adding linker in ratio 1:50.

PPy_Linker ratio	**Resistivity Ohm/sq**	**Thickness**	**Conductivity (S/cm)**
$FeCl_3$ 2 NL	3 073	145 nm	22
$FeCl_3$ 2 1:50	599	162 nm	103

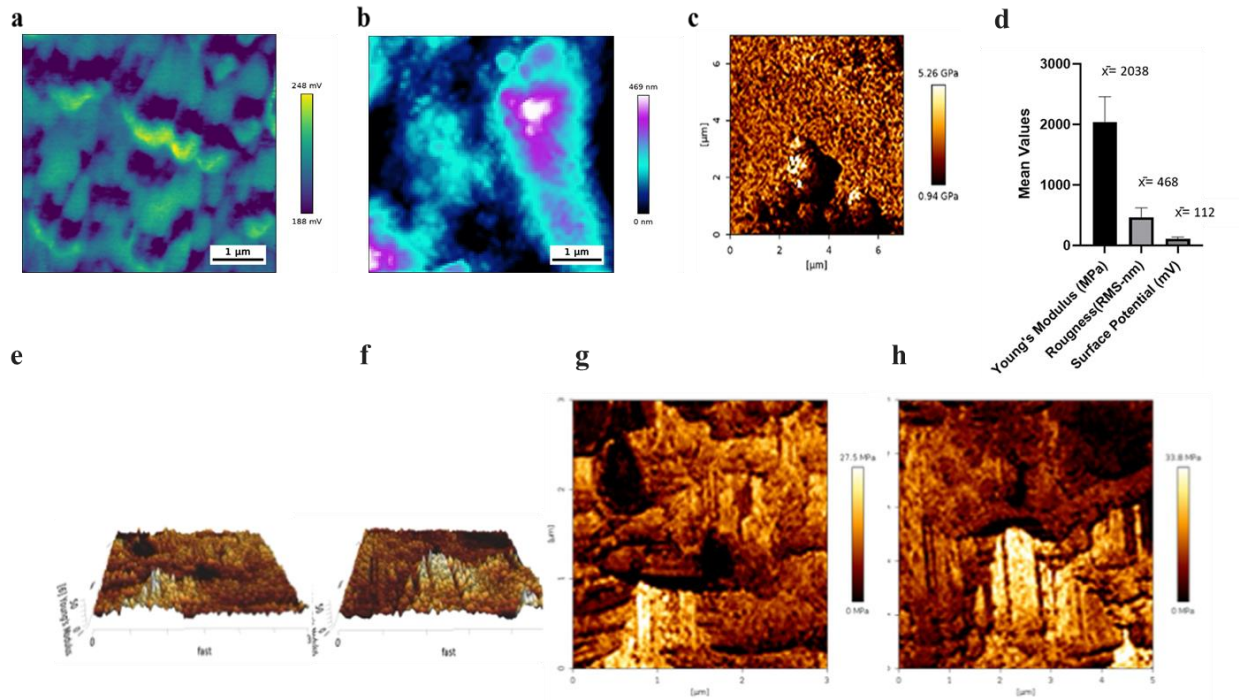

Figure 6.16. The AFM image of the roughness and mechanical properties of the 2D (a,b,c,d) and 3D (e,f,g,h) PPy.

The surface properties of synthesized 2D and 3D polypyrrole materials were analyzed by atomic force microscopy (AFM). A surface potential map of 2D polypyrrole is presented in Figure 6.16a, where surface potential values range from 188 mV to 248 mV, indicating a relatively uniform distribution with moderate roughness. This consistent surface potential across 2D ppy suggests a uniform conductive property of films. The surface roughness ranges from 0 to 469 nm (Figure 6.16b), reflecting a smooth surface with occasional peaks. This smooth surface is suitable for sensor applications or coatings. The mechanical stiffness across 2D polypyrrole ranging from 0.94 GPa to 5.26 GPa indicates heterogeneity in stiffness distribution. (Figure 6.16c) Figure 6.16d indicates the mean values of 2D polypyrrole nanosheets. The surface topography of 3D polypyrrole is significantly more complex and rugged than 2D polypyrrole. The increased surface roughness in the 3D structure is due to the higher surface area of the materials. The high variability in the stiffness modulus suggests a less rigid structure but with higher flexibility and mechanical adaptability. This observation supports the hypothesis that the presence of linkers affects the mechanical properties of polypyrrole.

The important information about the material's surface properties and its porous structure is extracted from the study of 3D PPy using linker. For example, Figure 6.17A shows the adsorption-

desorption isotherms where notable mesoporous and microporous features are revealed. The observed hysteresis loop indicates type IV isotherms, which are typical of mesoporous materials with capillary condensation happening in the pores. BET multipoint analysis (Figure 6.19B) displays a linear connection and validates the surface area measurement's dependability. This provides a certain surface area, which is necessary for high surface contact applications like catalysis or sensing. The structure of the material is further clarified by the pore distribution study (Figure 6.19C). The predominant pore sizes are in the mesoporous range (10–50 nm), contributing significantly to the pore volume and surface area. This distribution is advantageous for mass transport and diffusion applications, as mesopores balance surface area and accessibility. The high percentage of mesopores (56.91% of pore volume and 52.58% of surface area) suggests that the 3D PPy with the linker is well-suited for applications that benefit from large surface areas and efficient molecular diffusion. Despite their small volume fraction, the significant contribution of micropores to the surface area (21.56%) highlights the material's potential for high surface reactivity, which is beneficial for catalytic and sensing applications.

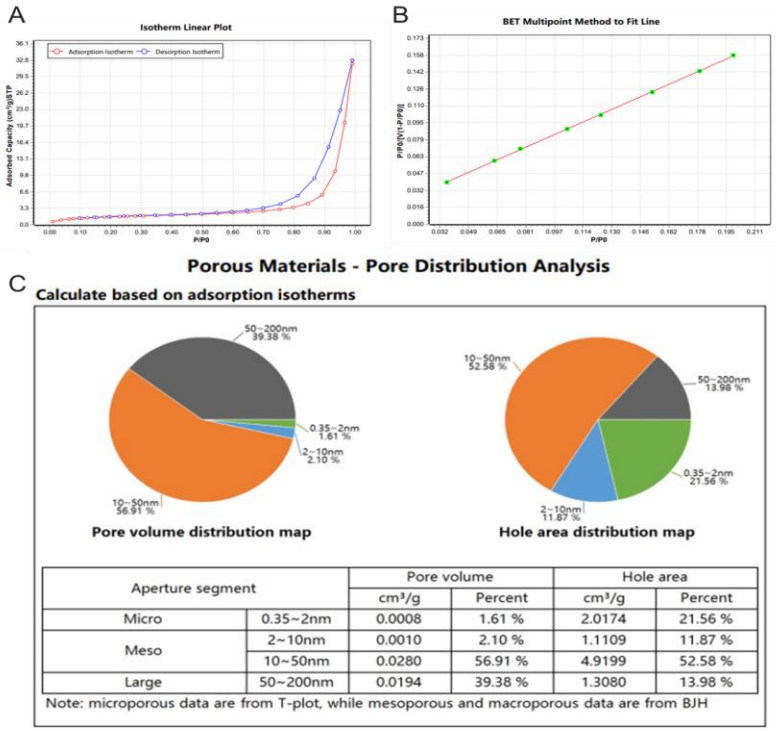

Aperture segment		Pore volume		Hole area	
		cm³/g	Percent	cm³/g	Percent
Micro	0.35~2nm	0.0008	1.61 %	2.0174	21.56 %
Meso	2~10nm	0.0010	2.10 %	1.1109	11.87 %
	10~50nm	0.0280	56.91 %	4.9199	52.58 %
Large	50~200nm	0.0194	39.38 %	1.3080	13.98 %

Note: microporous data are from T-plot, while mesoporous and macroporous data are from BJH

Figure 6.17. A and B BET curve and plot of 3D Polypyrrole with Linker. C) Pore Distribution Analysis of PPy with linker material.

6.2.3 3D Polypyrrole Composites with Linkers and N-Carbon Dots for Heavy Metal Detection Applications.

Carbon dots, as semiconductor materials, are extensively utilized in multiple domains. However, their primary limitation is the self-quenching effect in the dry state due to particle agglomeration, which diminishes light emission duration. Recent advancements have employed the host-guest technique to prolong light emission and mitigate the self-quenching effect. This method not only improves their optical stability but also enhances their sensing capabilities for heavy metal ions. Specifically, iron ions (Fe^{3+}) exhibit the most pronounced quenching effect by facilitating oxidation-reduction (redox) interactions between Fe^{2+}/Fe^{3+} and CDots.

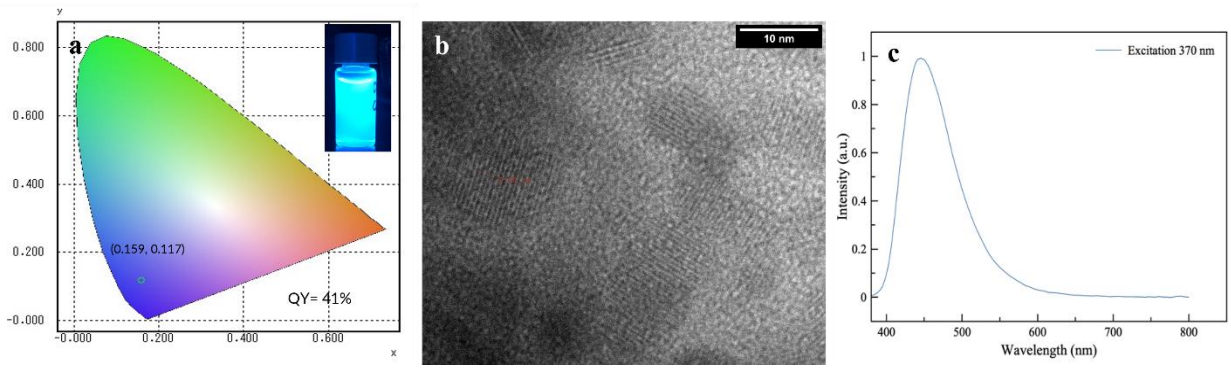

Figure 6.18. a) CIE chromaticity coordinate of carbon dots, b) TEM image of N-CDs, and c) the fluorescence intensity of N-CDs with an excitation peak at 370 nm.[8]

The synthesized N-carbon dots exhibited a 41% quantum yield, which is an excellent value (Figure 6.18a). The TEM image of carbon dots is shown in Figure 6.18b. Synthesized carbon dots didn't show any lattice and were more amorphous. The excitation peak of N-carbon dots was indicated by photoluminescence measurements and placed at 370 nm.

Carbon dots were embedded in polypyrrole films using pure-interface bicontinuous microemulsion system, both with and without addition of linker. The low concentration of oxidant $FeCl_3$ (5 mg ml^{-1}) resulted in a very thin uniform film due to the lower intermolecular interactions, thereby minimizing particle aggregation during synthesis.

The bicontinuous system provided a stable and arranged environment that ensured CDs were well-dispersed throughout the matrix. Additionally, the presence of the linker in the polymer matrix

enhanced the formation of porous structure in the film, further facilitating uniform embedding of the CDs within the polymer. These parameters, along with slower polymerization process, contributed to the even distribution of CDs across the film surface, as confirmed by TEM images of PPy-Linker-N-CD composite. (Figure 6.19)

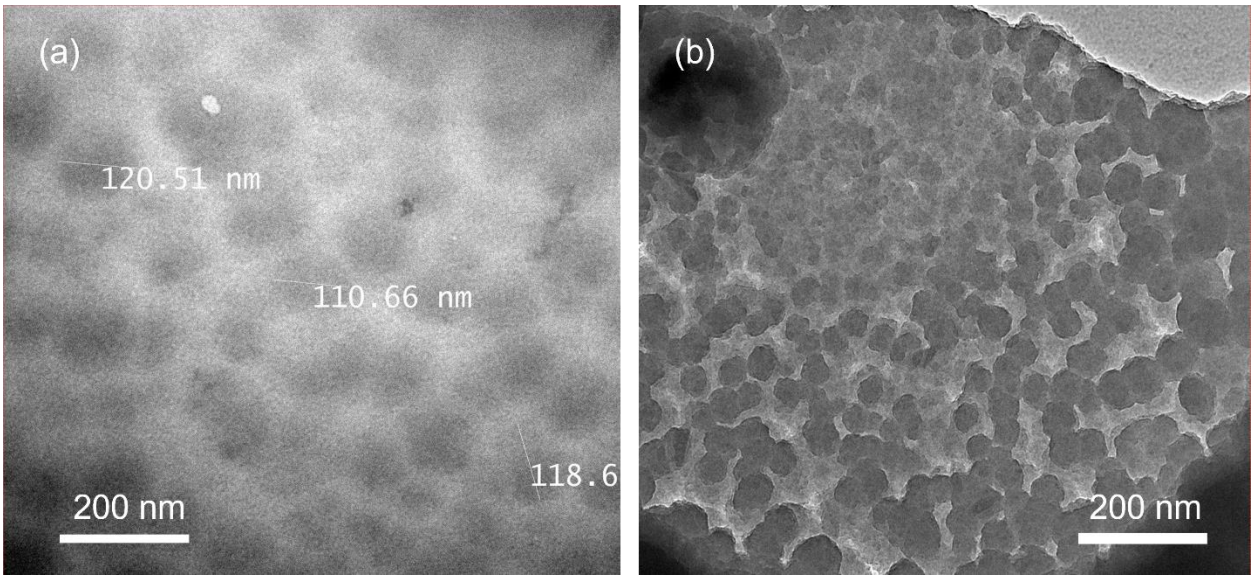

Figure 6.19. A and B are TEM images of PPy-Linker-N-CD composite films showing even distribution of CDs within the polymer matrix.

The fluorescence intensity, change and presence of the carbon dots in the polymer matrix studied in four different samples: pure 2D PPy, 2D PPY-N-CDs, 3D PPy-Linker, and 3D PPY-linker-N-CDs by confocal microscopy technique. (Figure 6.20) The intensity of 2D PPY linearly increased with the presence of the CDs in the matrix and even more with the addition of a crosslinker due to the porous structure formation. Since Fe^{3+} ions have the most significant emission quenching effect on the CDs, the sensitivity of the polymer films was tested using a ferric chloride solution. Additionally, the reactivation of the carbon dots with ascorbic acid demonstrates the presence of the CDs inside the polymer matrix and the ability of the system to incorporate nanoparticles into synthesized conductive polymers.

To confirm the stable incorporation of CDs, a controlled washing procedure was performed by DI water droplets to the film surface. As shown in Figure 6.21, partial reduction of fluorescence intensity occurred after washing, suggesting that only CDs embedded within the polymer matrix remained.

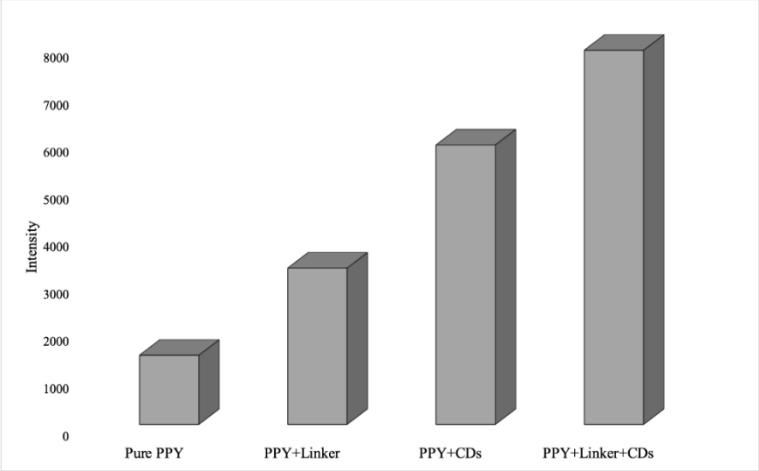

Figure 6.20. Fluorescence intensities change in PPY nanocomposite materials without and with CDs.[8]

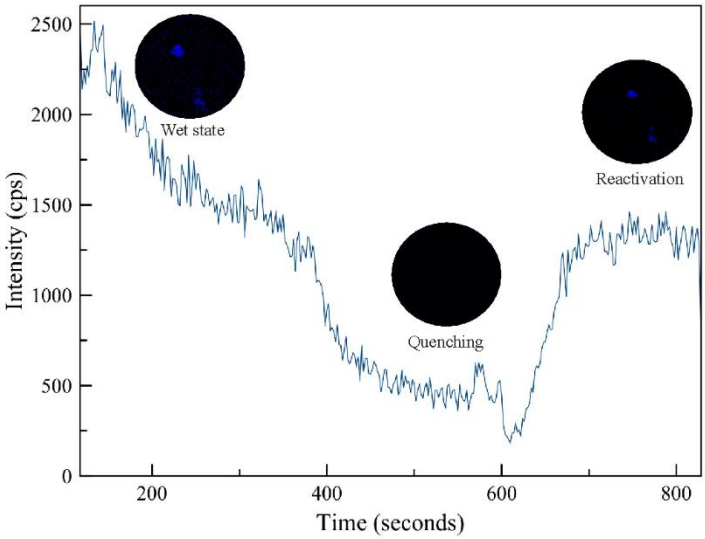

Figure 6.21. Fluorescence intensity quenching and reactivation analysis of Carbon Dots synthesized with polypyrrole by BME polymerization using confocal microscopy.[8]

The quenching experiment was conducted by real-time intensity change detection on the confocal microscope. The fluorescence intensity decreased rapidly, indicating successful quenching. (Figure 6.21) Several minutes later, the addition of ascorbic acid, reducing agent, reactivated the fluorescence of the CDs by reducing Fe^{3+} to Fe^{2+}, restoring the intensity to the washed by water level. The intensity of the CDs cannot be entirely reactivated since the dark polymer layer on the top of the CDs may interfere with the penetration of ascorbic acid to reach the particles.

The mechanism of quenching and reactivation of carbon dots involves complex electron transfer interactions.

Quenching mechanism: Fe^{3+} ions are strong oxidizing agents, they can accept electrons from N-CDs and form complexes with functional groups on the surface of N-CDs, resulting in changes in the electronic structure of carbon dots. This resulted in non-radiative energy transfer, and decreased fluorescence intensity of carbon dots.

Reactivation mechanism: Ascorbic acid donates electrons to reduce Fe^{3+} to $Fe^{2+,}$ reactivating the fluorescence of carbon dots. Fe^{2+} ions have a lower attraction to excited N-CDs, allowing emission to occur.

Polypyrrole facilitates the electron transfer and provides a protective environment for CDs, enhancing their stability and functionality within the polymer.

CONCLUSION

We successfully synthesized a linker contributing to structural rearrangements and morphological changes within the polypyrrole (PPy) matrix. The presence of a linker and the length of its carbon chains influenced the layered morphology of the resulting PPy thick films. Including the linker improved the mechanical properties and enhanced the material's electrical conductivity. The additional layers and sites formed by the linker allowed us to incorporate extra nanoparticles, such as carbon dots, into the polymer matrix. The presence of fluorescent carbon dots in the polymer matrix was confirmed by confocal microscopy. Even after washing the samples with water, the intensity remained high, indicating the stable incorporation of carbon dots within the polypyrrole film. The quenching and reactivation behavior demonstrated with Fe^{3+} ions highlight the potential of the developed composite material for further exploration in heavy metal ion detection. However, additional studies are required to comprehensively assess the material’s performance across various metal ions and conditions.

6.3 Synthesis of 3D Conducting Hybrid Composite Gels for Flexible Micro-Pseudocapacitor (MPC) Applications.

6.3.1 Introduction

Supercapacitors, also known as electrochemical capacitors, have garnered significant attention recently due to their high-power density, rapid charge-discharge capabilities, and long cycle life. These attributes make them ideal for various applications, including energy storage systems, portable electronics, and electric vehicles. However, there is a continuous need to develop advanced materials with enhanced electrochemical performance to meet the increasing energy demands and efficiency requirements. Among various materials, conducting polymers and transition metal oxides have emerged as promising candidates for supercapacitor electrodes.[140,141]

Polypyrrole (PPy), a well-known conducting polymer, has attracted considerable interest due to its excellent electrical conductivity, environmental stability, and ease of synthesis.[52,126] However, structural degradation and limited long-term stability are among the drawbacks of conducting polymers, despite the benefits they offer in practical applications.[142,143] Although it has low conductivity, cobalt oxide (CoO), a transition metal oxide, is well known for its high theoretical capacitance and capacity for redox processes, which greatly aid in energy storage.[144] Integration of transition metal oxides such as MnO_2, CoO, V_2O_5 into conductive polymers is one of the cost-effective solutions.[142,144–148] Conventional sandwich-like or wire like structures of polypyrrole composites are well-studied and proved the promising applicability of the PPy and cobalt oxide based electrode materials as active component for energy storage systems. Wang et al. fabricated a supercapacitor based on mesoporous Co_3O_4 nanostructure and achieved a specific capacitance of 202.5 $F \cdot g^{-1}$ and good stability over 1000 cycles, proving the superior electrochemical performance of porous Co_3O_4 structure over nanorods and nanowires.[149] Sandhya C. P et al. developed a PANi-Co_3O_4-based electrode or supercapacitor with specific capacitance 1151 $F \cdot g^{-1}$ @ 3 $A \cdot g^{-1}$ and excellent cycling stability (92% after 5000 cycles).[150] Cheng Zhou et al. designed a 3D CoO@PPy hybrid nanowire array on nickel foam with outstanding pseudocapacitive performance and high specific capacitance of 2223 $F \cdot g^{-1}$ and cyclability.[151] However, to the best of our knowledge there are yet no studies dedicated to the micro-scale interdigital and flexible

energy storage devices based on hybrid conducting polymer electrodes of cobalt oxide and polypyrrole.

The combination of PPy and CoO in micro-pseudocapacitors (MPCs) offers a novel approach to synergistically enhance the device's overall performance. The significance of PPy-CoO MPCs is found in their capacity to integrate two complementary energy storage mechanisms: cobalt oxide is in charge of reversible redox reactions and intercalation pseudocapacitance because protons from the PVA/H2SO4 electrolyte intercalate into the structure of CoO, while polypyrrole, as a conductive matrix, offers rapid electron transport and continuous charge storage through surface redox reactions.[145] Even while conducting polymers and metal oxides have promising properties, there are still issues that need to be resolved.[148] For example, relatively low mechanical stability of conducting polymers and the poor cycle performance might create a limitation for its practical application. Additionally, poor electrical conductivity of metal oxide and its possible structural deterioration during cycling may reduce their effectiveness. By coupling the high-capacitance characteristics of CoO with the conductive network of PPy, the PPy-CoO composite material minimizes the negative side effects and produces a composite with improved mechanical flexibility, stability, and electrochemical performance. Furthermore, micro-supercapacitors made by PPy-CoO composites offer effective energy storage options in a small form factor and may be incorporated into a variety of electrical products due to their quick charge and discharge rates. Thus, there is enormous potential to advance energy storage technology by creating PPy-CoO MPCs.

6.3.2 Experimental sections

6.3.2.1 Electrochemical Measurement

Cyclic voltammetry (CV), galvanostatic charge/discharge (GCD), and electrochemical impedance spectroscopy (EIS) techniques were used to investigate the electrochemical performance of MPCs. All the tests were carried out with PalmSens4 potentiostat/galvanostat (100 mA, 10 V) equipped with PS Trace 5.10 software. The CV characterizations were carried out within the potential window of 0-1 V with scan rates ranging from 5-1000 mV/s, while GCD measures were performed with current density ranging from 0.1-1.5 mA/cm^2. EIS was performed at a frequency range of 200 kHz to 0.1 Hz with a 10 mV voltage amplitude.

The actual capacitance of the device was calculated according to the following equations:

From CV curves[126]

$$C = \frac{\int i\, dV}{2 \times \vartheta \times \Delta V} \quad (3)$$

From charge-discharge curves

$$C = \frac{I \times \Delta t}{\Delta V} \quad (4)$$

Where $\int i\, dV$ is the area of the CV curve, ϑ is the scan rate, ΔV is the voltage window, I is the current used for charging and discharging, and Δt is the discharge time.

The energy density (E) and power density (P) of the device were calculated using the following equations:[152,153]

$$E = \frac{C}{2 \times 3600} \quad (5)$$

$$P = \frac{3600 \times E \times \vartheta}{V} = \frac{3600 \times E}{\Delta t} \quad (6)$$

The devices' capacitance retention has been evaluated as the ratio of the specific areal capacitance at each cycle to the specific areal capacitance achieved in the first one, over 10,000 cycles at 1 mA/cm^2.

6.3.3 Results and discussion

6.3.3.1 Physical characterization.

SEM and TEM techniques investigated the morphology and microstructure of the synthesized 3D PPy-CoO soft gels. The porous nature of the materials is demonstrated in Figure 6.22(a), while the presence of the cobalt oxide nanoparticles in the polymer matrix was proved by the EDS technique. (Figure 6.22b,c) Elements mapping indicated the presence of Cobalt within the polymer matrix. The TEM image, shown in Figure 6.23a, shows the presence of cobalt oxide nanoparticles in the material.

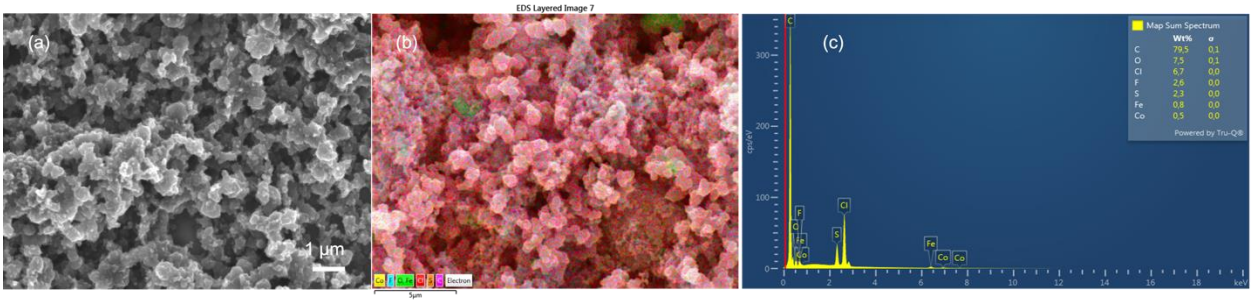

Figure 6.22. (a) SEM image of PPy-CoO gel morphology, (b) EDS mapping, (c) Elemental mapping of the PPy-CoO indicating the presence of cobalt oxide in the polymer matrix.

Fourier transform infrared (FT-IR), Raman spectroscopy, and X-ray diffraction (XRD) analyses have been carried out to confirm the structural features of the materials further. The IR spectra of the pure 3D PPy and 3D PPy-CoO soft gels are shown in Figure 6.24b. The peaks at 1547 cm-1 and 1456 cm^{-1} correspond to the C=C/C-C stretching vibrations in the fundamental polypyrrole ring, which are essential for the electrical conductivity of the PPy; the ones at 1235 and 1359 cm^{-1} indicate the C-N stretching vibration[46], while the peak at 1030 cm^{-1} reveals the characteristic adsorption peak of the O=S=O stretching, which indicates the p-TSA dopant in the PPy.[154] The 775 and 889 cm^{-1} peaks are associated with out-of-plane C-H and =C-H bending vibrations. The shift of the in-plane bending of the C-H bond in the 3D PPy-CoO IR spectra to 956 cm^{-1} indicates the dynamic response to the metal oxide within the composite structure. Another significant spectral shift is identified in the peak associated with C=C stretching vibrations of the PPy ring to 1630 cm^{-1}, which indicates the interaction between PPy and CoO.[145] Such shifts represent the structural rearrangements signifying the integration of cobalt oxide nanoparticles with polypyrrole matrix.

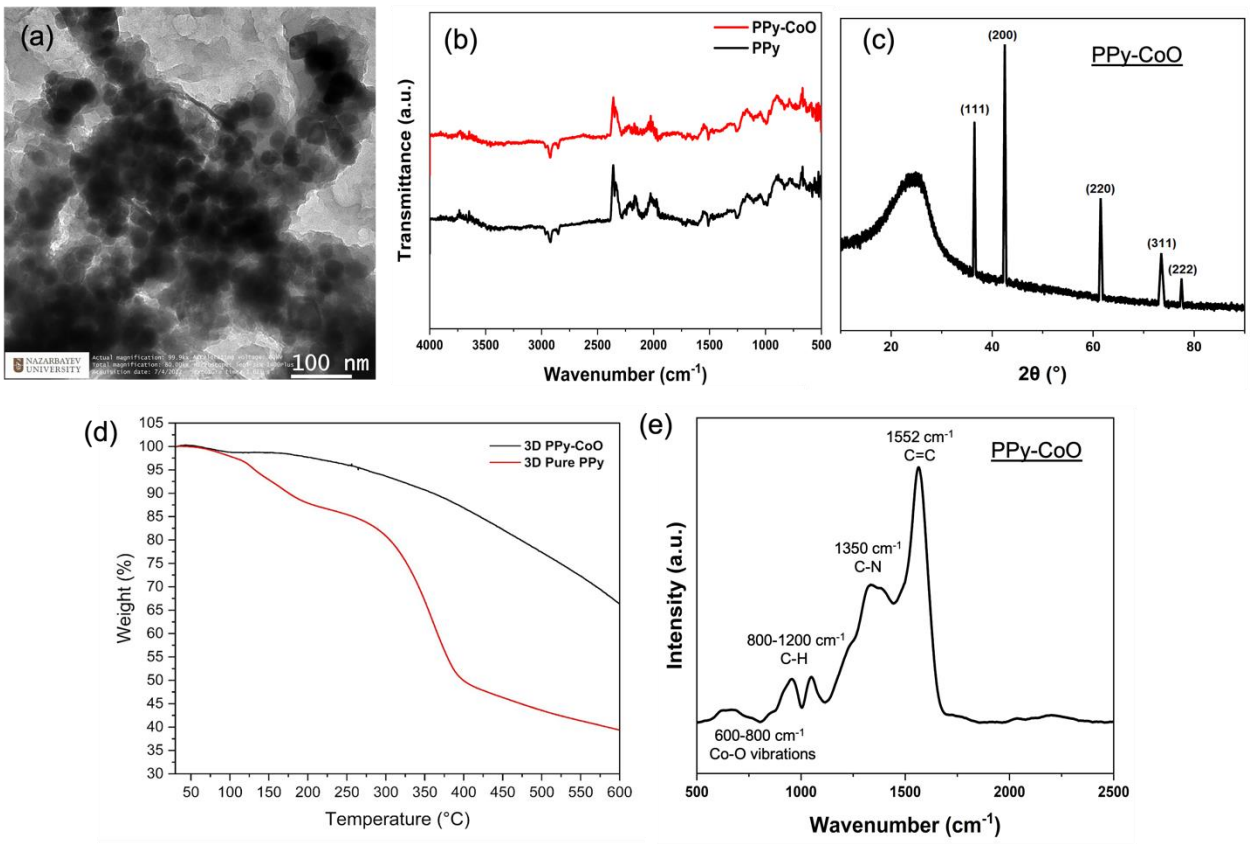

Figure 6.23. A) TEM image of PPy-CoO 1.0 wt% gel; B) FT-IR spectra of pure PPy and PPy-CoO 1.0 wt% gels; C) XRD spectra of PPy-CoO 1.0 wt% gel; D) TGA curves of Pure PPy and PPy-CoO 1.0 wt%; E) Raman spectra of PPy-CoO 1.0 wt%.

The obtained XRD spectra show the peaks corresponding to the crystalline plane of Cobalt (II) oxide interspersed with broader features indicative of polypyrrole amorphous or semi-crystalline nature. (Figure 6.24c) The sharp, narrow diffraction peaks at 2θ values of approximately 36.5°, 42.5°, 61.5°, 74.5°, and 78.5° correspond to the (111), (200), (220), (311), and (222) planes of cobalt oxide (CoO), respectively. These peaks confirm the presence of crystalline CoO with a relatively large crystal size within the composite and agree with standard crystallographic data for cubic CoO.[121,144,145] The combination of the broad polypyrrole feature and distinct crystalline peaks of cobalt oxide confirms that the cobalt oxide maintains its crystalline structure within the composite, which is essential for its catalytic and electronic applications.

The thermal and mechanical stability of polypyrrole composites were investigated by thermogravimetric analysis (TGA). The TGA data proves that the presence of cobalt oxide in the 3D polypyrrole matrix significantly improves the thermal stability of the polymer (Figure 6.24d).

The superior thermal stability of the 3D PPy-CoO composite compared to pure 3D PPy can be attributed to several factors, such as the thermal barrier effect due to cobalt oxide particles, which delay the thermal degradation of the polypyrrole matrix, and the stabilization of polymer chains due to the interaction of polypyrrole with cobalt oxide and the formation of protective layers, which result in higher resistance to thermal decomposition. Based on the comparative data of the weight percentage against temperatures up to 600 °C, several vital observations have been made:

1. Initial weight loss (50–150°C):

Both samples exhibit a minor weight loss at this temperature range, likely due to the evaporation of the residual moisture content and volatile impurities. The composite (black curve) shows better moisture absorption resistance than the pure polypyrrole.

2. Main decomposition (150–500 °C):

The 3D PPy-CoO shows a more gradual and delayed thermal decomposition at this stage than pure polypyrrole, which exhibited significant weight loss at around 300–400 °C. This weight loss of PPy can be attributed to the thermal degradation of the polypyrrole backbone, which involves breaking polymer chains.

3. Residual weight loss (500–600 °C):

At higher temperatures, the weight loss continues for both samples; however, the composite material retains a higher percentage of its original weight than pristine polypyrrole. 3D PPy-CoO shows only 30% weight loss at 600 °C, while pure PPy shows two times lower results as 60% weight loss at the same temperature.

Raman spectroscopy was carried out to understand the structural features of fabricated composite material. According to the obtained spectrum, a strong peak at 1500 cm^{-1} indicates the C=C stretching mode in the polypyrrole backbone and is a typical signature of aromatic rings in a conjugated polymer. The presence of cobalt oxide in the polymer composite with Co-O stretching vibrations can be seen by peaks in the range of 500 cm^{-1} to 700 cm^{-1}. Overlapping peaks at 500 cm^{-1} to 1000 cm^{-1} are attributed to stretching modes of ppy rings and C-H in-plane vibrations. Additionally, peaks at 1200 cm^{-1} to 1400 cm^{-1} correspond to C-N stretching and C-H bending modes in polymer structure. The clear and distinguishable peaks suggest good dispersion and interaction between the polypyrrole and cobalt oxide in the composite.

6.3.4 Micro-Pseudocapacitor (MPC) design.

A flexible micro-supercapacitor was fabricated by using PET as a substrate, a Cr/Au layer of the current collector, a PPy-CoO electrode cast by a doctor blade, and a gel PVA/H_2SO_4 electrolyte. The digital illustration of the MSC design is shown in Figure 6.24A. The graphical illustration of a single MSC with dimensions and an actual image of an MSC with electrolytes are demonstrated in Figures 6.24B and C. The flexible nature of the fabricated micro-supercapacitor is demonstrated in Figure 6.24D. SEM observed the surface morphology of the electrode, and images revealed that the continuously porous polymer gel inherited the continuously porous nature of electrode material and EDS elemental mapping revealed the presence of CoO NPs. (Figure 6.24 H,I) The thickness of the cast electrode was 30 µm. (Figure 6.24G) The width of the electrode interdigit was 450 µm, the interspace was 300-350 µm, and the thickness of the cast electrode was 30-35 µm.(Figure 6.24F)

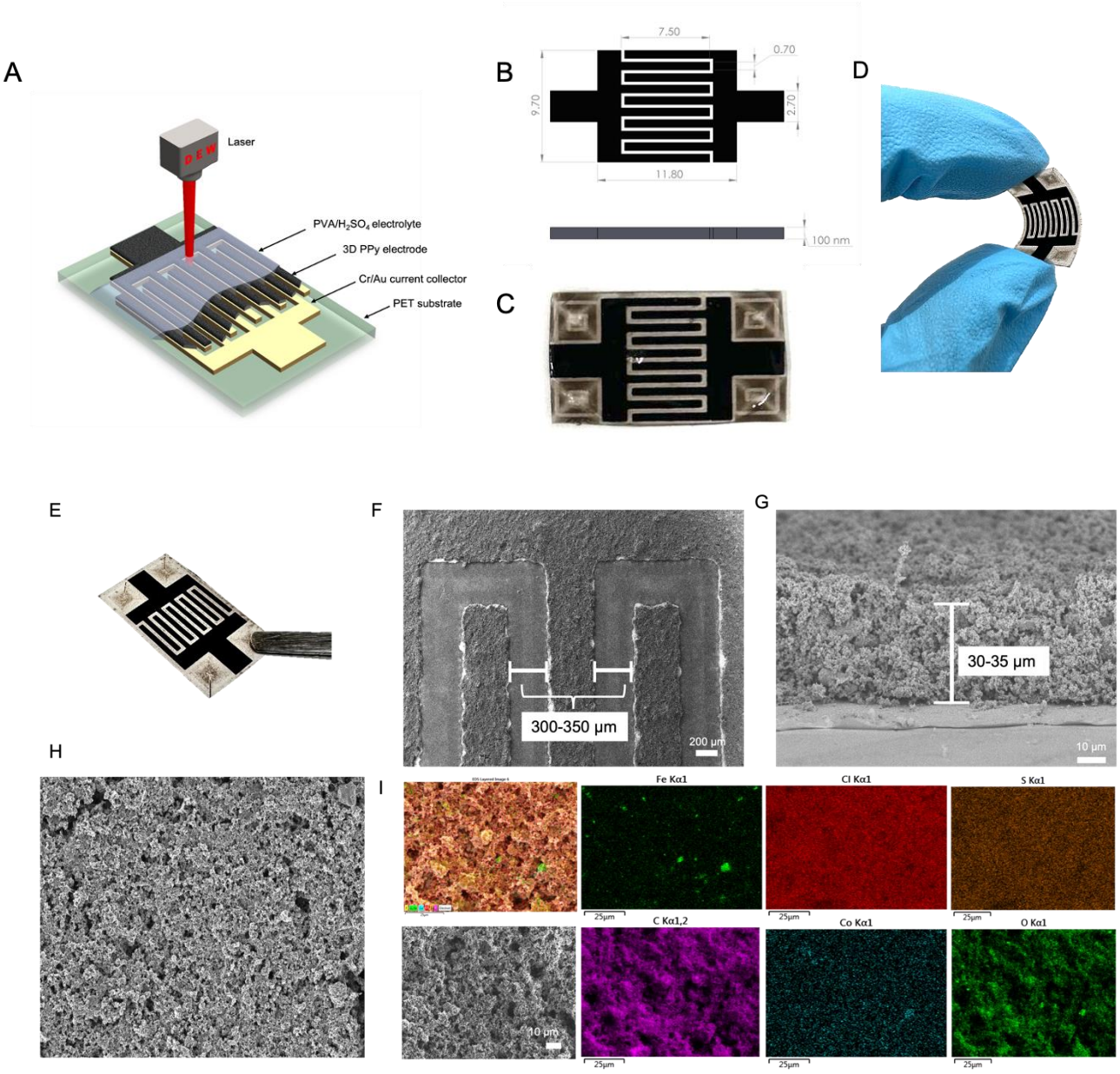

Figure 6.24. A) The digital illustration of MPC design; B,E) Single MPC design with dimensions; C) Real image of MPC covered with electrolyte; D) Flexible behavior of fabricated MPC. F) SEM images of PPy-CoO electrode with the evident continuously porous nature even after casting. G) The cross-section of the electrode. H) SEM image of PPy-CoO electrode's surface. I) EDS Elemental mapping of electrode.

6.3.5 Electrochemical Performance of MPCs.

To study the electrochemical activity of solid 3D PPy-CoO micro-supercapacitor, the electrochemical experiments were carried out by a two-electrode system using PVA/H_2SO_4 gel electrolyte. For the electrochemical studies, we used three composite materials with different concentrations of CoO: 0.5wt%, 1.0wt%, and 3.0wt%. According to the obtained results, the best capacitance was obtained by a sample with 1.0 wt% of CoO NPs. The rest of the measurements were done using this ratio. The CV curves are shown in Figure 6.25. The reduced porosity of the polymer can explain this due to the excess of nanoparticles of the polymer matrix and the overloading of pores with them in the case of 3.0 wt%. While at 0.5wt%, there was still room for nanoparticles, and it could have achieved better performance. So, further results will be presented by MPCs fabricated with PPy-CoO 1.0 wt.% sample.

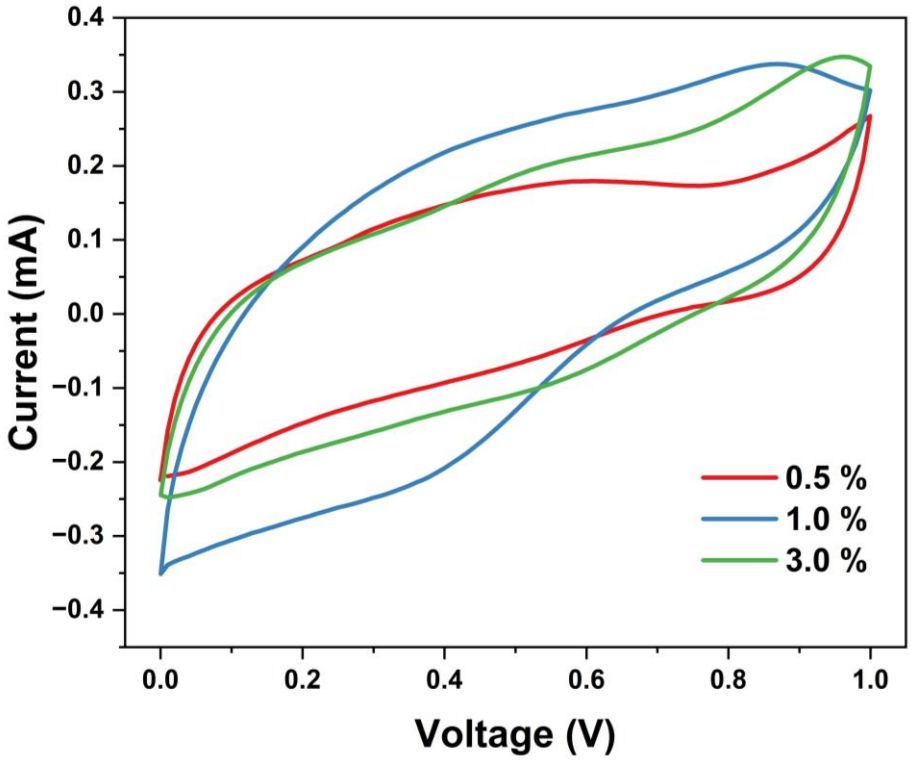

Figure 6.25 CV profiles of PPy-CoO MPCs with 0.5 wt%, 1.0 wt%, and 3.0 wt% concentrations of CoO NPs.

The areal capacitance of the pure PPy electrode at a scan rate of 5 mV s^{-1} was 9.2 mF cm^{-2}, with energy and power densities of 1.28 μWh cm^{-2} and 22.99 μW cm^{-2}, respectively. (Figure 6.26A, B) Conversely, although there was a notable increase in capacitance and energy storage characteristics, the PPy-CoO composite exhibited CV curves with more pronounced profiles. At a

rate of 5 mV s^{-1}, the areal capacitance rose to 30.39 mF cm^{-2}. The energy and power densities attained were 4.22 μWh cm^{-2} and 75.97 μW cm^{-2}, almost 3.5 times more than the values of the pure PPy electrode. (Figure 6.26 C,D) The increased capacitance results from the improved charge storage capacity provided by cobalt oxide via its localized $Co^{2+/}Co^{3+}$ reversible redox processes within a more specific voltage range. CoO initiates Faradaic reactions, enabled by the intercalation and deintercalation of protons (H^+) during the charging and discharging processes inside the electrode material: The redox processes increase the pseudocapacitive behavior and improve the total capacitance and energy storage of the PPy-CoO device.

The narrowed CV curve of PPy-CoO in comparison to pure PPy indicates a transition in charge storage processes from surface-oriented redox reactions to intercalation pseudocapacitance. The decreased electrolyte accessibility and the increased reversibility of CoO's redox reactions result in the more pronounced, narrower peaks in the composite's CV curve. This indicates that the synergistic interaction between PPy and CoO enhances electron transport while minimizing unnecessary redox processes, resulting in improved electrochemical stability.

$CoO + H^+ \leftrightarrow Co^{3+} + OH^- + e^-$ Oxidation Co^{2+} to Co^{3+}

$Co^{3+} + OH^- + e^- \leftrightarrow CoO + H^+$ Reduction Co^{3+} to Co^{2+}

The comprehensive summary of all electrochemical measurements is provided in Tables 6.3 and 6.4. The EIS map of PPy-CoO MPC illustrates the impedance properties of the device, with a reduced semi-circle signifying low charge transfer resistance and effective charge transfer at the electrode-electrolyte interface. The enhanced vertical line at low frequencies indicates superior ion diffusion and capacitance relative to pure PPy MPC. The inclined line at intermediate frequencies signifies the diffusion-controlled mechanism that facilitates effective ion diffusion into the porous structure of the electrode. The 3D PPy-CoO MPC exhibits reduced charge transfer resistance and enhanced ion diffusion compared to pure PPy, as seen by the semicircle in the Nyquist plot. The use of CoO improves electrochemical performance, particularly at reduced currents, owing to enhanced pseudocapacitive behavior and accelerated charge transfer. Pure PPy demonstrates elevated resistance, which constrains its capacitance and charge-discharge efficiency. The improved electrochemical performance of the PPy-CoO composite can be attributed to the synergistic interaction between PPy and CoO. Polypyrrole serves as a conductive matrix,

facilitating fast electron transport and sustained charge storage via surface redox processes. Cobalt oxide facilitates reversible redox reactions and intercalation pseudocapacitance as protons from the PVA/H_2SO_4 electrolyte intercalate into the CoO structure. Although the CV curves of the PPy-CoO electrode are constricted, the enhancement in capacitance and energy density is attributable to these localized redox processes.

Table 6.3. Electrochemical activity performance of 3D PPy and 3D PPy-CoO MPCs.

	Pure PPy MPC	**PPy-CoO MPC**		**Pure PPy MPC**	**PPy-CoO MPC**
Cyclic voltammetry					
Areal Capacitance at **5mV/s**	9.20 mF/cm2	30.4 mF/cm2	Areal Capacitance at **200 mV/s**	2.28 mF/cm2	2.42 mF/cm2
Energy Density at **5 mV/s**	1.28 µWh/cm2	4.22 µWh/cm2	Energy Density at **200 mV/s**	0.317 µWh/cm2	0.336 µWh/cm2
Power Density at **5 mV/s**	22.99 µW/cm2	75.97 µW/cm2	Power Density at **200mV/s**	228.34 µW/cm2	242.11 µW/cm2

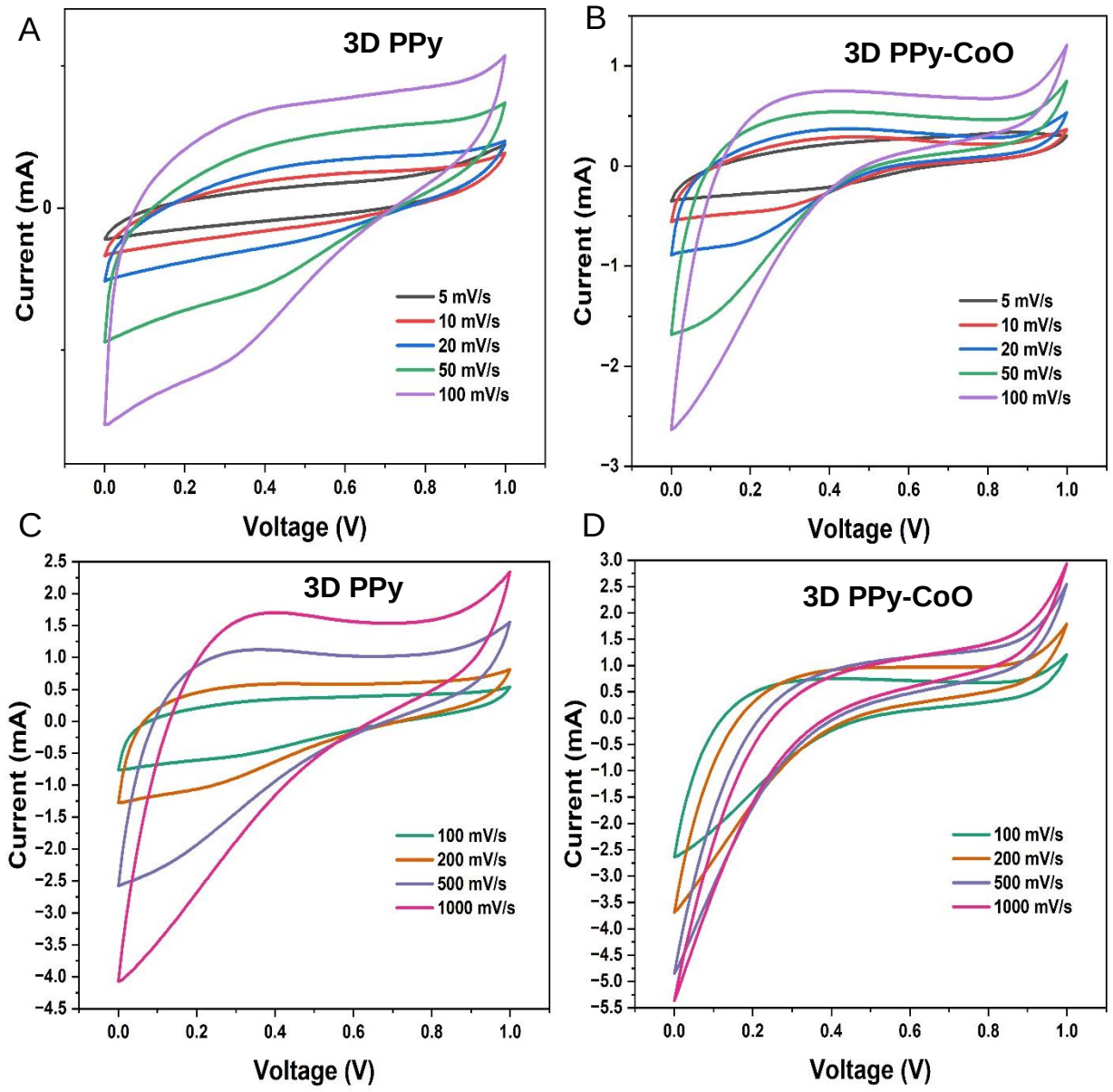

Figure 6.26. Cyclic Voltammetry (CV) curves at various scan rates (5 mV s^{-1} to 1000 mV s^{-1}) for 3D PPy and 3D PPy-CoO MPCs.

The fabricated device also demonstrates excellent cycling stability, retaining 80% of its initial capacitance after 10,000 cycles at a current density of 1 mA cm^{-2} (Figure 6.27 D, E). The initial capacitance decline in PPy-CoO MPC might be due to structural modifications during contact with the electrolyte and its penetration, causing slight volumetric changes. The rapid deterioration between 2000 and 6000 cycles may indicate mechanical degradation, leading to the loss of ion

transport routes and electroactive sites. Beyond 6000 cycles, a stabilization phase occurs as the residual polymer matrix becomes denser and more stable, allowing for ion transport and redox processes, resulting in stable capacitance. This long-term reliability and durability make the micro-supercapacitor a promising candidate for compact, low-power applications such as wearable electronics, sensors, and microelectromechanical systems (MEMS).

Table 6.4. Galvanostatic charge-discharge data for PPy and PPy-CoO MPCs.

	Pure PPy MPC	**PPy-CoO MPC**
GCD		
Areal Capacitance at **0.2 mA/cm2**	7.48 mF/cm^2	30.56 mF/cm^2
Energy Density at **0.2 mA/cm2**	1.039 $\mu Wh/cm^2$	4.24 $\mu Wh/cm^2$

The charge-discharge curves of PPy MPC are nearly triangular at lower current densities, indicating capacitive behavior. (Figure 6.27A) However, at higher current densities, the curves become more distorted, indicating the limitations of ion transport and the material's ability to sustain high currents. Shorter charge-discharge times at higher current densities indicate lower capacitance. PPy-CoO MPC, on the other hand, shows more linear segments, suggesting better capacitive behavior even at higher current densities. (Figure 6.27B) The device sustains higher currents better than pure PPy, with longer charge-discharge times indicating higher capacitance and better performance under high currents. The energy density of PPy-CoO MPC is about four times higher than pure PPy MPC, making it more suitable for applications requiring higher energy storage. (Table 6.4) EIS plots show the impedance characteristics of the supercapacitors, with a semi-circle at high frequencies indicating charge transfer resistance and diffusion limitations at low frequencies. The smaller semi-circle of 3D PPy-CoO MPC indicates efficient charge transfer at the electrode-electrolyte interface, while the more vertical line at low frequencies suggests improved capacitive performance. (Figure 6.27 C and F)

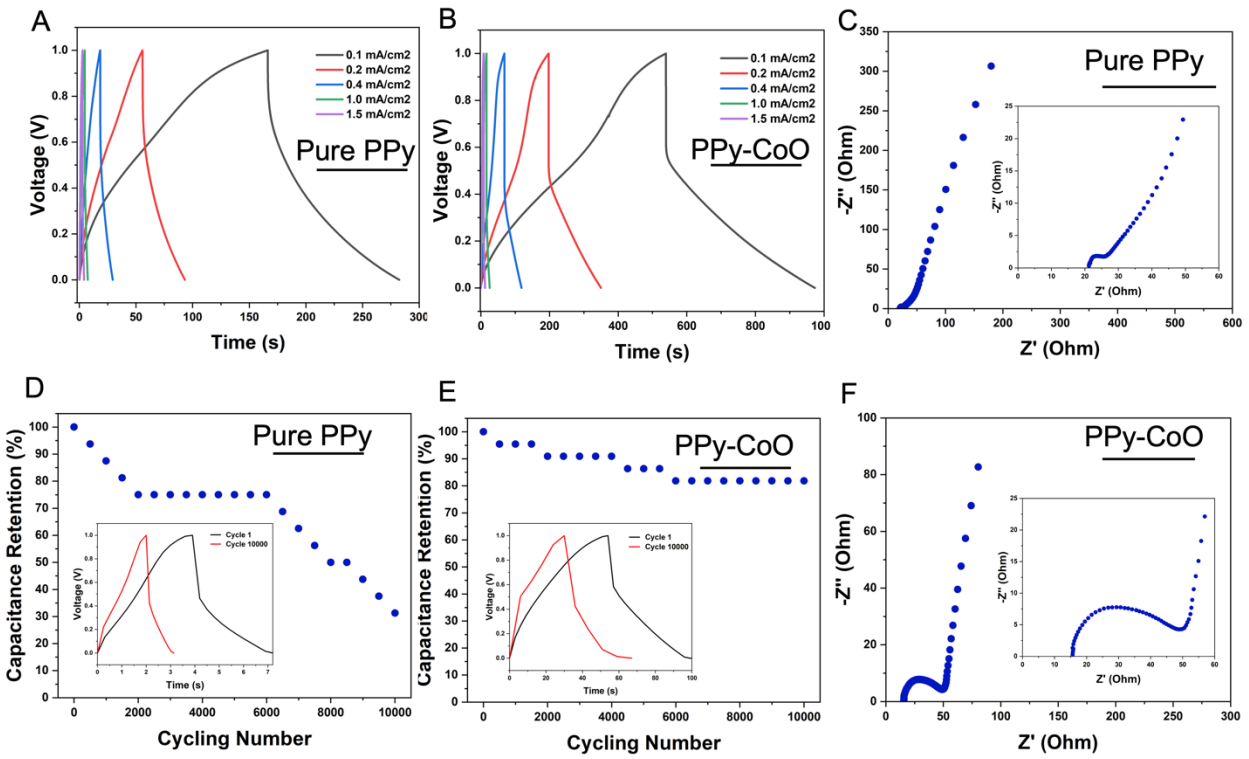

Figure 6.27. Galvanostatic Charge-Discharge (GCD) Curves: A) 3D PPy MPC; B) 3D PPy-CoO MPC; C) Electrochemical Impedance Spectroscopy (EIS): C) 3D PPy MPC; F) 3D PPy-CoO MPC. D) Capacitance retention graphs of fabricated 3D PPy MPC after 10 , 0 cycles at 1 mA/cm^{2,} and E) Capacitance retention of 3D PPy-CoO MPC after 10,000 cycles at 1 mA/cm^2.

The integrability of the prepared MPC was analyzed by fabricating the parallel and in-series connected circuits. (Figure 6.28)

The CV curve for a single supercapacitor is rectangular, indicating good capacitive behavior. Its current moderate response indicates a single device's charge storage capacity. The series configuration has a broader potential window, twice the single devices. The current response is lower in series connections, reducing overall capacitance. The parallel configuration shows a higher current response, indicating increased overall capacitance. The potential window remains the same as the single device, but the parallel configuration effectively increases charge storage capacity.

The GCD curve for a single supercapacitor reveals a triangular shape, indicating capacitive behavior. The series configuration has a broader voltage range reaching 2V, indicating a series combination of two devices. The parallel configuration has shorter charge-discharge times,

indicating lower capacitance but higher operating voltage. The voltage range remains the same as the single device, but the increased charge-discharge time confirms enhanced charge storage capacity. Combining supercapacitors in series and parallel configurations significantly impacts their performance characteristics.

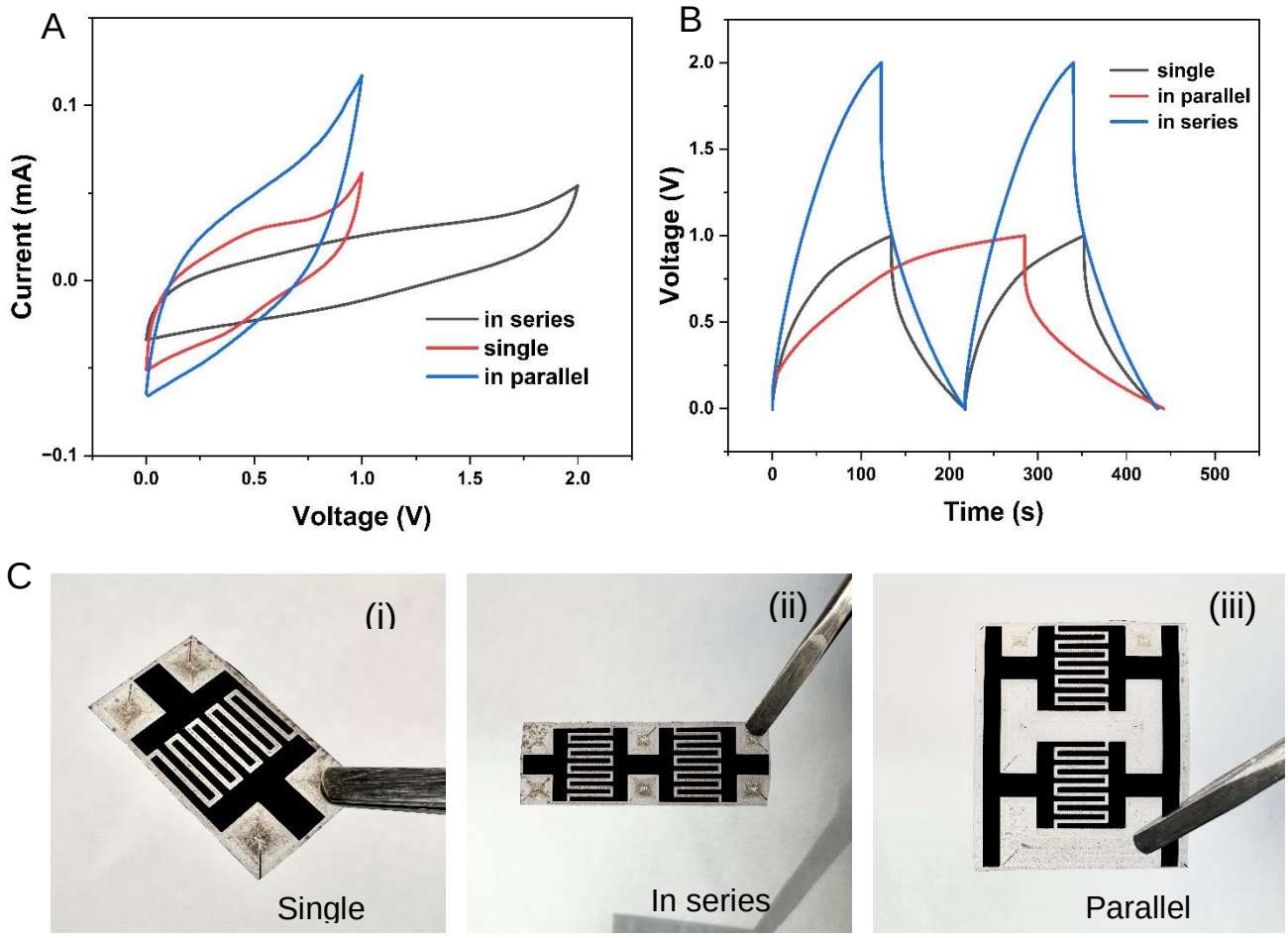

Figure 6.28. Electrochemical performance of integrated MPCs circuits A) CV and B) GCD. C) Real images of single, in-series, parallel circuit connections.

Table 6.5. A summary of MPC based on polypyrrole with main characteristic properties.

Electrode material	Electrolyte	**Area capacitance**	**Energy density**	**Power density**	**Cycle-life**	**Reference**
PPy@Ag (2023)	PVA/H3PO4	90 mF cm^{-2} /0.5 mA cm^{-2}	12.5 µWh cm^{-2} at 0.25 mW cm− 2	2.6 mW cm^{-2} 8.05 µWh cm− 2	109% after 10000 cycles	155
PPy-CNT@rGO (2023)	PVA/H3PO4	65. mF cm^{-2} / 0.1 mA cm^{-2}	5.9 µWh cm− 2	(0.4 mW cm− 2	79% capacitance after 10,000 cycles at 5 mA cm−2	156
Polypyrrole and cotton fabric (2022)	PVA/H2SO4	2.64 mF/cm2/ at 0.08 mA/cm2,	0.09µWh/cm2	19.1µW/cm2 0.0191 mW	85% after 3000 cycles	157
LIG-PPy (2022)	Acetonitrile/ water-in-salt	124 mF cm− 2	99.2 µWh cm− 2	47.75 mW cm− 2	84% as after 10,000 cycles	158
PPy-hs@CoS (2022)	KOH	40.3 mF/cm2 at 0.3 mA/cm2	4.67 mWh/cm2 at 0.125 W/cm3	0.83 W/cm2 at 3.17 mWh/cm3		143
Zn@PPy (2021)	NaCl/agarose	2.84 mF/cm2	0.4 µWh cm−2) 3.4µWcm−2	0.39 mW/cm2 at 0.0064µWhcm−		159
Nickelnanocone arrays (NNAs) and polypyrrole nanotubes (PPyNTs) (2021)	PVA/H3PO4	60.2 mF cm−2 at 0.16 mA cm−2	5.35µWh cm−2 at 63.9µWcm−2	2 mW cm−2 at 1.7µWh cm−2	84.3% after 5000 cycle	160
Dual-Mesoporous Polypyrrole/ Graphene Nanosheets (2020)	PVA/H2SO4	38 mF cm−2 1 mV s−1	volumetric energy density of 2.5 mWh cm−3	Volumetric of 397 mW cm−3 at energy density of 0.9 mWh cm−3	82% after 4500 cycles	161
MnO2/PPy (2020)	LiClO4/ PVA	13 mF cm^{-2} / 0.1 mA cm^{-2}	1.07 µW cm^{-2}	0.53 mW cm^{-2}	84% of the initial capacitance after 5000 CV cycles at a scan rate of 500 mV s-1	147
Ag@PPy NC (2017)	PVA/H3PO4	47.5 mF cm−2 at 60 µA cm−2	4.33 µWh cm−2 at 0.02597 mW cm−2	0.6 mW cm−2at an energy density of 0.00267 mW h cm−2	77.6% after 1000 bending cycles 82.6% after 10000	162

PPy-coated SiNTr (2015)	PYR13TFSI aprotic ionic liquid	14 mF cm2 0.1 mA cm^{-2}	4.17 µWh cm−2	0.8 mW cm2	30% after 10 000	[163]
PPy_CoO	PVA/H2SO4	**30.56 mF cm^{-2} at 0.2 mA cm^{-2}**	**4.24 µWh cm− 2**	**75.97 µW/cm2 0.07597 mW/cm2**	**80% after 10 000 cycles at 1mA/cm2.**	**This work**

CONCLUSION

We successfully synthesized 3D continuously porous PPy-CoO composite material with exceptional electrochemical activity for energy storage applications.

The study of PPy-CoO micro-pseudocapacitors (MSPs) has shown significant improvements in electrochemical performance compared to pure PPy MPCs. Improved areal capacitance, energy density, power density, and cycle stability are seen in the composite MPCs that consist of polypyrrole (PPy) and cobalt oxide (CoO). With an impressive areal capacitance of 30.56 mF cm^{-2} at 0.2 mA cm^{-2}, the PPy-CoO MPCs display an impressive ability to store a significant amount of charge. Their energy density of 4.24 µWh cm^{-2} is modest, which makes them appropriate for small-scale uses. The power density of the composite MPCs is 75.97 µW cm^{-2}, which is three times more than that of the pure PPy MPCs. They are dependable and long-lasting because, even after 10,000 cycles, 80% of their original capacitance is still there. Microelectromechanical systems, sensors, wearable electronics, and other small, power-efficient devices may benefit from the PPy-CoO MPCs. Improving the composite's CoO content and finding ways to scale up manufacturing might be areas of future study.

6.4 3D continuously porous PPy-Gr Network for an Ultra-Sensitive and Flexible Hydrogen Gas Sensor at Room Temperature

6.4.1 Introduction

Hydrogen (H_2) is considered a next-generation energy source with diverse applications across valuable social, economic, and industrial sectors, including transportation, biomedical, power generation, and space exploration.[164] The anticipated increase in production and utilization of hydrogen gas necessitates the development of new safe technologies for its production, storage, and transportation due to its low ignition energy and wide flammable range.[165,166] Moreover, the gas's low molecular weight and colorless and odorless properties lead to easy leaks, potentially

causing rapid explosions. Consequently, developing an ultrasensitive, lightweight, portable, and flexible hydrogen sensor to detect early gas leaks and mitigate environmental and economic consequences is extremely important.

An effective method involves the utilization of chemical sensors to identify and notify us of hazardous contaminants. These sensors can function as preemptive alert systems, allowing for proactive actions to mitigate pollutants and safeguard human well-being and the ecosystem. These sensors' advanced gas-sensing performance has opened a wide range of applications. The main advantages of chemical gas sensors (CGSs) lie in their sensing materials, which demonstrate higher sensitivity to lower gas concentrations and offer cost-effective fabrication methods compared to conventional sensing materials.[167,168] Unlike traditional two-dimensional (2D) materials that suffer from high operating temperatures, limited selectivity, chemical degradation, and lower cycling stability, nanoporous materials provide significant improvements. These materials have a high surface area, enhanced adsorption and desorption capabilities, and an interconnected porous network, facilitating faster charge carrier transport, resulting in lower detection limits, excellent selectivity, and remarkable response and recovery times.[109,167] Chemical gas sensors (CGSs) are devices that detect and measure the levels of gases by monitoring changes in electrical resistance. The functioning concept of CGSs is based on the interaction between a sensing material and the target analyte. The selection of the sensing material, also known as the receptor, is done with great care to ensure that it demonstrates a visible alteration in electrical conductivity or resistance upon exposure to certain gases. The sensing material's surface is specifically engineered to possess a high surface-to-volume ratio to optimize its interaction with the target analyte. To improve the ability of CGSs to selectively detect and accurately measure target analytes, the surface of the sensing material can be modified with specialized coatings, catalysts, or receptors that have a high affinity for the target analyte.[169,170]

Despite their excellent sensing performances, conventional solid sensors do not meet current demands for gas sensors designed to operate in specialized conditions and be utilized as wearable devices for real-time monitoring. Additionally, certain materials employed in solid gas sensors cannot be adapted to flexible substrates due to their brittleness, rigidity, or synthesis methods. In contrast, conducting polymers (CPs) emerge as exceptional candidates for flexible gas sensors due to their unique structure and electrochemical properties, tunable morphology, and scalable, easy synthetic procedures.[166,170,171] Furthermore, their integration with various nanocomposites as

hybrid materials enhances their multifunctional performance, making them well-suited for desired applications.

Here, we present a flexible hydrogen gas sensor based on the conducting polymer polypyrrole (PPy) synthesized by the bicontinuous microemulsion polymerization method. This one-step scalable synthetic procedure enables the design of 0D, 2D, and 3D conducting polymers and their nanocomposites with tunable morphological and electrical properties. The unique, multi-layered oil-to-water nature of the bicontinuous microemulsion allows the fabrication of pure mesoporous 3D conducting polymers and their composites without the addition of any crosslinkers, exhibiting excellent electrical properties. The 3D pure porous polymer network acts as a monolithic conducting framework that facilitates electron and ion transport and promotes the diffusion of molecules and ions more efficiently than 1D or 2D structures. The soft and porous nature of the polymer improves the interaction and adsorption of target gas molecules and sensing material by increasing the number of active sites.

This study supports the hypothesis that the 3D PPy-graphene flexible network synthesized by the bicontinuous microemulsion method exhibits a notable response to 0.05 ppm of H2 gas. Pure graphene is not highly sensitive to hydrogen gas, but its sensitivity can be enhanced through modifications and by using it as a composite or hybrid sensor material component. These modifications and combinations exploit graphene's high surface area, electrical conductivity, and charge transfer capabilities, making it a valuable material in developing advanced hydrogen gas sensors.

Pure Polypyrrole Film (PPy) can detect hydrogen gas through adsorption and subsequent interaction with the polymer matrix. This adsorption can cause changes in charge carrier distribution, electrical conductivity, swelling effect, and sensitivity to humidity and temperature. Graphene in the PPy matrix introduces additional mechanisms to enhance hydrogen gas sensing, such as increased surface area, enhanced electron mobility, improved baseline stability and sensitivity, synergistic effects, and physical and chemical interactions. At room temperature, the fabricated sensor displayed response and recovery times of about 60 seconds. No study has explored the application of 3D pure conducting polymers and their nanocomposites for hydrogen gas sensors using the bicontinuous microemulsion polymerization method, yielding such exceptional sensing results.

Gas sensing tests were conducted at room temperature using a gas sensor test setup comprising a gas chamber, gas pumps, a parameter analyzer, and gas cylinders. The target gas for the tests was hydrogen (H_2), and selectivity measurements were also performed for carbon dioxide (CO_2) and nitrogen dioxide (NO_2)

6.4.2 Results and Discussion

6.4.2.1 Physical characterization

The surface morphology of the PPy-Gr electrode is demonstrated by SEM images in Figure 6.29A. The polymer composite's continuously porous nature remains consistent in the fabricated electrode. This high surface area is essential for further better adsorption and desorption processes during sensing measurements. The structural characteristics of synthesized composites were analyzed using X-ray diffraction (XRD) analysis. (Figure 6.29B) The XRD patterns reveal significant crystallinity and phase composition differences between the two samples. The broad peak observed in pure PPy indicates its amorphous nature, which is typical for conducting polymers. The lack of sharp peaks suggests that the polymer chains are not arranged in a regular, crystalline manner. In contrast, the XRD pattern of the PPy-Gr composite displays a distinct sharp peak at 2θ=26°, corresponding to the (002) plane of graphene. This indicates that the graphene sheets retain their crystalline structure within the composite, which can significantly influence the material's overall properties. The presence of graphene in the composite enhances crystallinity and introduces additional structural order, as evidenced by the sharp diffraction peak.

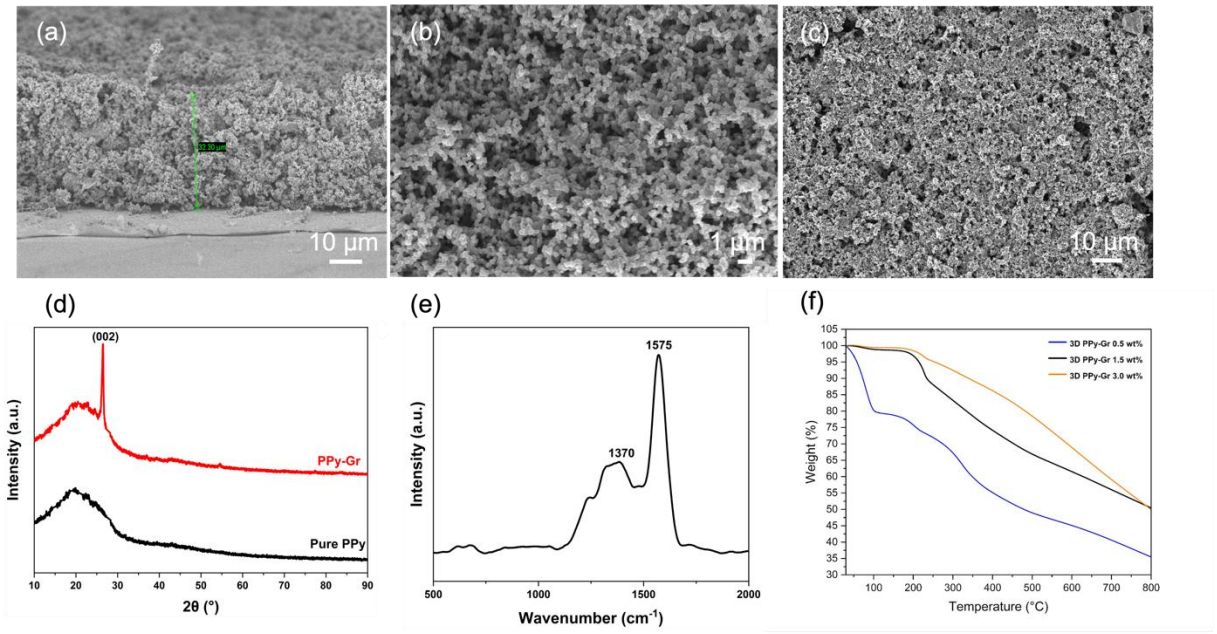

Figure 6.29. A) SEM images of morphology of PPy-Gr electrode. B) XRD spectra of Pure PPy and PPy-Gr; C) Raman spectrum of PPy-Gr composite; D) TGA curves of composite material with different graphene concentrations.

The Raman spectrum of a composite containing polypyrrole and graphene reveals the presence of two distinct bands. (Figure 6.29 C) The first peak, at 1575 cm^{-1}, corresponds to the G-band of graphene, characteristic of the in-plane vibrations of sp2-bonded carbon atoms. This peak indicates the presence of well-ordered graphene within the composite. The second peak, at 1370 cm^{-1}, corresponds to the D-band of graphene, which arises due to the breathing modes of sp2 atoms in rings and requires a defect for activation. This suggests defects or edge sites within the graphene structure, which can be expected in chemically synthesized or processed graphene materials. The broadening of peaks around 1300-1600 cm^{-1} suggests that polypyrrole interacts with the graphene sheets. [172,173] Further, to investigate the thermal stability and degradation characteristics of 3D PPy-Gr composites, TGA analysis was carried out. (Figure 6.29 D) Samples with varying graphene content (0.5 wt%, 1.5 wt%, and 3.0 wt%) were studied. The analysis revealed that the graphene content significantly contributes to the thermal stability of composites. Higher graphene content improves thermal stability, as evidenced by higher residual weights and delayed decomposition. The 3.0 wt% PPy-Gr composite exhibits the highest residual weight at 800°C, indicating superior thermal stability. This can be attributed to the excellent thermal stability and reinforcing effect of graphene, which delays the thermal decomposition of the polypyrrole matrix. The 0.5 wt% PPy-

Gr composite shows the lowest residual weight, suggesting lower thermal stability than the composites with higher graphene content. Additionally, the graphene sheets provide a barrier effect, restricting the movement of degradation products.

The surface area study reveals that introducing graphene nanoflakes into the polypyrrole-graphene (PPy-Gr) matrix significantly increases the surface area from 12.4 to 30.2 m^2/g. (Table 6.7) However, with higher graphene content, the surface area decreases to 11 m^2/g and 8 m^2/g, respectively, due to the aggregation of graphene sheets at higher concentrations. The pore volume increases significantly for PPy-Gr 0.5 wt% compared to pure PPy (0.056 cm^3/g), suggesting that adding a small amount of graphene enhances the composite's porosity. (Table 6.6) For higher graphene content, the pore volume decreases to 0.05 cm^3/g and 0.06 cm^3/g, suggesting that excessive graphene might block some pores or lead to a denser material structure.

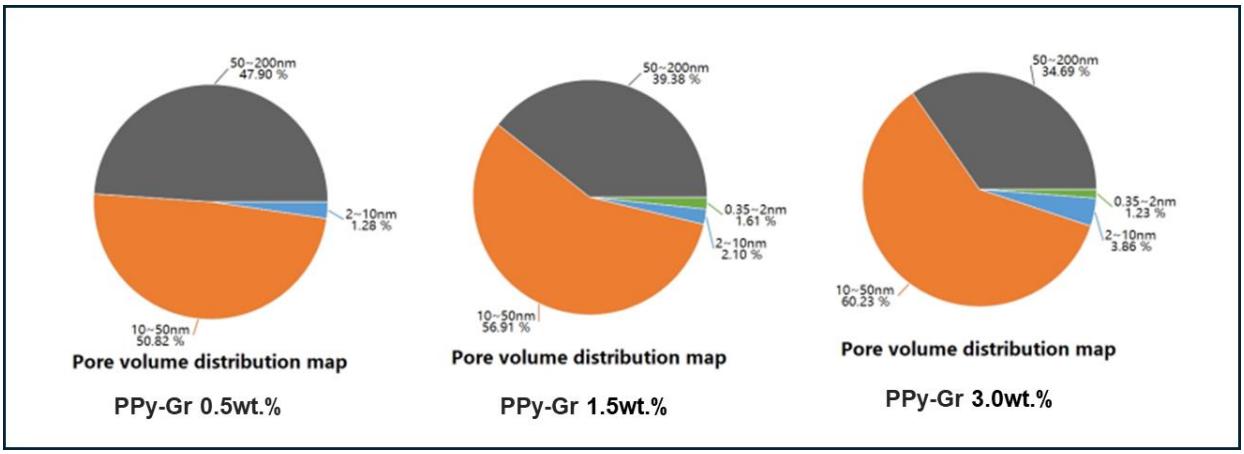

Figure 6.30. Pore volume distribution map for 3D PPy-Gr composites with three graphene content weight percents. (0.5,1.5, and 3.0)

The average pore diameter for pure PPy is 5.4 nm, which drastically increases to 57.3 nm for PPy-Gr 0.5 wt%, suggesting the formation of larger pores due to the introduction of graphene. (Figure 6.30) The large pores and high surface area in PPy-Gr 0.5 wt% might make the material more suitable for applications requiring high surface interaction, such as supercapacitors and sensors. However, the reduced surface area and pore volume at higher graphene contents suggest a denser structure, which might enhance mechanical stability but at the cost of reduced electrochemical activity.

Table 6.6. Pore distribution analysis of PPy-Gr composite with different concentrations.

Pore volume distribution	**Micro**	**Meso**		**Large**
Pore size	0.35-2 nm	2-10 nm	10-50 nm	50-200 nm
PPy-Gr 0.5wt%	0%	1.28%	50.82%	47.90%
PPy-Gr 1.5wt%	1.61%	2.10%	56.91%	39.38%
PPy-Gr 3.0wt%	1.23%	3.86%	60.23%	34.69%

Table 6.7. Surface area analysis results of synthesized materials.

Material	**Surface area (m^2/g)**	**Pore volume (cm^3/g)**	**Average pore diameter (nm)**
Pure PPy	12.4	0.056	5.4
PPy-Gr 0.5wt%	30.2	0.36	57.3
PPy-Gr 1.5wt%	11	0.05	18.4
PPy-Gr 3.0wt%	8	0.06	18.1

6.4.3 Gas sensing analysis

Figure 6.31 demonstrates the flexible 3D PPy-Gr gas sensor chip. The sensor's compact design, featuring metallic contacts for easy connection to external circuits, demonstrates its potential for integration into various electronic systems. The sensor's flexibility suits wearable technology and flexible electronics, such as environmental monitoring on curved surfaces or integration into smart textiles. The sensor's innovative sensing material maximizes interaction with gas molecules through a high surface-to-volume ratio, enhancing sensitivity and selectivity and allowing it to detect low concentrations of gases effectively.

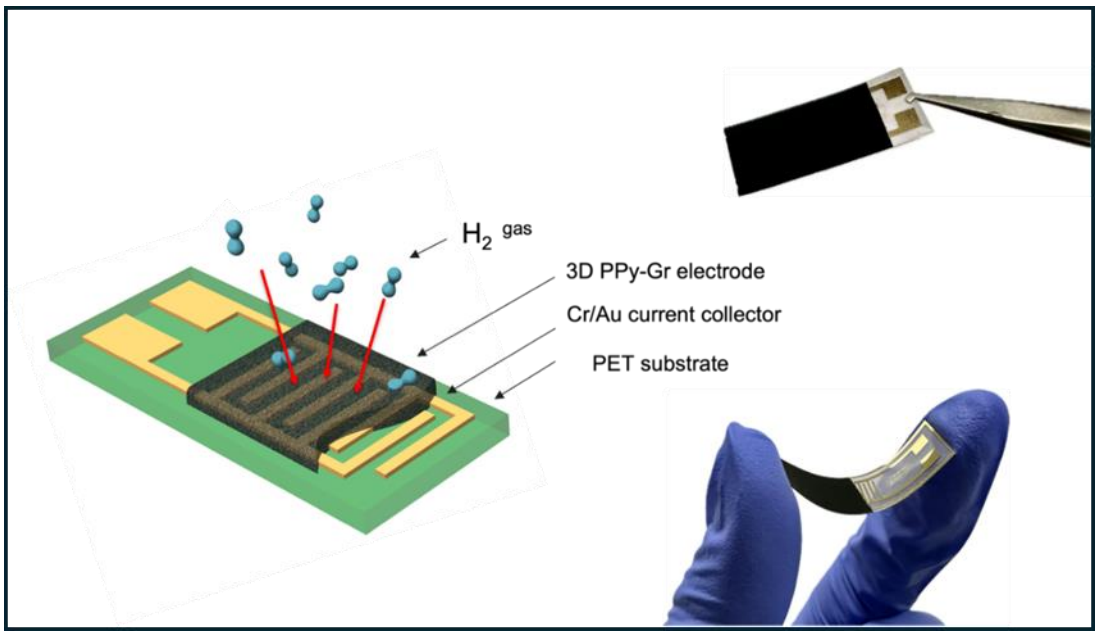

Figure 6.31. The graphical illustration of 3D PPy-Gr CGS.

The study compares the gas sensing performance of 3D Pure Polypyrrole (PPy) and 3D PPy-Graphene (PPy-Gr) composites for hydrogen gas detection at 1 to 100 ppm concentrations. Both sensors show increased resistance upon exposure to H_2 gas, indicating a positive correlation between gas concentration and sensor response. (Figure 6.32 A and B) The 3D Pure PPy sensor shows a smooth and gradual increase in resistance with each step of gas concentration but a slower recovery to baseline resistance. In contrast, the 3D PPy-Gr composite sensor shows a more pronounced and sharper response to each step of gas concentration, with faster recovery times compared to the 3D Pure PPy sensor. Because graphene has a large surface area and improves gas-sensing material interaction and charge transfer, the PPy-Gr composite is more sensitive than its counterpart. It appears that both sensors are very selective for hydrogen gas, as their resistance rises steadily as H_2 concentrations rise. As the resistance approaches its baseline value upon gas shutoff, the PPy-Gr sensor demonstrates superior stability and repeatability. It is essential to monitor air quality and industrial emissions, and the PPy-Gr sensor is well-suited for this task due to its high sensitivity and quick response/recovery times, which allow it to detect low amounts of hydrogen gas in the environment. The flexible nature of the PPy-Gr sensor also suggests potential applications in wearable devices for personal health and environmental monitoring.

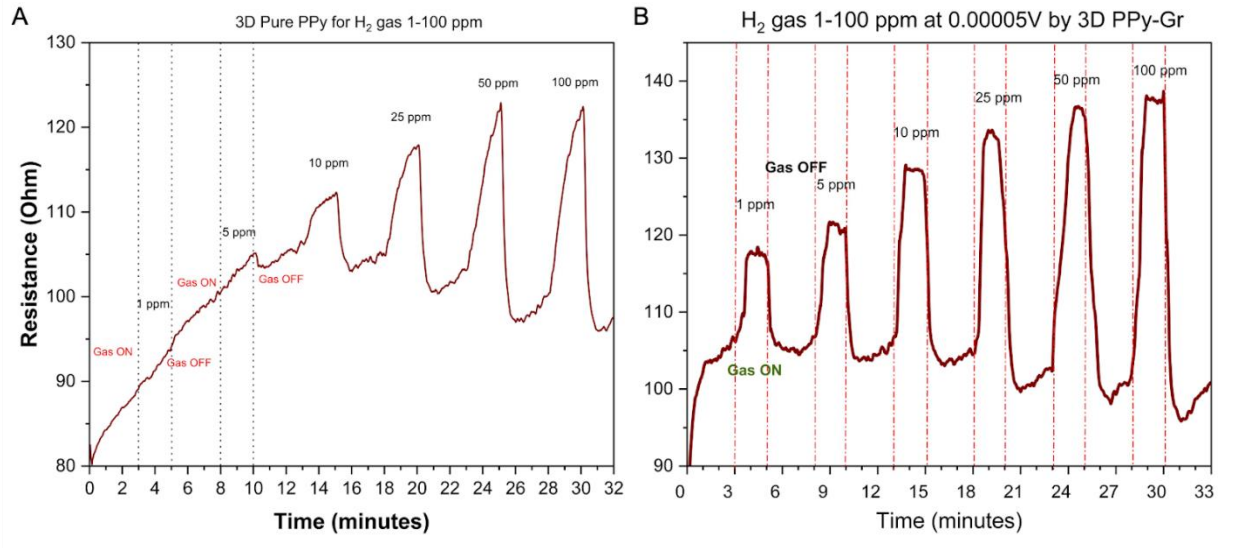

Figure 6.32. Gas sensing performance of 3D Pure Polypyrrole (PPy) and 3D PPy-Graphene (PPy-Gr) composites for hydrogen gas detection at concentrations ranging from 1 to 100 ppm.

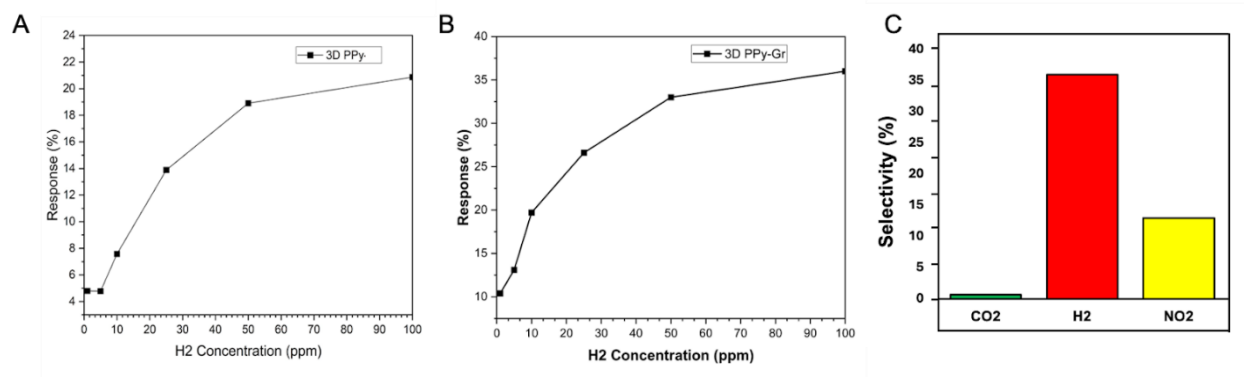

Figure 6.33. Sensitivity response of A) pure PPy and B) PPy-Gr sensors. C) Gas selectivity of 3D PPy-Gr sensor.

Figure 6.34 displays graphs illustrating the gas sensing response and selectivity of 3D PPy-Graphene (PPy-Gr) composites and 3D Pure Polypyrrole (PPy). The sensitivity of the 3D Pure PPy sensor to H_2 gas is demonstrated by its linear response to rising H_2 concentration. At larger doses, however, the reaction levels off, which might indicate a saturation effect. The addition of graphene to the 3D PPy-Gr composite sensor increases its overall responsiveness, which in turn increases its sensitivity to rising H_2 concentrations. The PPy-Gr sensor responds much more strongly to H_2 than to CO_2 or NO_2, demonstrating its excellent selectivity for H_2. Excellent selectivity against carbon dioxide is indicated by the minor reactivity to this gas. Although it is lower than the reaction to H_2, the response to NO_2 is greater than that to CO_2. The PPy-Gr

composite is an improved and dependable hydrogen detector due to its increased sensitivity to H_2 gas and its ability to retain strong selectivity. Compared to more conventional sensing materials, the sensor's performance is dramatically improved because to the addition of graphene to the polypyrrole matrix.

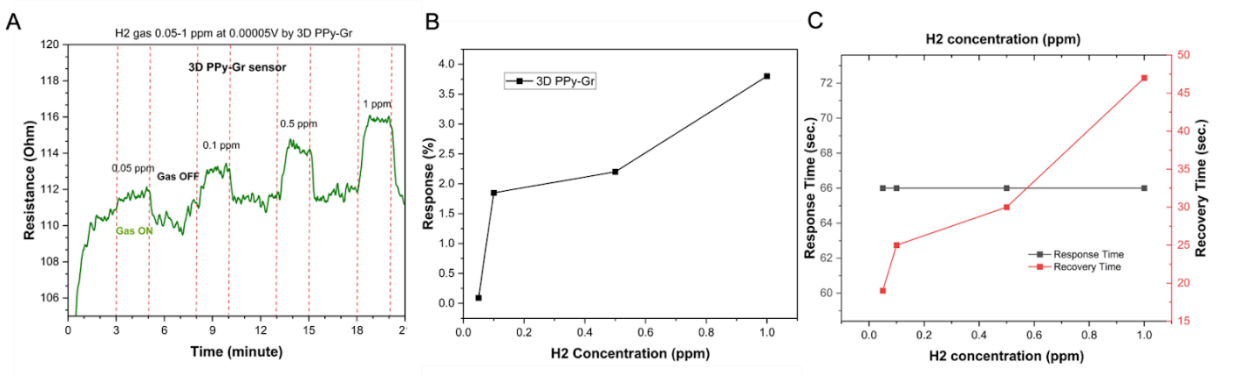

Figure 6.34. A) Hydrogen gas (H_2) sensing performance of the 3D PPy-Gr sensor at low concentrations between 0.05 ppm and 1 ppm. B) Sensitivity response of 3D PPy-Gr sensor for H_2 gas concentrations. C) Graphical representation of Response (t_{Res}) and Recovery times (t_{Rec}) for 3D PPy-Gr sensor at low hydrogen gas concentrations.

The 3D PPy-Gr sensor can detect hydrogen gas at low concentrations, especially between 0.05 and 1 ppm, and it is a sensitive and responsive gas-sensing device. Figure 6.34A demonstrates the sensor's excellent sensitivity and quick resistance rise upon exposure to even insufficient amounts of hydrogen, demonstrating its capacity to detect low levels of the gas effectively. The proportion of correct responses rises as H_2 concentration rises. This linearity is very important for sensor applications since it makes concentration measurements more accurate and facilitates calibration. It is clear that the sensor can react quickly to the presence of hydrogen because the reaction time is very constant over the concentration range, staying around 70 seconds. On the other hand, as the H_2 concentration rises, the recovery time also rises, indicating that the sensor needs more time to desorb gas molecules from the detecting surface.

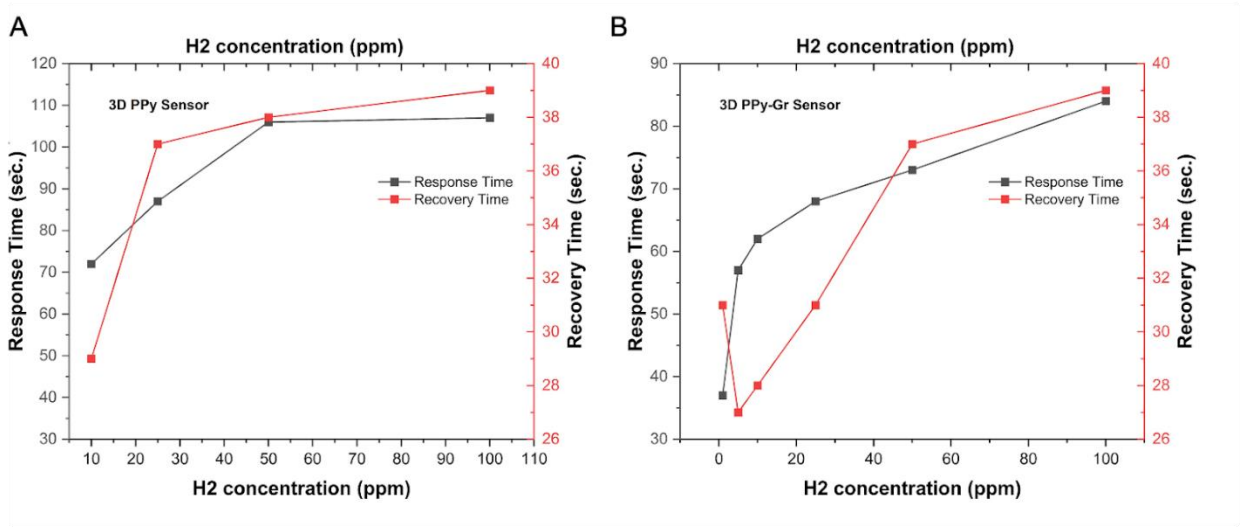

Figure 6.35. Graphical analysis of the Response (t_{Res}) and Recovery times (t_{Rec}) of 3D Pure Polypyrrole (PPy) and 3D PPy-Graphene (PPy-Gr) sensors when exposed to different concentrations (from 0 ppm to 100 ppm) of H_2 gas.

The 3D Pure PPy sensor's reaction time rises with concentration, indicating a slower rate of detection at higher concentrations. (Figure 6.35A) With a reaction time of 40 seconds at low concentrations and 80 seconds at 100 ppm, the PPy-Gr sensor has quicker recovery time. (Figure 6.35B) This is because of the graphene component's increased conductivity and surface area, which speed up the adsorption and charge transfer processes. With a recovery period of 26 seconds at lower concentrations and 38 seconds at 100 ppm, the PPy-Gr sensor's recovery time also increases. In terms of response and recovery times, the PPy-Gr sensor performs better than the Pure PPy sensor, making it a more dependable choice for hydrogen gas detection in a range of applications, such as industrial safety and environmental monitoring.

CONCLUSION

The 3D PPy-Gr hydrogen gas sensor outperforms the 3D Pure PPy sensor, making it a potential option for hydrogen detection applications. It exhibits the lowest detected concentration of hydrogen gas (0.05 ppm at room temperature) that has been documented to date. With a greater percentage response at every concentration level, the sensor exhibits increased sensitivity over a broad concentration range. Additionally, it has increased selectivity, being able to differentiate hydrogen gas from other ambient gases such as NO_2 and CO_2. Real-time monitoring and quick

detection cycles are made possible by the sensor's quicker reaction and recovery durations compared to the Pure PPy sensor. The dependability of the sensor is crucial for its useful use in diverse environments. Graphene is included into the PPy-Gr composite material, which improves charge transport characteristics and surface area to increase performance. For hydrogen detection applications in industrial safety, environmental monitoring, and portable sensing devices, this makes it a great option.

CHAPTER 7. CONCLUSIONS AND FUTURE WORK

7.1 CONCLUSIONS

The presented work successfully addressed all tasks formulated at the outset of PhD studies. We fabricated both two-dimensional and three-dimensional conducting polymers and their composites and investigated a broad range of applications. The proposed approach demonstrated remarkable versatility, enabling the straightforward fabrication of various conducting polymer morphologies and hybrid composites with multifunctional properties. The synthesized materials exhibited outstanding performance across all evaluated applications and covered knowledge gaps at each application area.

Our unique synthesis approach has proven to be a universal platform for generating different morphologies, facilitating the large-scale production of freestanding conducting polymers. The proposed approach allowed to fabricate highly conducting 2D polypyrrole nanosheets with conductivity of 219 S/cm. The 3D polypyrrole soft gels exhibited 0.3 S/cm conductivity which is also a great number compared to other 3D CPs. To the best of our knowledge there is not any work with comprehensive analysis of four surfactant interface effects on the polymer fabrication via bicontinuous microemulsion polymerization method. This method holds significant potential for advancing the field of conducting polymer research and its practical applications.

7.2 Future work

Further research articles focusing on 3D PPy composite materials are planned for publication. To ensure the robustness of micro-supercapacitors (MSCs), additional experiments will be conducted to evaluate the capacitance stability at various bending angles. Material modifications will be explored to enhance the capacitance of these devices.

For hydrogen gas sensors, additional selectivity tests will be performed to examine cross-sensitivity to other reducing gases. The sensors' sensitivity to humidity and performance across a range of temperatures, both lower and higher, will be evaluated. A multi-gas sensing platform will be developed based on conducting polymer composites to address a broader array of applications.

Moreover, a more detailed analysis of other interfacial bicontinuous systems will be undertaken to investigate their potential applications. This research will aim to further elucidate the properties and functionalities of these advanced materials.

References

1. Kaur, G., Adhikari, R., Cass, P., Bown, M. & Gunatillake, P. Electrically conductive polymers and composites for biomedical applications. *RSC Advances* vol. 5 37553–37567 Preprint at https://doi.org/10.1039/c5ra01851j (2015).
2. Kunitake, M., Kuraya, E., Kato, D., Niwa, O. & Nishimi, T. Electrochemistry in bicontinuous microemulsions based on control of dynamic solution structures on electrode surfaces. *Current Opinion in Colloid and Interface Science* vol. 25 13–26 Preprint at https://doi.org/10.1016/j.cocis.2016.05.004 (2016).
3. Yang, Q., Hou, Z. & Huang, T. Self-assembled polypyrrole film by interfacial polymerization for supercapacitor applications. *J Appl Polym Sci* **132**, (2015).
4. Qi, G., Huang, L. & Wang, H. Highly conductive free standing polypyrrole films prepared by freezing interfacial polymerization. *Chemical Communications* **48**, 8246–8248 (2012).
5. Sun, Y. *et al.* Synthesis of polypyrrole coated melamine foam by in-situ interfacial polymerization method for highly compressible and flexible supercapacitor. *J Colloid Interface Sci* **557**, 617–627 (2019).
6. Shi, H. *et al.* Conducting polymer hydrogels as a sustainable platform for advanced energy, biomedical and environmental applications. *Science of the Total Environment* vol. 786 Preprint at https://doi.org/10.1016/j.scitotenv.2021.147430 (2021).
7. Wang, B. *et al.* Properties of TX-100/n-butanol/cyclohexane/water microemulsion and its osmosis for wood. in *Journal of Biobased Materials and Bioenergy* vol. 5 197–202 (2011).
8. Abutalip, M. *et al.* Strategic Synthesis of 2D and 3D Conducting Polymers and Derived Nanocomposites. *Advanced Materials* **35**, (2023).
9. Shirakawa, H., Louis, E. J., MacDiarmid, A. G., Chiang, C. K. & Heeger, A. J. Synthesis of electrically conducting organic polymers: Halogen derivatives of polyacetylene, (CH)x. *J Chem Soc Chem Commun* 578–580 (1977) doi:10.1039/C39770000578.
10. Chiang, C. K. *et al.* Electrical Conductivity in Doped Polyacetylene. *Phys Rev Lett* **39**, 1098–1101 (1977).
11. Handbook_of_Conducting_Polymers_Second_Edition_Rev.
12. Le, T. H., Kim, Y. & Yoon, H. Electrical and electrochemical properties of conducting polymers. *Polymers* vol. 9 Preprint at https://doi.org/10.3390/polym9040150 (2017).
13. heeger 1992 diodes.
14. Hsieh, B. R. A Review of: " 'Organic Electroluminescent Materials and Devices' , Edited by S. Miyata and H. S. Nalwa, Gordon and Breach Science Publishers, Amsterdam, 1997; ISBN 2-919875-10-8; x + 487 pages, 12 color plates; $180.00" . *Molecular Crystals and Liquid Crystals Science and Technology. Section A. Molecular Crystals and Liquid Crystals* **326**, 425–427 (1999).
15. *Handbook of Conducting Polymers Third Edition CONJUGATED POLYMERS*.
16. Namsheer, K. & Rout, C. S. Conducting polymers: a comprehensive review on recent advances in synthesis, properties and applications. *RSC Advances* vol. 11 5659–5697 Preprint at https://doi.org/10.1039/d0ra07800j (2021).
17. Li, X., Gittleson, F., Carmo, M., Sekol, R. C. & Taylor, A. D. Scalable fabrication of multifunctional freestanding carbon nanotube/polymer composite thin films for energy conversion. *ACS Nano* **6**, 1347–1356 (2012).

18. MacDiarmid, A. G. ‘Synthetic metals’: A novel role for organic polymers (Nobel lecture). *Angewandte Chemie - International Edition* vol. 40 2581–2590 Preprint at https://doi.org/10.1002/1521-3773(20010716)40:14<2581::AID-ANIE2581>3.0.CO;2-2 (2001).
19. Akagi, K. *et al. SYNTHESIS OF POLYACETYLENE FILMS WITH HIGH DENSITY AND HIGH MECHANICAL STRENGTH*. *Synthetic Metals* vol. 28 (1989).
20. Ciric-Marjanovic, G. Recent advances in polyaniline research: Polymerization mechanisms, structural aspects, properties and applications. *Synthetic Metals* vol. 177 1–47 Preprint at https://doi.org/10.1016/j.synthmet.2013.06.004 (2013).
21. Wang, L.-X., Li, X.-G. & Yang, Y.-L. *Preparation, Properties and Applications of Polypyrroles*. *Reactive & Functional Polymers* vol. 47 www.elsevier.com/locate/react (2001).
22. Liu, R. & Liu, Z. Polythiophene: Synthesis in aqueous medium and controllable morphology. *Chinese Science Bulletin* **54**, 2028–2032 (2009).
23. Kirchmeyer, S. & Reuter, K. Scientific importance, properties and growing applications of poly(3,4-ethylenedioxythiophene). *J Mater Chem* **15**, 2077–2088 (2005).
24. Wen, J., Tian, Y., Mei, Z., Wu, W. & Tian, Y. Synthesis of polypyrrole nanoparticles and their applications in electrically conductive adhesives for improving conductivity. *RSC Adv* **7**, 53219–53225 (2017).
25. Li, Y., Bober, P., Trchová, M. & Stejskal, J. Polypyrrole prepared in the presence of methyl orange and ethyl orange: Nanotubes versus globules in conductivity enhancement. *J Mater Chem C Mater* **5**, 4236–4245 (2017).
26. Minisy, I. M. *et al.* Cationic dyes as morphology-guiding agents for one-dimensional polypyrrole with improved conductivity. *Polymer (Guildf)* **174**, 11–17 (2019).
27. Lakard, B. *et al.* Effect of ultrasounds on the electrochemical synthesis of polypyrrole, application to the adhesion and growth of biological cells. *Bioelectrochemistry* **75**, 148–157 (2009).
28. Fan, Y. *et al.* Conductively monolithic polypyrrole 3-D porous architecture with micron-sized channels as superior salt-resistant solar steam generators. *Solar Energy Materials and Solar Cells* **206**, (2020).
29. Gupta, A. *et al.* Nanostructured Polyaniline/Graphene/Fe2O3Composites Hydrogel as a High-Performance Flexible Supercapacitor Electrode Material. *ACS Appl Energy Mater* **3**, 6434–6446 (2020).
30. Liu, X., Zheng, W., Kumar, R., Kumar, M. & Zhang, J. Conducting polymer-based nanostructures for gas sensors. *Coordination Chemistry Reviews* vol. 462 Preprint at https://doi.org/10.1016/j.ccr.2022.214517 (2022).
31. Guimard, N. K., Gomez, N. & Schmidt, C. E. Conducting polymers in biomedical engineering. *Progress in Polymer Science (Oxford)* vol. 32 876–921 Preprint at https://doi.org/10.1016/j.progpolymsci.2007.05.012 (2007).
32. Murad, A. R., Iraqi, A., Aziz, S. B., Abdullah, S. N. & Brza, M. A. Conducting polymers for optoelectronic devices and organic solar cells: A review. *Polymers* vol. 12 1–47 Preprint at https://doi.org/10.3390/polym12112627 (2020).
33. Wang, Y. & Jing, X. Intrinsically conducting polymers for electromagnetic interference shielding. *Polymers for Advanced Technologies* vol. 16 344–351 Preprint at https://doi.org/10.1002/pat.589 (2005).

34. Iqbal, S. & Ahmad, S. Recent development in hybrid conducting polymers: Synthesis, applications and future prospects. *Journal of Industrial and Engineering Chemistry* vol. 60 53–84 Preprint at https://doi.org/10.1016/j.jiec.2017.09.038 (2018).
35. Sharma, S., Sudhakara, P., Omran, A. A. B., Singh, J. & Ilyas, R. A. Recent trends and developments in conducting polymer nanocomposites for multifunctional applications. *Polymers* vol. 13 Preprint at https://doi.org/10.3390/polym13172898 (2021).
36. Aydemir, N., Malmström, J. & Travas-Sejdic, J. Conducting polymer based electrochemical biosensors. *Physical Chemistry Chemical Physics* vol. 18 8264–8277 Preprint at https://doi.org/10.1039/c5cp06830d (2016).
37. Naveen, M. H., Gurudatt, N. G. & Shim, Y. B. Applications of conducting polymer composites to electrochemical sensors: A review. *Applied Materials Today* vol. 9 419–433 Preprint at https://doi.org/10.1016/j.apmt.2017.09.001 (2017).
38. Park, S. J., Park, C. S. & Yoon, H. Chemo-electrical gas sensors based on conducting polymer hybrids. *Polymers* vol. 9 Preprint at https://doi.org/10.3390/polym9050155 (2017).
39. Zhou, Q. & Shi, G. Conducting Polymer-Based Catalysts. *Journal of the American Chemical Society* vol. 138 2868–2876 Preprint at https://doi.org/10.1021/jacs.5b12474 (2016).
40. Karg, S., Scott, J. C., Salem, J. R. & Angelopoulos, M. *Increased Brightness and Lifetime of Polymer Light-Emitting Diodes with Polyaniline Anodes*. *Synthetic Metals* vol. 80 (1996).
41. Nambiar, S. & Yeow, J. T. W. Conductive polymer-based sensors for biomedical applications. *Biosensors and Bioelectronics* vol. 26 1825–1832 Preprint at https://doi.org/10.1016/j.bios.2010.09.046 (2011).
42. Snook, G. A., Kao, P. & Best, A. S. Conducting-polymer-based supercapacitor devices and electrodes. *Journal of Power Sources* vol. 196 1–12 Preprint at https://doi.org/10.1016/j.jpowsour.2010.06.084 (2011).
43. Mandal, T. K., Fleming, M. S. & Walt, D. R. Preparation of Polymer Coated Gold Nanoparticles by Surface-Confined Living Radical Polymerization at Ambient Temperature. *Nano Lett* **2**, 3–7 (2002).
44. El-Sayed, M. A. Some interesting properties of metals confined in time and nanometer space of different shapes. *Acc Chem Res* **34**, 257–264 (2001).
45. Corbierre, M. K. *et al.* Polymer-stabilized gold nanoparticles and their incorporation into polymer matrices [13]. *Journal of the American Chemical Society* vol. 123 10411–10412 Preprint at https://doi.org/10.1021/ja0166287 (2001).
46. Heeger, A. J. Semiconducting and metallic polymers: The fourth generation of polymeric materials. *Journal of Physical Chemistry B* **105**, 8475–8491 (2001).
47. Le, T. H., Kim, Y. & Yoon, H. Electrical and electrochemical properties of conducting polymers. *Polymers* vol. 9 Preprint at https://doi.org/10.3390/polym9040150 (2017).
48. Kivelson ', S. & Heeger, A. J. *PHYSICAL REVIEW LETTERS First-Order Transition to a Metallic State in Polyacetylene: A Strong-Coupling Polaronic Metal*. vol. 55 (1985).
49. Heeger, A. J., Kivelson, S., Schrieffer, J. R. & Su, W.-P. *Solitons in Conducting Polymers*. (1988).
50. Su, W. P., Schrieffer, J. R. & Heeger, A. J. *Solitons in Polyaeetylene*. vol. 42.
51. Handbook_of_Conducting_Polymers_Second_Edition_Rev.

52. Wang, L.-X., Li, X.-G. & Yang, Y.-L. *Preparation, Properties and Applications of Polypyrroles*. *Reactive & Functional Polymers* vol. 47 www.elsevier.com/locate/react (2001).
53. Groenendaal, L., Jonas, F., Freitag, D., Pielartzik, H. & Reynolds, J. R. Poly(3,4-ethylenedioxythiophene) and Its Derivatives: Past, Present, and Future. *Advanced Materials* **12**, 481–494 (2000).
54. Xiong, S., Phua, S. L., Dunn, B. S., Ma, J. & Lu, X. Covalently bonded polyaniline-TiO2 hybrids: A facile approach to highly stable anodic electrochromic materials with low oxidation potentials. *Chemistry of Materials* **22**, 255–260 (2010).
55. Chen, B., Liu, C., Ge, L. & Hayashi, K. Electrical conduction and gas sensing characteristics of P3HT/Au nano-islands composite. *Sens Actuators B Chem* **241**, 1099–1105 (2017).
56. Ye, S. & Feng, J. Self-assembled three-dimensional hierarchical graphene/polypyrrole nanotube hybrid aerogel and its application for supercapacitors. *ACS Appl Mater Interfaces* **6**, 9671–9679 (2014).
57. Saini, P., Choudhary, V., Singh, B. P., Mathur, R. B. & Dhawan, S. K. Polyaniline-MWCNT nanocomposites for microwave absorption and EMI shielding. *Mater Chem Phys* **113**, 919–926 (2009).
58. Chougule, M. A. *et al.* Synthesis and Characterization of Polypyrrole (PPy) Thin Films. *Soft Nanoscience Letters* **01**, 6–10 (2011).
59. Pang, A. L., Arsad, A. & Ahmadipour, M. Synthesis and factor affecting on the conductivity of polypyrrole: a short review. *Polymers for Advanced Technologies* vol. 32 1428–1454 Preprint at https://doi.org/10.1002/pat.5201 (2021).
60. Le, T. H., Kim, Y. & Yoon, H. Electrical and electrochemical properties of conducting polymers. *Polymers* vol. 9 Preprint at https://doi.org/10.3390/polym9040150 (2017).
61. Tan, Y. & Ghandi, K. Kinetics and mechanism of pyrrole chemical polymerization. *Synth Met* **175**, 183–191 (2013).
62. Huang, J. & Kaner, R. B. Nanofiber Formation in the Chemical Polymerization of Aniline: A Mechanistic Study. *Angewandte Chemie* **116**, 5941–5945 (2004).
63. Olad, A. & Nosrati, R. Preparation and corrosion resistance of nanostructured PVC/ZnO-polyaniline hybrid coating. *Prog Org Coat* **76**, 113–118 (2013).
64. Xu, H., Zhang, J., Chen, Y., Lu, H. & Zhuang, J. Electrochemical polymerization of polyaniline doped with Cu2+ as the electrode material for electrochemical supercapacitors. *RSC Adv* **4**, 5547–5552 (2014).
65. Heinze, J., Frontana-Uribe, B. A. & Ludwigs, S. Electrochemistry of conducting polymers-persistent models and new concepts. *Chem Rev* **110**, 4724–4771 (2010).
66. Richardson-Burns, S. M., Hendricks, J. L. & Martin, D. C. Electrochemical polymerization of conducting polymers in living neural tissue. *J Neural Eng* **4**, (2007).
67. Friebe, C., Zens, C., Kupfer, S. & Schubert, U. S. Additive-Free Organic Radical Batteries Prepared through Electrochemical Polymerization of TEMPO-Decorated Terthiophene. *Journal of Physical Chemistry C* **127**, 1333–1344 (2023).
68. Cai, X., Anyaogu, K. C. & Neckers, D. C. Photopolymerization of conductive polymeric metal nanoparticles. *Photochemical and Photobiological Sciences* **8**, 1568–1573 (2009).
69. Heydarnezhad, H. R., Pourabbas, B. & Tayefi, M. Conducting electroactive polymers via photopolymerization: A review on synthesis and applications. *Polymer - Plastics*

Technology and Engineering vol. 57 1093–1109 Preprint at https://doi.org/10.1080/03602559.2017.1370111 (2018).
70. Fang, Q., Chetwynd, D. G. & Gardner, J. W. *Conducting Polymer Films by UV-Photo Processing*.
71. Nishio, S. *et al. Preparation of Polythiophene Thin Films by UV Laser-Assisted Deposition of 2,5-Dichlorothiophene with a 248 Nm Excimer Laser Beam*. *Journal of Photochemistry and Photobiology A: Chemistry* vol. 116 (1998).
72. Paosawatyanyong, B., Tapaneeyakorn, K. & Bhanthumnavin, W. AC plasma polymerization of pyrrole. *Surf Coat Technol* **204**, 3069–3072 (2010).
73. Cruz, G. J., Morales, J., Castillo-Ortega, M. M. & Olayo, R. *Synthesis of Polyaniline Films by Plasma Polymerization*. *Synthetic Metals* vol. 88 (1997).
74. Park, C. S. *et al.* Conductive polymer synthesis with single-crystallinity via a novel plasma polymerization technique for gas sensor applications. *Materials* **9**, (2016).
75. Kim, J. Y. *et al.* In-situ iodine doping characteristics of conductive polyaniline film polymerized by low-voltage-driven atmospheric pressure plasma. *Polymers (Basel)* **13**, 1–14 (2021).
76. Nuraje, N., Su, K., Yang, N. I. & Matsui, H. Liquid/liquid interfacial polymerization to grow single crystalline nanoneedles of various conducting polymers. *ACS Nano* **2**, 502–506 (2008).
77. Dallas, P. & Georgakilas, V. Interfacial polymerization of conductive polymers: Generation of polymeric nanostructures in a 2-D space. *Advances in Colloid and Interface Science* vol. 224 46–61 Preprint at https://doi.org/10.1016/j.cis.2015.07.008 (2015).
78. Qi, G., Wu, Z. & Wang, H. Highly conductive and semitransparent free-standing polypyrrole films prepared by chemical interfacial polymerization. *J Mater Chem C Mater* **1**, 7102–7110 (2013).
79. Kim, S. C. *et al.* Template-assisted synthesis of self-doped polyaniline: Morphological effects of templates on the conductivity. *Macromol Rapid Commun* **28**, 1356–1360 (2007).
80. Estrany, F., Calvet, A., Del Valle, L. J., Puiggalí, J. & Alemán, C. A multi-step template-assisted approach for the formation of conducting polymer nanotubes onto conducting polymer films. *Polym Chem* **7**, 3540–3550 (2016).
81. Samwang, T., Watanabe, N. M., Okamoto, Y., Srinives, S. & Umakoshi, H. Study of Chemical Polymerization of Polypyrrole with SDS Soft Template: Physical, Chemical, and Electrical Properties. *ACS Omega* **8**, 48946–48957 (2023).
82. Pan, L. *et al.* Hydrothermal synthesis of polyaniline mesostructures. *Adv Funct Mater* **16**, 1279–1288 (2006).
83. Vandana, M., Vijeth, H., Ashokkumar, S. P. & Devendrappa, H. Hydrothermal synthesis of quantum dots dispersed on conjugated polymer as an efficient electrodes for highly stable hybrid supercapacitors. *Inorg Chem Commun* **117**, (2020).
84. Li, S. *et al.* Modifying Reduced Graphene Oxide by Conducting Polymer Through a Hydrothermal Polymerization Method and its Application as Energy Storage Electrodes. *Nanoscale Res Lett* **14**, (2019).
85. Chu, J. *et al.* Synthesis and electrochromic properties of conducting polymers: Polyaniline directly grown on fluorine-doped tin oxide substrate via hydrothermal techniques. *Solar Energy Materials and Solar Cells* **177**, 70–74 (2018).

86. Palaniappan, S. & John, A. Polyaniline materials by emulsion polymerization pathway. *Progress in Polymer Science (Oxford)* vol. 33 732–758 Preprint at https://doi.org/10.1016/j.progpolymsci.2008.02.002 (2008).
87. Imran, S. M. *et al.* Enhancement of electroconductivity of polyaniline/graphene oxide nanocomposites through in situ emulsion polymerization. *J Mater Sci* **49**, 1328–1335 (2014).
88. Lei, Y., Oohata, H., Kuroda, S. I., Sasaki, S. & Yamamoto, T. Highly electrically conductive poly(3,4-ethylenedioxythiophene) prepared via high-concentration emulsion polymerization. *Synth Met* **149**, 211–217 (2005).
89. Salah Abdullah, H. Electrochemical polymerization and Raman study of polypyrrole and polyaniline thin films. *International Journal of Physical Sciences* **7**, 5468–5476 (2012).
90. Pavel, F. M. Microemulsion polymerization. *J Dispers Sci Technol* **25**, 1–16 (2004).
91. Malik, M. A., Wani, M. Y. & Hashim, M. A. Microemulsion method: A novel route to synthesize organic and inorganic nanomaterials. 1st Nano Update. *Arabian Journal of Chemistry* vol. 5 397–417 Preprint at https://doi.org/10.1016/j.arabjc.2010.09.027 (2012).
92. Sripriya, R., Muthu Raja, K., Santhosh, G., Chandrasekaran, M. & Noel, M. The effect of structure of oil phase, surfactant and co-surfactant on the physicochemical and electrochemical properties of bicontinuous microemulsion. *J Colloid Interface Sci* **314**, 712–717 (2007).
93. Gao, N., Yu, J., Chen, S., Xin, X. & Zang, L. Interfacial polymerization for controllable fabrication of nanostructured conducting polymers and their composites. *Synthetic Metals* vol. 273 Preprint at https://doi.org/10.1016/j.synthmet.2020.116693 (2021).
94. Hazarika, J. & Kumar, A. Controllable synthesis and characterization of polypyrrole nanoparticles in sodium dodecylsulphate (SDS) micellar solutions. *Synth Met* **175**, 155–162 (2013).
95. Khadem, F., Pishvaei, M., Salami-Kalajahi, M. & Najafi, F. Morphology control of conducting polypyrrole nanostructures via operational conditions in the emulsion polymerization. *J Appl Polym Sci* **134**, (2017).
96. Pal, N., Saxena, N. & Mandal, A. Phase Behavior, Solubilization, and Phase Transition of a Microemulsion System Stabilized by a Novel Surfactant Synthesized from Castor Oil. *J Chem Eng Data* **62**, 1278–1291 (2017).
97. Zhang, F., Fan, J. bing & Wang, S. Interfacial Polymerization: From Chemistry to Functional Materials. *Angewandte Chemie - International Edition* vol. 59 21840–21856 Preprint at https://doi.org/10.1002/anie.201916473 (2020).
98. Yan, F., Xue, G. I. & Zhou, M. *Preparation of Electrically Conducting Polypyrrole in Oil/Water Microemulsion*. *J Appl Polym Sci* vol. 77 (2000).
99. Mackay, R. A. *PROPERTIES OF HIGH EMULSIFIER CONTENT 0/W MICROEMULSIONS*.
100. Iwunze, M. 0, Hu, N. & Rusling, J. F. *Electrocatalysis in Organized Assemblies Part X. Debromination of Alkyl Vicinal Dibromides with Neutral Metal Phthalocyanines in a Bicontinuous Microemulsion. I. Electroanal. Chem* vol. 333 (1992).
101. Gounili, G., Bobbitt, J. M. & Rusling, J. F. *Electron Transfer between Amphiphilic Ferrocenes and Electrodes in a Bicontinuous Microemulsion*. *Langmuir* vol. 11 (1996).
102. Yoshitake, S. *et al. Electrochemistry in Middle Phase Microemulsion Composed of Saline and Toluene with Sodium Dodecylsulfate and N-Butanol*.

103. Kawano, S., Kobayashi, D., Taguchi, S., Kunitake, M. & Nishimi, T. Construction of continuous porous organogels, hydrogels, and bicontinuous organo/hydro hybrid gels from bicontinuous microemulsions. *Macromolecules* **43**, 473–479 (2010).
104. Yang, W., Furukawa, H. & Gong, J. P. Highly extensible double-network gels with self-assembling anisotropic structure. *Advanced Materials* **20**, 4499–4503 (2008).
105. Jeon, J. *et al. Wilkin-Son. J. Vac. Sci. Technol. A* vol. 406 (2000).
106. Sakata, K. *et al.* Continuous porous poly(N-isopropylacrylamide) gels prepared from a bicontinuous microemulsion. *Chem Lett* **43**, 240–242 (2014).
107. Sakata, K. *et al.* Continuous porous poly(N-isopropylacrylamide) gels prepared from a bicontinuous microemulsion. *Chem Lett* **43**, 240–242 (2014).
108. Wu, T. & Chen, B. Facile Fabrication of Porous Conductive Thermoplastic Polyurethane Nanocomposite Films via Solution Casting. *Sci Rep* **7**, (2017).
109. Ham, H., Sim, G., Choi, W. & Park, M. J. Porous pathways: Exploring the future of conducting polymers. *Bulletin of the Korean Chemical Society* vol. 45 200–213 Preprint at https://doi.org/10.1002/bkcs.12814 (2024).
110. Guo, X. *et al.* Application of conductive polymer hydrogels in flexible electronics. *Journal of Polymer Science* Preprint at https://doi.org/10.1002/pol.20210933 (2022).
111. Wang, X. S., Tang, H. P., Li, X. D. & Hua, X. Investigations on the mechanical properties of conducting polymer coating-substrate structures and their influencing factors. *International Journal of Molecular Sciences* vol. 10 5257–5284 Preprint at https://doi.org/10.3390/ijms10125257 (2009).
112. *Light-Emitting Diodes Using n-Type Conducting Polymer*.
113. Kim, J., Deshpande, S. D., Yun, S. & Li, Q. A comparative study of conductive polypyrrole and polyaniline coatings on electro-active papers. *Polym J* **38**, 659–668 (2006).
114. Kondawar, S. B. & Patil, P. T. Conducting Polymer Nanocomposites for Sensor Applications. in 223–267 (2017). doi:10.1007/978-3-319-46458-9_8.
115. Bai, H. & Shi, G. Gas Sensors Based on Conducting Polymers. *Sensors* **7**, 267–307 (2007).
116. Han, J., Johnson, I. & Chen, M. 3D Continuously Porous Graphene for Energy Applications. *Advanced Materials* vol. 34 Preprint at https://doi.org/10.1002/adma.202108750 (2022).
117. Sun, Z., Fang, S. & Hu, Y. H. 3D Graphene Materials: From Understanding to Design and Synthesis Control. *Chemical Reviews* vol. 120 10336–10453 Preprint at https://doi.org/10.1021/acs.chemrev.0c00083 (2020).
118. Song, F., Xu, J. & Hou, W. G. Surfactant-free oil/water and bicontinuous microemulsion composed of benzene, ethanol and water. *Chinese Chemical Letters* **21**, 880–883 (2010).
119. Sun, B. *et al.* A surfactant-free microemulsion consisting of water, ethanol, and dichloromethane and its template effect for silica synthesis. *J Colloid Interface Sci* **526**, 9–17 (2018).
120. Sripriya, R., Muthu Raja, K., Santhosh, G., Chandrasekaran, M. & Noel, M. The effect of structure of oil phase, surfactant and co-surfactant on the physicochemical and electrochemical properties of bicontinuous microemulsion. *J Colloid Interface Sci* **314**, 712–717 (2007).
121. Anwar, A., Numan, A., Siddiqui, R., Khalid, M. & Khan, N. A. Cobalt nanoparticles as novel nanotherapeutics against Acanthamoeba castellanii. *Parasit Vectors* **12**, (2019).

122. Foitzik, R. C., Kaynaka, A. & Pfefferb, F. M. *Synthesis and Polymerisation of a,u-Bis(3-Pyrrolyl)Alkanes*.
123. Zhu, S. *et al.* Highly photoluminescent carbon dots for multicolor patterning, sensors, and bioimaging. *Angewandte Chemie - International Edition* **52**, 3953–3957 (2013).
124. Salager, J. L., Marquez, R., Rondón, M., Bullón, J. & Graciaa, A. Review on Some Confusion Produced by the Bicontinuous Microemulsion Terminology and Its Domains Microcurvature: A Simple Spatiotemporal Model at Optimum Formulation of Surfactant-Oil-Water Systems. *ACS Omega* vol. 8 9040–9057 Preprint at https://doi.org/10.1021/acsomega.3c00547 (2023).
125. Wang, T. *et al.* Structural Tuning of a Flexible and Porous Polypyrrole Film by a Template-Assisted Method for Enhanced Capacitance for Supercapacitor Applications. *ACS Appl Mater Interfaces* **13**, 17726–17735 (2021).
126. Li, P. *et al.* Flexible, long cycle-life micro-supercapacitor with polypyrrole@Ag-wall interdigitated electrodes fabricated by micro-3D printing and electrochemical polymerization. *J Manuf Process* **94**, 338–347 (2023).
127. Grzeszczuk, M., Kepas, A., Kvarnstrom, C. & Ivaska, A. Effects of small octahedral mono, di, and trivalent hexafluoroanions on electronic and molecular structures of polypyrrole monitored by in situ UV-vis-NIR and resonance Raman spectroelectrochemical measurements. *Synth Met* **160**, 636–642 (2010).
128. Hasoon, S. & Salah Abdullah, H. Electrochemical polymerization and Raman study of polypyrrole and polyaniline thin films. *Article in International Journal of the Physical Sciences* **7**, 5468–5476 (2012).
129. Liu, Y. C. & Hwang, B. J. Identification of oxidized polypyrrole on Raman spectrum. *Synth Met* **113**, 203–207 (2000).
130. González, J. S. *et al.* Compact polyelectrolyte hydrogels of gelatin and chondroitin sulfate as ion's mobile media in sustainable all-solid state electrochemical devices. *Mater Adv* **1**, 2526–2535 (2020).
131. Costerton, J. W., Stewart, P. S. & Greenberg, E. P. Bacterial biofilms: A common cause of persistent infections. *Science* vol. 284 1318–1322 Preprint at https://doi.org/10.1126/science.284.5418.1318 (1999).
132. Norowski, P. A. & Bumgardner, J. D. Biomaterial and antibiotic strategies for peri-implantitis. *Journal of Biomedical Materials Research - Part B Applied Biomaterials* vol. 88 530–543 Preprint at https://doi.org/10.1002/jbm.b.31152 (2009).
133. Aiyer, K. & Doyle, L. E. Capturing the signal of weak electricigens: a worthy endeavour. *Trends in Biotechnology* vol. 40 564–575 Preprint at https://doi.org/10.1016/j.tibtech.2021.10.002 (2022).
134. Turick, C. E., Shimpalee, S., Satjaritanun, P., Weidner, J. & Greenway, S. Convenient non-invasive electrochemical techniques to monitor microbial processes: current state and perspectives. *Applied Microbiology and Biotechnology* vol. 103 8327–8338 Preprint at https://doi.org/10.1007/s00253-019-10091-y (2019).
135. Bosire, E. M. & Rosenbaum, M. A. Electrochemical potential influences phenazine production, electron transfer and consequently electric current generation by Pseudomonas aeruginosa. *Front Microbiol* **8**, (2017).
136. Liu, D. F. & Li, W. W. Potential-dependent extracellular electron transfer pathways of exoelectrogens. *Current Opinion in Chemical Biology* vol. 59 140–146 Preprint at https://doi.org/10.1016/j.cbpa.2020.06.005 (2020).

137. Olaifa, K., Ajunwa, O. & Marsili, E. Electroanalytic evaluation of antagonistic effect of azole fungicides on Acinetobacter baumannii biofilms. *Electrochim Acta* **405**, (2022).
138. Saito, J. *3.1 Introduction to Microbial Electrochemical Functions and Processes 3.1.1 Microbes Capable of Exchanging Electrons with Extracellular Solid Surfaces*. (2020).
139. Furst, A. L. & Francis, M. B. Impedance-Based Detection of Bacteria. *Chemical Reviews* vol. 119 700–726 Preprint at https://doi.org/10.1021/acs.chemrev.8b00381 (2019).
140. Suriyakumar, S., Bhardwaj, P., Grace, A. N. & Stephan, A. M. Role of Polymers in Enhancing the Performance of Electrochemical Supercapacitors: A Review. *Batteries and Supercaps* vol. 4 571–584 Preprint at https://doi.org/10.1002/batt.202000272 (2021).
141. Snook, G. A., Kao, P. & Best, A. S. Conducting-polymer-based supercapacitor devices and electrodes. *Journal of Power Sources* vol. 196 1–12 Preprint at https://doi.org/10.1016/j.jpowsour.2010.06.084 (2011).
142. Tao, J. *et al.* Solid-state high performance flexible supercapacitors based on polypyrrole-mno2-carbon fiber hybrid structure. *Sci Rep* **3**, (2013).
143. Zhao, Y. *et al.* Hierarchical polypyrrole@cobalt sulfide-based flexible on-chip microsupercapacitors with ultrahigh energy density for self-charging system. *Nano Res* **16**, 555–563 (2023).
144. Kunhikrishnan, L. & Shanmugham, R. High electrochemical performance of morphologically controlled cobalt oxide for supercapacitor application. *Mater Charact* **177**, (2021).
145. Wei, H. *et al.* Electropolymerized polypyrrole nanocomposites with cobalt oxide coated on carbon paper for electrochemical energy storage. *Polymer (Guildf)* **67**, 192–199 (2015).
146. Lee, C. P. *et al.* Cobalt oxide-decorated silicon carbide nano-tree array electrode for micro-supercapacitor application. *Materials* **14**, (2021).
147. Haider, W. A. *et al.* Bilayered microelectrodes based on electrochemically deposited MnO2/polypyrrole towards fast charge transport kinetics for micro-supercapacitors. *RSC Adv* **10**, 18245–18251 (2020).
148. Naderi, L. & Shahrokhian, S. Wire-type flexible micro-supercapacitor based on MOF-assisted sulfide nano-arrays on dendritic CuCoP and V2O5-polypyrrole/nanocellulose hydrogel. *Chemical Engineering Journal* **476**, (2023).
149. Wang, D., Wang, Q. & Wang, T. Morphology-controllable synthesis of cobalt oxalates and their conversion to mesoporous Co3O4 nanostructures for application in supercapacitors. *Inorg Chem* **50**, 6482–6492 (2011).
150. C.P, S. *et al.* Polyaniline-cobalt oxide nano shrubs based electrodes for supercapacitors with enhanced electrochemical performance. *Electrochim Acta* **324**, (2019).
151. Zhou, C., Zhang, Y., Li, Y. & Liu, J. Construction of high-capacitance 3D CoO@Polypyrrole nanowire array electrode for aqueous asymmetric supercapacitor. *Nano Lett* **13**, 2078–2085 (2013).
152. Chu, X. *et al.* Air-Stable Conductive Polymer Ink for Printed Wearable Micro-Supercapacitors. *Small* **17**, (2021).
153. Beidaghi, M. & Wang, C. Micro-supercapacitors based on three dimensional interdigital polypyrrole/C-MEMS electrodes. *Electrochim Acta* **56**, 9508–9514 (2011).
154. Qin, J. *et al.* Hierarchical Ordered Dual-Mesoporous Polypyrrole/Graphene Nanosheets as Bi-Functional Active Materials for High-Performance Planar Integrated System of Micro-Supercapacitor and Gas Sensor. *Adv Funct Mater* **30**, (2020).

155. Li, P. *et al.* Flexible, long cycle-life micro-supercapacitor with polypyrrole@Ag-wall interdigitated electrodes fabricated by micro-3D printing and electrochemical polymerization. *J Manuf Process* **94**, 338–347 (2023).
156. Tahir, M. *et al.* Pushing the Electrochemical Performance Limits of Polypyrrole Toward Stable Microelectronic Devices. *Nanomicro Lett* **15**, (2023).
157. Lu, J. *et al.* Polypyrrole and cotton fabric-based flexible micro-supercapacitors. *J Appl Polym Sci* **139**, (2022).
158. Kamboj, N. & Dey, R. S. Exploring the chemistry of "Organic/water-in-salt" electrolyte in graphene-polypyrrole based high-voltage (2.4V) microsupercapacitor. *Electrochim Acta* **421**, (2022).
159. Tian, W. *et al.* Implantable and biodegradable micro-supercapacitor based on a superassembled three-dimensional network Zn@ppy hybrid electrode. *ACS Appl Mater Interfaces* **13**, 8285–8293 (2021).
160. Ma, S. *et al.* Flexible Planar Microsupercapacitors Based on Polypyrrole Nanotubes. *ACS Appl Energy Mater* **4**, 8857–8865 (2021).
161. Qin, J. *et al.* Hierarchical Ordered Dual-Mesoporous Polypyrrole/Graphene Nanosheets as Bi-Functional Active Materials for High-Performance Planar Integrated System of Micro-Supercapacitor and Gas Sensor. *Adv Funct Mater* **30**, (2020).
162. Liu, L. *et al.* All-Printed Solid-State Microsupercapacitors Derived from Self-Template Synthesis of Ag@PPy Nanocomposites. *Adv Mater Technol* **3**, (2018).
163. Aradilla, D. *et al.* An innovative 3-D nanoforest heterostructure made of polypyrrole coated silicon nanotrees for new high performance hybrid micro-supercapacitors. *J Mater Chem A Mater* **3**, 13978–13985 (2015).
164. Hübert, T., Boon-Brett, L., Palmisano, V. & Bader, M. A. Developments in gas sensor technology for hydrogen safety. in *International Journal of Hydrogen Energy* vol. 39 20474–20483 (Elsevier Ltd, 2014).
165. Al-Mashat, L., Tran, H. D., Wlodarski, W., Kaner, R. B. & Kalantar-Zadeh, K. Conductometric hydrogen gas sensor based on polypyrrole nanofibers. *IEEE Sens J* **8**, 365–369 (2008).
166. Gu, H., Wang, Z. & Hu, Y. Hydrogen gas sensors based on semiconductor oxide nanostructures. *Sensors (Switzerland)* vol. 12 5517–5550 Preprint at https://doi.org/10.3390/s120505517 (2012).
167. Lawaniya, S. D. *et al.* Functional nanomaterials in flexible gas sensors: recent progress and future prospects. *Materials Today Chemistry* vol. 29 Preprint at https://doi.org/10.1016/j.mtchem.2023.101428 (2023).
168. Verma, A., Gupta, R., Verma, A. S. & Kumar, T. A review of composite conducting polymer-based sensors for detection of industrial waste gases. *Sensors and Actuators Reports* vol. 5 Preprint at https://doi.org/10.1016/j.snr.2023.100143 (2023).
169. Resistive-type hydrogen gas sensor based on TiO2- A review.
170. Bai, H. & Shi, G. Gas Sensors Based on Conducting Polymers. *Sensors* **7**, 267–307 (2007).
171. Das, M. & Roy, S. Polypyrrole and associated hybrid nanocomposites as chemiresistive gas sensors: A comprehensive review. *Materials Science in Semiconductor Processing* vol. 121 Preprint at https://doi.org/10.1016/j.mssp.2020.105332 (2021).

172. Al-Mashat, L., Tran, H. D., Wlodarski, W., Kaner, R. B. & Kalantar-Zadeh, K. Conductometric hydrogen gas sensor based on polypyrrole nanofibers. *IEEE Sens J* **8**, 365–369 (2008).
173. Anand, K., Singh, O., Singh, M. P., Kaur, J. & Singh, R. C. Hydrogen sensor based on graphene/ZnO nanocomposite. *Sens Actuators B Chem* **195**, 409–415 (2014).